CRANFIELD UNIVERSITY

Qiang Fu

Optimization of a Composite Wing Subject to Multi Constraints

School of Engineering
PhD in Aerospace Engineering

PhD Thesis
Academic Year: 2009 - 2013

Supervisor: Dr Shijun Guo
May 2013

CRANFIELD UNIVERSITY

School of Engineering
PhD Thesis

Submit for the Degree of Ph.D.

Academic Year 2009 - 2013

Qiang Fu

Optimization of a Composite Wing Subject to Multi Constraints

Supervisor: Dr Shijun Guo
May 2013

This thesis is submitted in partial fulfilment of the requirements for the degree of Ph.D.

ABSTRACT

In this thesis, an investigation has been carried out into a minimum weight optimization analysis of a composite wing with multi design constraints under both static and dynamic loadings. The study includes the influence of a morphing leading edge on the wing stiffness and gust load reduction by employing a passive gust alleviation device at the wing tip.

The design process started from a generic study of optimal structure against buckling for three typical types of reinforced skin panel structures including stiffener panel, sandwich and grid panel. The optimal design in terms of buckling performance and structural efficiency were compared. The study then focused on the optimal design of stiffened skin panels for a particular wing. Parametric studies on optimal design for isotropic stiffened panels were carried out in which practical design constraints were introduced. The optimal design method was further extended to composite stiffened skin panels. Optimal designs were obtained within a compression distributed load range from 500 N/mm to 5250 N/mm and a symmetric balanced layup with 0˚, 90˚, and ±45˚ plies. Based on the study, the modelling and optimal design method for composite stiffened panels was applied to a composite wing box for its upper surface panel design. The initial composite wing box was designed to achieve a minimum weight. Gradient based optimization method was applied in the analysis with practical design constraints. The results indicate that the effect of leading edge morphing on the overall wing structural stiffness is negligible. It has been shown that the weight of the upper surface of the wing box structure can be reduced by 19.8% from its initial design.

Optimal design of a passive gust alleviation device (PGAD) mounted at the wing tip was then investigated. Based on the dynamic analysis of the 3D wing FE model in different flight and payload cases, a method and program was

developed to create a dynamically equivalent beam model. Gust response of the optimized wing model was computed for a wide range of frequencies in accordance with the CS-25. Next, a parametric study of the key design variables of the PGAD was carried out to determine the optimal design parameters for minimum gust loading. The results have shown that the gust response can be reduced by 15% by using a 1m long PGAD for a conventional aircraft wing and yet reduce 50% tip displacement with 37.2% bending moment at wing root for a flying wing concept aircraft wing with 1.6m long PGAD mounted at the wing tip.

The results of the investigation contribute to knowledge in the following aspects. It provides an evaluation of the structural efficiency of three typical types of stiffened panels against buckling prevention. The research also provided an optimal design method for composite stringer stiffened panels by combining theoretical and practical design constraints. It made possible for the first-time a numerical evaluation of the novel PGAD as applied to a large aircraft.

ACKNOWLEDGEMENTS

Firstly I would like to thank my parents, especially my father. There was a time in my time I was really disappointed by myself but his love and confidence in me finally bring me out of the dark. In the past couple of years, I almost gave up my study several times, but I persisted just because I do not want to disappoint him. He never blamed me for anything because I am the continuation of his life.

I would like to really appreciate my supervisor Dr Shijun Guo for his guidance, kindness, and patience during the last three years. During the time, his attitude and passion towards academic and life really impressed me generously sharing his life experiences and knowledge. During my study, he really spent a lot of time and efforts on me I really appreciate that and will always remember these days that I spent with him in Cranfield University.

It is also a pleasure to acknowledge Natalia di Matteo, Ryoko Morishima, Shakeel Ahmed, and Marco Boscolo for their friendship and help during my study. With them, I feel I am not along on this journey and lucky to know these smart, hummer, and nice friends.

I also really thank those friends I made in Cranfield University. I did spend a good time with them and they would always be a part of my life.

TABLE OF CONTENTS

LIST OF FIGURES

LIST OF TABLES

LIST OF EQUATIONS

List of Nomenclature and Symbols

N_x	Resultant In-plane Force Intensity in x-axis
N_y	Resultant In-plane Force Intensity in y-axis
N_{xy}	Shear Force Intensity in the x(y)-axis
M_x	Resultant Moment Intensity about x-axis
M_y	Resultant Moment Intensity about y-axis
M_{xy}	Twist Moment Intensity about x(y)-axis
ε_x	Direct Strain in x-axis
ε_y	Direct Strain in y-axis
γ_{xy}	Direct Shear Strain in the xy-axis
k_x	The Bending Curvature of XY plane about Y axis
k_y	The Bending Curvature of XY plane about X axis
k_{xy}	The Twist Curvature of XY plane about X(Y) axis
A_{xy}	x,y=1-3, Extensional Stiffness Matrix
B_{xy}	x,y=1-3, Membrane-Bending Coupling Stiffness Matrix
D_{xy}	x,y=1-3, Bending Stiffness Matrix
f_1	Stress in Fibre Direction
f_2	Stress in Off-Fibre Direction
f_{12}	In Plane Shear Stress
X_t	Tensile Strength in Fibre Direction
Y_t	Tensile Strength in Off-Fibre Direction
X_c	Compressive Strength in Fibre Direction
Y_c	Compressive Strength in Off-Fibre Direction
S	In Plane Shear Strength
ε_1	Strain in Fibre Direction
ε_2	Strain in Off-Fibre Direction
ε_{12}	In Plane Shear Strain
ε_{xt}, ε_{yt}	Tensile Failure Strains
ε_{xc}, ε_{yc}	Compressive Failure Strains
ε_s	Shear Failure Strain

Q_{xy}	x,y=1-3, Reduced Stiffness Matrix
U	Internal Strain Energy
V	External Load Energy
a	Plate dimension in x-diretion
b	Plate dimension in y-diretion
D	Flexural rigidity of a plate
w	Displacement in z-axis
$N_{x,cr}$	Critical Distributed Load in x-axis
E	Young's Modulus
G	Shear Modulus
μ	Poisson Ratio
t_s	Skin thickness
σ_{cr}	Critical Buckling Stress
k	Buckling Coefficient
b_f	Flange Length
t_f	Flange Thickness
b_w	Web Length
t_w	Web Thickness
b_a	Attachment Flange Length
t_a	Attachment Flange Thickness
b_s	Stringer Pitch
ϵ	Emero's Buckling Efficiency
ϵ_{max}	Optimum Emero's Buckling Efficiency
r_{bw}	b_w/b_s
r_{tw}	t_w/t_s
r_{bf}	b_f/b_s
r_{tf}	t_f/t_s
L	Stiffened Panel Length
$\bar{t}$	Effective Thickness
ρ_G	radius of gyration
α , β , γ	Dimensionless Geometric Expressions

A_{st}	Section Area of Stringer
A_{sk}	Section Area of Skin
K_b	Bending Stiffness
K_t	Torsional Stiffness
M	Moment
T	Torque
I	Length of a Cantilever Uniform Beam
J	Second Moment of Area
h_s	Structure Stiffness
h_a	Aerodynamic Stiffness
H	An Aerodynamic Hinge Moment
δ	An Aileron (or Elevator) Rotated Angle
ρ	Air Density
S_a	Aileron Reference Span
C_a	Aileron Reference Chord
b_2	A Constant Depending on the Shape and Type of Balance
V	Flight Velocity
V_{DIV}	Divergence velocity
P_k	Forces at Aerodynamic Grid Points
U_k	Displacements at Aerodynamic Grid Points
$\bar{q}$	Dynamic Pressure
S_{kj}	Forces due to Pressures at the Aerodynamic Control Points
A_{jj}	Aerodynamic Influence Coefficient Matrix
D_{jk}	Substantial Derivative Matrix
w_j^g	Downwash at Initial condition
G_{kg}	Interpolation Matrix
Q_{aa}	Force due to Deformations
W_{kk}	A Matrix of Empirical Correction Factors
K_{aa}	Structural Stiffness Matrix
P_a	Vector of applied loads

Q_{ax}	Forces due to Unit Deflection
D	Damping Matrix
a	Acceleration
$H_n^{(m)}$	Bessel Functions
k	Reduced Frequency
m	Mach Number
t	time
T	Period
R_1	Maximum Landing Weight / Maximum Take-off Weight
R_2	Maximum Zero Fuel Weight / Maximum Take-off Weight
Z_{mo}	Maximum operating altitude
U_{ref}	Reference gust speed
t_{ply}	Ply Thickness
t_c	Core Height
BLF	Buckling Load Factor
EI	Bending Rigidity
GJ	Torsional Rigidity
V_D	Design Velocity

1 Introduction

1.1 Overview and Motivation

A minimum weight aircraft structure meeting all the design requirements is always an ultimate design target for structural engineers. Such a design provides benefits in payload, less fuel consumption, environment friendly low carbon foot-print in both emissions and manufacture waste. Over the past decades, research efforts were made to develop advanced design methods and technologies such as optimization methods, use of composite materials, morphing wing and gust alleviation devices. Although significant weight saving has been achieved by applying some of the techniques, it is by no means the end of design improvement and further developments of relevant techniques have continued.

With the introduction of the composite materials to aerospace industry, the advantages in obtaining high specific stiffness and strength led to a revolution in aircraft design and manufacture. Dramatic increase in using composite materials in civil aircraft have taken place in the last decade around the world. A350 XWB and B787 are made of more than 50% of composite materials which set a milestone for application of composite materials in aviation industry. The application of composite material in aircraft design drives the research efforts on developing optimal design methods for not only composite material itself but also for composite component design. Many research efforts have been expended on developing such methods and this would carry on along with the application of composite materials.

The application of optimization methods is another key technique to achieve a minimum weight aircraft design. Many optimization methods have been

developed and applied to aircraft components design for minimum weight. With a proper selection of optimization methods, a satisfactory design can be achieved with less time than manual iteration. The use of composite materials offers not only a potential weight saving, but also further options for structural engineers to achieve specific design targets and requirements by laminate tailoring or optimization. The optimization of composite aircraft structures usually involves a considerable large number of design variables and multi design constraints. This drives further development in optimization methods and algorithms.

In addition to the optimization of structures in the routine design procedure, various advanced technologies are applied to airframe. Those technologies will improve aircraft performance. They can produce benefit beyond structural optimization although weight penalty may have to be paid at this stage. One of the examples is morphing technology applied to wing and high lift devices. The current study is actually part of an EU FP7 programme ‘Smart High Lift Devices for Next Generation Aircraft (SADE)’. Another example is the use of active or passive control surfaces for flutter suppression and gust load reduction. In this thesis, an investigation has been made into the optimal design and analysis of a forward-elastic-axis and torsional-spring connected passive gust alleviation device mounted at wing tip. A proper design of such a device reduces wing tip displacement and bending moment at wing root during gust without a significant weight penalty.

1.2 Aims and Objectives

The aim of this research work is to develop a methodology and process for a minimum weight design optimization of a composite wing with smart leading edge and a passive gust alleviation device. The methodology and process are based on detailed structure FE modelling and analysis subject to multi design

constraints. The optimal design of composite wing structure started from the stiffened panel type selection and optimization. Following an initial wing structure design, an optimization method is applied to the composite wing to achieve minimum weight in the whole design process.

To achieve the aim, research objectives are set as follows:

- To determine the optimal structure type within stringer stiffened panel, sandwich panel, and grid structure for panel design against buckling under distributed compressive load
- To develop an optimal design method and program for composite stiffened panels under distributed compressive load subject to buckling
- To optimize a composite wing structure for minimum weight with the optimized upper skin panel subject to multi design constraints
- To design and optimize a passive gust alleviation device mounted at the wing tip and calculate the gust load reduction.

In order to achieve these objectives, analytical methods and numerical methods were introduced to each objective whenever necessary. Three types of structures are considered for the optimal structure type selection under a given uniaxial compression load and individual optimal design method for each structure type is used. The knowledge gained from this structure type selection was then applied to a composite wing box design case. Minimum weight design of the stiffened panels of the composite wing box became an important focus area. Optimization of the wing box assembled with optimal design stiffened panels with multi design constraints was then carried out to achieve a minimum weight with satisfying all design constraints. Then the optimization of the wing tip passive gust alleviation device was processed to ensure the entire wing achieved a minimum weight with an optimal designed wing tip gust alleviation device.

1.3 Research Novelty

The optimization started with the optimal structure type determination under uniaxial compression distributed load by comparing three panel stiffened methods (stringer panel, sandwich panel, and grid panel) against buckling. The investigations of optimal design of these structure types were carried out in previous research, but a comparison of these structure types have not been applied to guide structural engineers to determine the most efficient structure type under a given loading condition.

In this thesis a method for optimal design of composite stringer stiffened panels subject to practical design constraints is introduced. Attention is drawn to combine a minimum weight optimal solution against buckling with practical constraints to achieve a practical optimal design. This optimal design method is developed for both metallic and composite stiffened panels for maximum structural efficiency against buckling.

In the study of dynamic load and aeroelastic response, numerical evaluation of a passive gust alleviation device mounted at the wing tip is also investigated. This is achieved for the first time by using numerical solution tool to evaluate dynamic response of such a novel device on a large aircraft. In the initial study, a simplified beam model of the wing and the device are used and detailed numerical studies are carried out to investigate the performance of the device. An optimization method is introduced in the optimal design of the device by optimizing several key design parameters. The performance of such a device equipped to a commercial aircraft composite wing and a flying wing concept aircraft composite wing are examined.

1.4 Thesis Structure

The structure and layout of the thesis are described in this section to guide the reader smoothly on how the research work was systematically carried out.

Chapter 2 - Literature Review

This section summarized techniques related to the topics covered in this thesis. The review started from introduction of composite materials. The mechanics of composite materials and design processes of composite wings are summarized in this section. The state of the art on optimal design of stiffened panels, grid structures, and sandwich panels is given in the second section of this chapter. Morphing techniques are reviewed. Aeroelasticity section is divided into static aeroelasticity and dynamic aeroelasticity and different analysis methods are introduced and discussed. Different optimization techniques used in composite laminate design are highlighted and the advantage and disadvantage were discussed.

Chapter 3 - Optimal Structure Type Determination Subject to Buckling

In this section the buckling efficiency of three different types of structure, namely stringer stiffened panel, grid structure, and sandwich panel are compared within a practical load range. From topology optimization results, the loading path of uniform compression load case and combined loading case indicated that these structure types were efficient to carry specific loading condition. By comparing the efficiencies of optimal design of three structure types within a practical load range, a guideline for structural engineer to choose an optimal structure type against buckling was concluded. Theoretical and numerical methods were applied for evaluation.

Chapter 4 – Optimal Design of Composite Stringer Stiffened Panels

According to a practical loading range of a 200-seat commercial aircraft, the optimal structure type against buckling for the upper surface of the composite wing of the aircraft was stringer stiffened panel. To develop a method for optimal design of a composite stringer stiffened panel with practical constraints, Emero's optimal design method and Niu's practical design ratios are introduced firstly on metallic stringer stiffened panel and then extended to composite stringer stiffened panel. Theoretical and numerical methods are applied for verification.

Chapter 5 – Optimization of a Composite Wing with Multi Constraints

By assembling the upper surface panels of the composite wing designed in the optimal design method developed in Chapter 4 with other wing components, an initial design of the composite wing was obtained and strength check was processed. Static aeroelasticity analysis was carried out to update the spanwise lift loading distribution. A gradient based optimizer was introduced for minimum weight optimization and practical design parameters of a composite laminate were considered to limit design parameters.

Chapter 6 – Optimal Design of a Passive Gust Alleviation Wing Tip Device

A passive gust alleviation device was mounted to the composite wing optimized in Chapter 5. The composite wing was simplified into an equivalent beam model and the dynamic response of the beam model was studied. The device was then mounted to the wing by replacing a piece of segment from the wing tip. Parametric study on key design parameters of the device was then applied to show their impact to the performance of the device and optimization method was introduced to achieve an optimal design by varying several key design parameters.

Chapter 7 – Conclusions

In this chapter, the key results and findings in each chapter are summarized. The contribution of the investigations is concluded and some suggestions are provided for further research work.

2 Literature Review

This chapter presents optimal design techniques in each individual design phase to achieve a minimum weight design of a composite wing and morphing techniques are reviewed. It starts from an introduction of composite materials (Section 2.1), optimal design for metallic and composite structures subject to buckling (Section 2.2) including buckling of different structure types. Morphing techniques are reviewed and discussed in section 2.3. Section 2.4 presents aeroelasticity including static aeroelasticity and dynamic aeroelasticity. Static aeroelasticity, flutter and gust are reviewed in this section. Optimization is the last section (Section 2.5) in this chapter with optimization algorithm review and discussion. These sections give a whole picture about the techniques applied in later chapters.

2.1 Composite Material in Aviation Structures

2.1.1 Introduction of Composite Materials

In 1935, the first glass fibre was introduced, fiberglass. This is the beginning of the Fibre Reinforced Polymers (FRP) industry as it is known today. In aviation industry, fibrous composite was applied since the first flight of Wright Brothers' Flyer on 17th December 1903 [1]. Carbon fibre composite materials were first introduced in the 1960s developed by Royal Aircraft Establishment at Farnborough [2]. In its early stage, composite material was used for horizontal tail and landing gear doors on A320. Nowadays, A350 represents a milestone in aircraft design since more than 50% of the aircraft is made of composite and essential components such as wing box and fuselage are made of composite materials these days. Due to its high strength and low weight [3], composite material is becoming more and more popular in recent years. The trend of

composite materials usage for commercial aircrafts in the last few decades is shown in Figure 2.1.

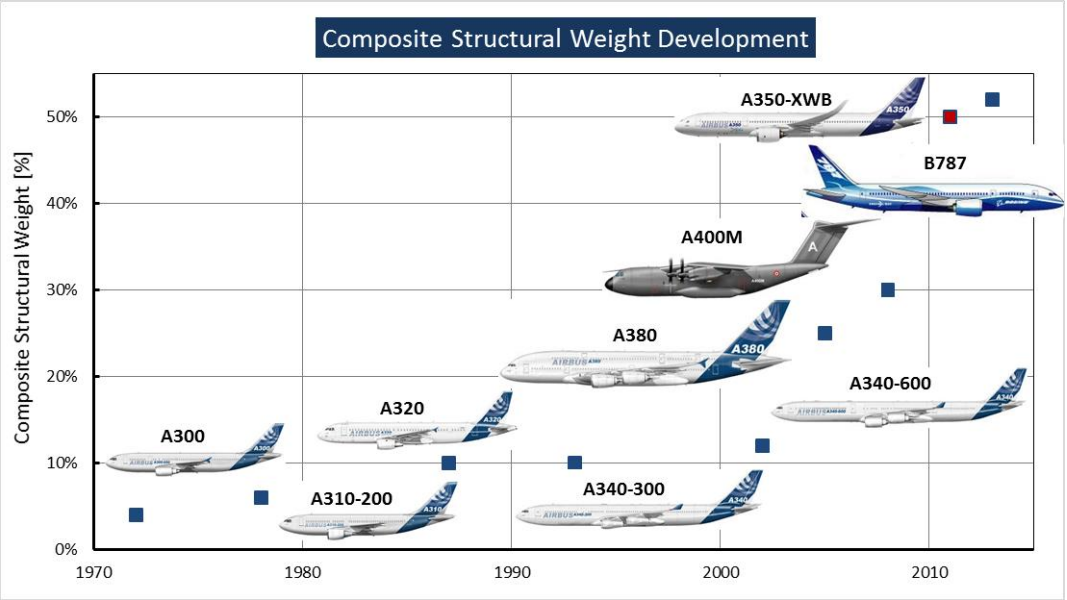

Figure 2.1 Usage trend for composite materials in commercial aircraft [4]

One of the reasons is that composite material has a high stiffness to weight ratio compare with traditional material such as alloy aluminium. With a general quasi-isotropic layup, composite material provides 20%-30% higher stiffness and 30% weight saving when compared with alloy aluminium which is widely used in aviation industry.

There are also disadvantages of composite materials. In spite of high raw material prices and difficulty in complex shape manufacture, from a structural engineer's point of view, impact [5], delamination [6-8], cut out [9, 10], composite joints [11-13] and difficulty in optimization [14-17] are challenges with further application of composite materials in real commercial aircraft design. Composite material will keep on developing rapidly with an aim to minimize weight and fuel consumption.

2.1.2 Mechanics of Composite Materials

Classical composite laminate theory is based on ply coordinate system (local coordinate system) and laminate coordinate system (global coordinate system). Ply stiffness of each ply in the ply coordinate system is transferred into laminate coordinate stiffness according to the angle θ between the ply coordinate system and the laminate coordinate system. With a specific stacking sequence of a laminate and ply thickness, the stiffness of the laminate can be determined. A, B, and D matrices are given in Eq. (2.1) [18].

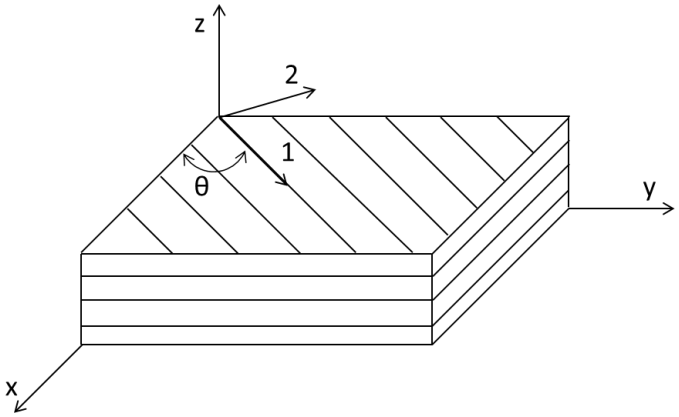

Figure 2.2 Ply and laminate coordinate systems

$$\begin{Bmatrix} N_x \\ N_y \\ N_{xy} \\ M_x \\ M_y \\ M_{xy} \end{Bmatrix} = \begin{bmatrix} \begin{bmatrix} A_{11} & A_{12} & A_{13} \\ A_{21} & A_{22} & A_{23} \\ A_{31} & A_{32} & A_{33} \end{bmatrix} & \begin{bmatrix} B_{11} & B_{12} & B_{13} \\ B_{21} & B_{22} & B_{23} \\ B_{31} & B_{32} & B_{33} \end{bmatrix} \\ \begin{bmatrix} B_{11} & B_{12} & B_{13} \\ B_{21} & B_{22} & B_{23} \\ B_{31} & B_{32} & B_{33} \end{bmatrix} & \begin{bmatrix} D_{11} & D_{12} & D_{13} \\ D_{21} & D_{22} & D_{23} \\ D_{31} & D_{32} & D_{33} \end{bmatrix} \end{bmatrix} \begin{Bmatrix} \varepsilon_x \\ \varepsilon_y \\ \gamma_{xy} \\ k_x \\ k_y \\ k_{xy} \end{Bmatrix} \quad \textbf{(2.1)}$$

Six commonly used composite failure criteria are list in Table 2.1. All these composite failure criteria are used to indicate a ply failure, but not the failure of the laminate. Maximum Stress/Strain Theory are non-interactive theories, which consider tensile stress/strain or compressive stress/strain individually. For other

criteria, both tensile and compressive stress/ strain are considered. Usually at least one non-interactive and one interactive criterion should be considered in composite component design.

Table 2.1 Failure criteria of composite materials [19]

Maximum Stress Theory	$f_1 < X_t, f_2 < Y_t;\ f_1 < X_c, f_2 < Y_c,\ \lvert f_{12}\rvert < S$
Maximum Strain Theory	$\varepsilon_1 < \varepsilon_{x_t}, \varepsilon_2 < \varepsilon_{y_t};\ \varepsilon_1 < \varepsilon_{x_c}, \varepsilon_2 < \varepsilon_{y_c},\ \lvert\varepsilon_{12}\rvert < \varepsilon_s$
Tsai-Hill Theory	$\left[\frac{f_1}{X}\right]^2 + \left[\frac{f_2}{Y}\right]^2 + \left[\frac{f_{12}}{S}\right]^2 - \left[\frac{f_1}{X}\right]\left[\frac{f_2}{X}\right] < 1, X = X_t \text{ or } X_c, Y = Y_t \text{ or } Y_c$
Hoffman Theory	$F_1 f_1 + F_2 f_2 + F_{11} f_1^2 + F_{22} f_2^2 + F_{33} f_{12}^2 + 2F_{12} f_1 f_2 < 1$ $F_1 = \frac{1}{X_t} - \frac{1}{X_c};\ F_2 = \frac{1}{Y_t} - \frac{1}{Y_c};\ F_{11} = \frac{1}{X_t X_c};\ F_{22} = \frac{1}{Y_t Y_c};$ $F_{33} = \frac{1}{S^2};\ F_{12} = \frac{-1}{2X_t X_c}$
Tsai-Wu Stress Theory	$F_1 f_1 + F_2 f_2 + F_{11} f_1^2 + F_{22} f_2^2 + F_{33} f_{12}^2 + 2F_{12} f_1 f_2 < 1$ $F_1 = \frac{1}{X_t} - \frac{1}{X_c};\ F_2 = \frac{1}{Y_t} - \frac{1}{Y_c};\ F_{11} = \frac{1}{X_t X_c};\ F_{22} = \frac{1}{Y_t Y_c};$ $F_{33} = \frac{1}{S^2};\ F_{12} = F_{12}^* / \sqrt{X_t X_c Y_t Y_c}$
Tsai-Wu Strain Theory	$G_1 \varepsilon_1 + G_2 \varepsilon_2 + G_{11} \varepsilon_1^2 + G_{22} \varepsilon_2^2 + G_{33} \varepsilon_{12_1}^2 + 2G_{12} \varepsilon_1 e_2 < 1$ $G_1 = F_1 Q_{11} + F_2 Q_{12};\ G_2 = F_1 Q_{12} + F_2 Q_{22};$ $G_{11} = F_{11} {Q_{11}}^2 + 2F_{12} Q_{11} Q_{12} + F_{22} {Q_{12}}^2;$ $G_{22} = F_{11} {Q_{12}}^2 + 2F_{12} Q_{12} Q_{22} + F_{22} {Q_{12}}^2;$ $G_{33} = F_{33} {Q_{33}}^2;$ $G_{12} = F_{11} Q_{11} Q_{12} + F_{12}\left(Q_{11} Q_{22} + {Q_{12}}^2\right) + F_{22} Q_{12} Q_{22}$

2.1.3 Design of Composite Wings

There are three main design phases of a composite wing design: preliminary design, detail design, and optimization, illustrated in Figure 2.3.

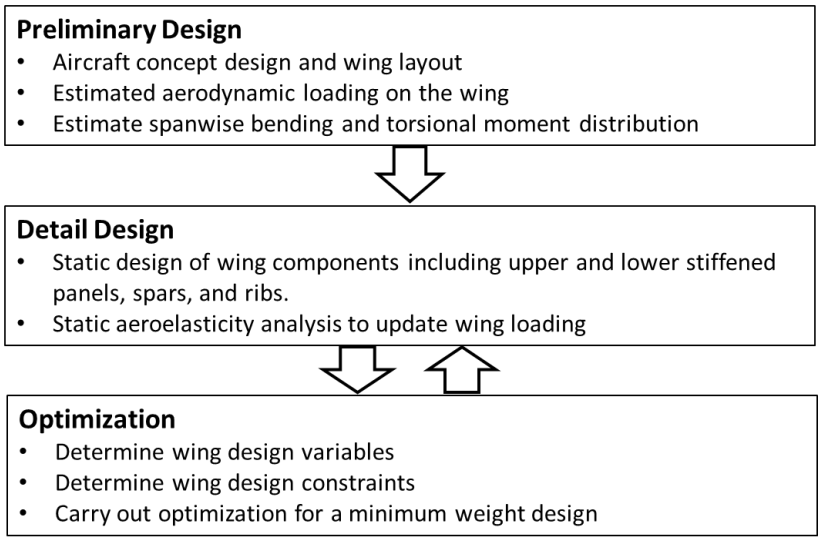

Figure 2.3 Composite wing design phases

At the initial design phase, the aircraft concept is frozen and wing configuration and layout are determined such as wing geometry and locations of spars. The aerodynamic load of the wing and spanwise bending and torsional moment can be calculated. By taking the structure and fuel mass into account the actual load distribution can be obtained.

In the detail design phase, optimal design of stiffened panels and components are carried out individually. By assembling these individual components, an initial design of a composite wing structure can be made. Classical analytical solutions for composite thin wall closed box section structures were developed by Vlasov [20] and Gjelsvik [21] and a beam model can be created to represent the composite wing for static and dynamic aeroelastic analysis.

In the optimization phase, not only optimization for a minimum weight can be carried out, but can be further developed for aeroelastic tailoring and other design purposed. Many previous studies were carried out in stacking sequence optimization of a composite laminates with strength and stability requirement to

achieve a minimum weight [17]. Composite material also provides potential of aeroelastic tailoring by laminate layup optimization [22, 23]. With these techniques, some difficulties in conventional design can be solved such as safety margin of stability of a seamless aircraft [24] and control problems for tailless air vehicles [25, 26].

2.2 Optimal Design of Stiffened Panels Subject to Instability

In this section, the techniques for optimal design of stiffened panels subject to stability are reviewed. This section starts with basic mechanism of buckling of a flat plate (Subsection 2.2.1) and extends to stringer stiffened panels (Subsection 2.2.2) and grid structures (Subsection 2.2.3). Emero's [27] optimal design method and Niu's practical design method [28] for optimal stringer stiffened panel design are discussed. Sandwich panel is reviewed in (Subsection 2.2.4).

2.2.1 Buckling of Flat Plates

The first part in this section presents a quick review of buckling of a rectangular flat plate simply supported along all four edges. In general, many methods are available to determine the critical buckling load of a flat plate such as the differential equation method, energy method [29], modified slope deflection method [30], direct method [31], and finite element method [32]. The energy based method for flat plate critical load estimation is reviewed in this section. For energy method, the estimation of critical buckling load of a flat plate is based on the estimation of the stationary value of the total potential energy of the equilibrating system.

$$\delta(\mathrm{U}+\mathrm{V})=0 \qquad \textbf{(2.2)}$$

where U and V are internal or strain energy and external load energy. The total potential energy of a deformed flat plate under bending load is defined as the summation of work done by the external bending load and bending deformation strain energy presented in Eq. (2.3).

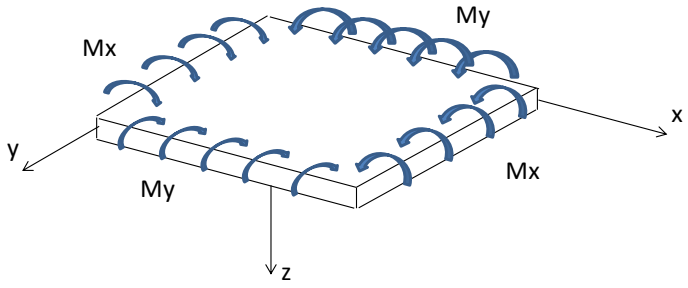

Figure 2.4 Pure bending of a plate

$$\mathrm{U+V}=\int_0^{\mathrm{a}}\int_0^{\mathrm{b}}\left\{\frac{\mathrm{D}}{2}\left[\left(\frac{\partial^2\mathrm{w}}{\partial\mathrm{x}^2}+\frac{\partial^2\mathrm{w}}{\partial\mathrm{y}^2}\right)^2-2(1-\mu)\left\{\frac{\partial^2\mathrm{w}}{\partial\mathrm{x}^2}\frac{\partial^2\mathrm{w}}{\partial\mathrm{y}^2}-\left(\frac{\partial^2\mathrm{w}}{\partial\mathrm{x}\,\partial\mathrm{y}}\right)^2\right\}\right]-N_x\left(\frac{\partial\mathrm{w}}{\partial\mathrm{x}}\right)^2\right\}\mathrm{dxdy} \tag{2.3}$$

where w is the displacement in the z direction and D is the flexural rigidity of the plate. With a given Fourier series plate deflection,

$$\mathrm{w}=\sum_{\mathrm{m}=1}^{\infty}\sum_{\mathrm{n}=1}^{\infty}\mathrm{A_{mn}}\sin\frac{\mathrm{m\pi x}}{\mathrm{a}}\sin\frac{\mathrm{n\pi x}}{\mathrm{b}} \tag{2.4}$$

where m and n represent half waves numbers in x and y directions. Substituting for w from Eq. (2.4) into Eq. (2.3) and performing the integration of Eq. (2.3) gives

$$\mathrm{U+V}=\frac{\pi^4 abD}{8}\sum_{m=1}^{\infty}\sum_{n=1}^{\infty}A_{mn}^2\left(\frac{m^2}{a^2}+\frac{n^2}{b^2}\right)-\frac{\pi^2 b}{8a}N_x\sum_{m=1}^{\infty}\sum_{n=1}^{\infty}m^2A_{mn}^2 \tag{2.5}$$

The differentiation of Eq. (2.5) with respect to unknown coefficient $A_{mn,}$ the Eq. (2.5) turns

$$\frac{\partial(U+V)}{\partial A_{mn}} = \frac{\pi^4 abD}{4} A_{mn}\left(\frac{m^2}{a^2}+\frac{n^2}{b^2}\right)^2 - \frac{\pi^2 b}{4a} N_{x,CR} m^2 A_{mn} = 0 \quad \textbf{(2.6)}$$

and the critical buckling load is

$$N_{x,CR} = \pi^2 a^2 D \frac{1}{m^2}\left(\frac{m^2}{a^2}+\frac{n^2}{b^2}\right) \quad \textbf{(2.7)}$$

Further simplification can be made by letting $k = \left(\frac{mb}{a}+\frac{a}{mb}\right)^2$ and considering $\sigma_{cr} = N_{x,CR}/t_s$

$$\sigma_{cr} = \frac{k\pi^2 E}{12(1-\mu^2)}\left(\frac{t_s}{b}\right)^2 \quad \textbf{(2.8)}$$

The buckling coefficient k is dependent on plate aspect ratio a/b and boundary conditions as shown in Figure 2.5. Eq. (2.8) can be further developed for stringer stiffened panel critical buckling load estimation [33].

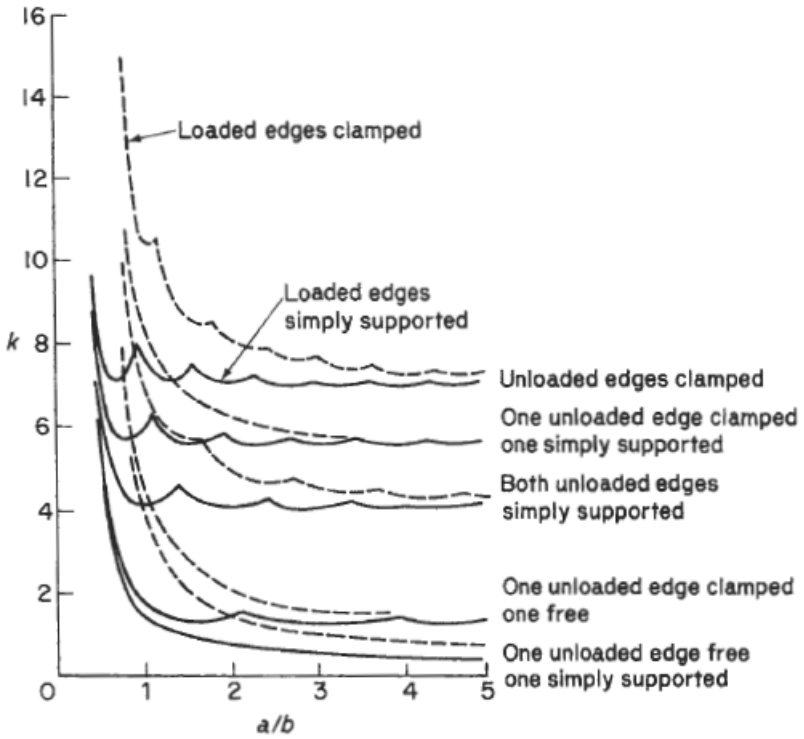

Figure 2.5 Buckling coefficient for flat plate [33]

To study the instability problems for a composite laminate flat plate, the bending stiffness of the plate should be calculated using classical lamination theory. It is developed from single ply stiffness with local ply coordinate system and transferring all ply stiffness into laminate global coordinate system to form laminate stiffness matrix as show in Eq. (2.1). In Eq. (2.1), matrix A represents in-plane stiffness resisting the in-plane tension and compression and matrix D represents bending stiffness. Matrix B shows bending and in-plane coupling stiffness for a specific layup laminate.

Take a symmetric layup composite flat plate as an example, bending and twisting coupling stiffness term D_{12} is taken into consideration for a more accurate estimation through Raleigh-Ritz method. The buckling stress turns to be Eq.(2.9) [34].

$$\sigma_{cr,min} = \frac{2\pi^2}{t_s b^2}\left[(D_{11}D_{22})^{\frac{1}{2}} + D_{12} + 2D_{66}\right] \quad \textbf{(2.9)}$$

It is shown in Eq. (2.9) that for composite buckling estimation bending and torsion coupling effect should be considered.

2.2.2 Stringer Stiffened Panels

Stringers are introduced to stiffen a flat plate by providing bending stiffness to resist buckling. Buckling modes of stringer stiffened panel can be categorized into global buckling and local buckling. A lower wing cover of A350 XWB stiffened with stringers is displayed in Figure 2.6.

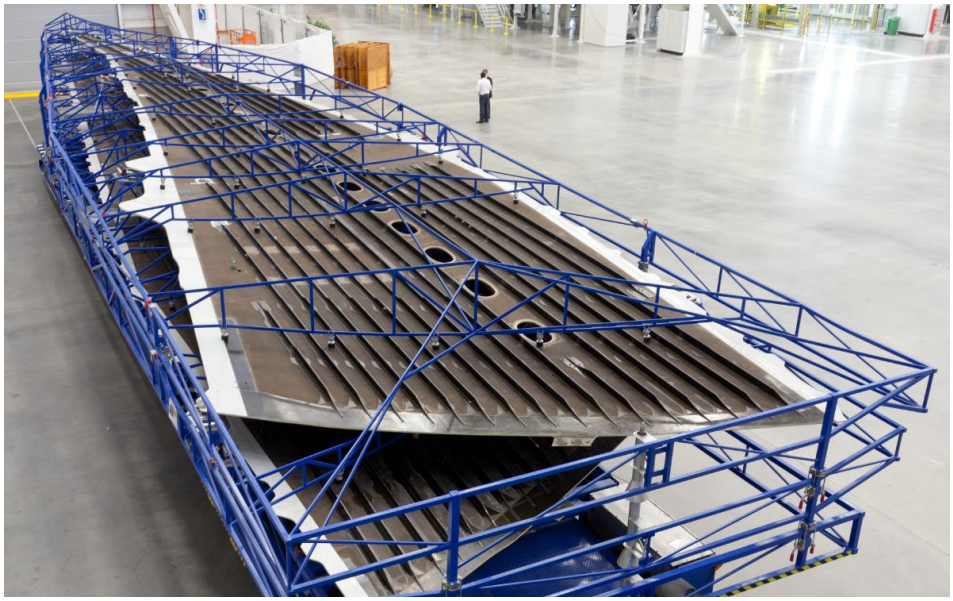

Figure 2.6 Lower wing cover of A350 XWB [35]

The critical buckling load is the minimum load applied on the structure to make the structure fall into global or local buckling mode. Both of the buckling modes should be estimated to determine the most critical buckling mode and the critical buckling load for the stringer stiffened panel. The critical local buckling load estimation of metallic stringer stiffened panel can be traced back to 1957 [36, 37]. Through these studies distributed moment method was developed for local buckling of stiffened panel with different stringer types [38]. Each stringer-skin section is divided into individual panel elements with elastic boundary conditions. The local buckling coefficient of the stringer-skin section is the buckling coefficient of the critical panel element at a certain geometrical configuration. Figure 2.7 shows the local buckling coefficient of blade stringer stiffened panel.

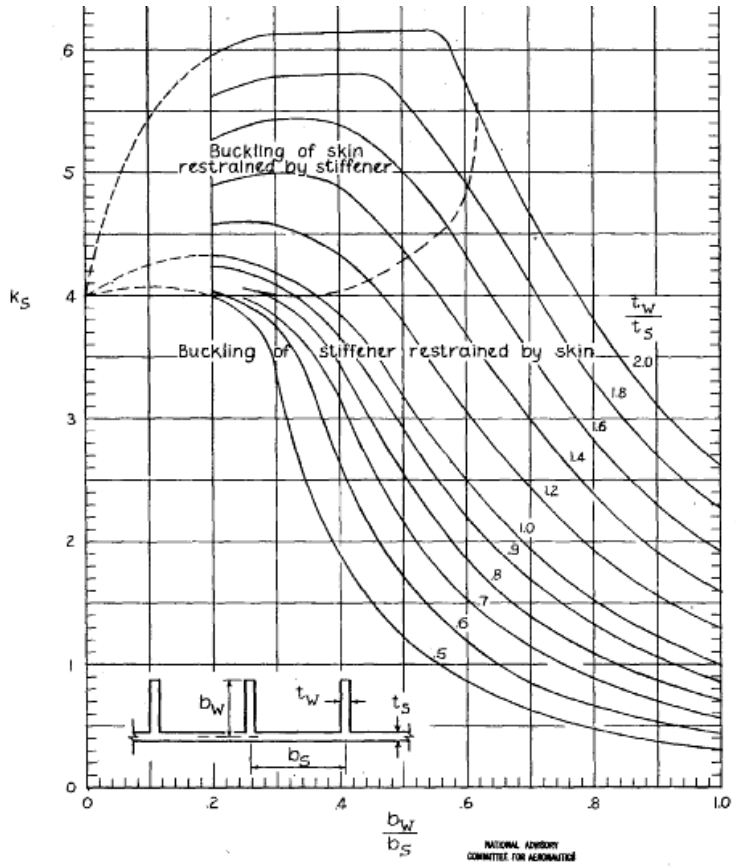

Figure 2.7 Local buckling coefficient for blade stringer stiffened panel [39]

Figure 2.7 shows that with the increase of stiffener height ratio (b_w/b_s), the location of critical local buckling changes from stiffener to skin. Local buckling coefficient increases with stiffener thickness to skin thickness ratio (t_w/t_s) at a specified stiffener height ratio. Global buckling of a flat plate has already been explained in Section 2.2.1 and an optimal design of stringer stiffened panel is to let global and local buckling to take place at the same buckling load.

Emero [27] introduces an optimal design method for metallic stringer stiffened panel by allowing the global buckling to take place along with the local buckling. The method is based on single stringer-skin strip with elastic boundary condition. The local buckling coefficient used in the method is calculated through moment distributed method and Euler's equation is used for global buckling estimation. An efficiency factor (ϵ) is introduced to measure buckling stress to weight ratio

between different stiffener types, see Table 2.2. It also provides efficiency evaluation method for different section dimension ratios to determine an optimal design set. Optimal design dimension ratios were listed with corresponding efficiencies [27].

Table 2.2 Emero's stringer stiffened panel efficiencies for three stringer types

Stringer Type	**Optimums Values**	**Auxiliary Relations**	**Dimensionless Geometric Expressions**
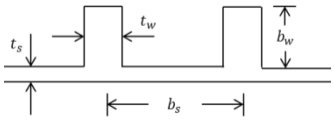 Blade	$\epsilon_{max} = 0.656$ $r_{bw} = 0.65$ $r_{tw} = 2.25$		$\alpha = 1 + r_{bw}r_{tw}$ $\beta = .5r_{bw}^2 r_{tw}$ $\gamma = .333r_{bw}^3 r_{tw}$
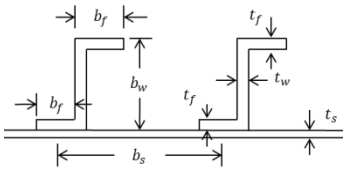 Z - Stiffened	$\epsilon_{max} = 0.911$ $r_{bw} = 0.87$ $r_{tw} = 1.06$	$r_{bf} = 0.3r_{bw}$ $r_{tf} = 1.0r_{tw}$	$\alpha = 1 + 1.6r_{bw}r_{tw}$ $\beta = .8r_{bw}^2 r_{tw}$ $\gamma = .633r_{bw}^3 r_{tw}$
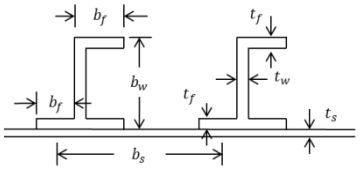 J - Stiffened	$\epsilon_{max} = 0.793$ $r_{bw} = 0.85$ $r_{tw} = 0.79$	$r_{bf} = 0.3r_{bw}$ $r_{tf} = 1.0r_{tw}$	$\alpha = 1 + 1.9r_{bw}r_{tw}$ $\beta = .8r_{bw}^2 r_{tw}$ $\gamma = .633r_{bw}^3 r_{tw}$

where α , β ,and γ are geometric expressions.

$$\frac{N_x}{L * E} = \epsilon * \left(\frac{\bar{t}}{L}\right)^2 \quad \textbf{(2.10)}$$

$$\mathrm{b}_s = \left[\frac{N_x L^2}{\pi^2 E \bar{t}} \frac{\alpha}{\gamma - \frac{\beta^2}{\alpha}}\right]^{1/2} \quad \textbf{(2.11)}$$

$$\rho_G = \mathrm{b}_s \left[\frac{\gamma - \frac{\beta^2}{\alpha}}{\alpha}\right]^{1/2} \quad \textbf{(2.12)}$$

$$\mathrm{t}_s = \frac{\bar{t}}{\alpha} \quad \textbf{(2.13)}$$

Niu [28] provides design ratio ranges of stringer stiffened panel design parameters based on practical design experiences. These design parameters are defined from Eq. (2.8) since each stringer stiffened panel elements are treated as individual rectangular panel for critical buckling stress estimation. A recommended stringer section area to skin section area ratio is 0.5 and the same buckling stress at each individual rectangular panel element from the stringer stiffened panel section was assumed to get detail dimensions from Niu's method [28], see Table 2.4. These design parameters are given in Table 2.3 and manual modification should be made to ensure the ratios are within the ranges.

Table 2.3 Niu's practical design ratios [28, 40]

$\frac{b_a}{t_a}$	$\frac{b_w}{t_w}$	$\frac{b_f}{t_f}$	$\frac{A_{St}}{A_{Sk}}$	t_a	$\frac{b_f}{b_w}$
10 or less	18 - 22	6 - 8	0.5	0.7 t_s	0.4

Table 2.4 Niu's definitions and equations [28, 40]

Elements	Applied Equations	Remarks
t_s	$t_s = \frac{N}{(1+\frac{A_{st}}{A_{sk}})}$	
A_{st}	$A_{st} = \left(\frac{A_{st}}{A_{sk}}\right) b_s t_s$	
b_f	0.327 b_w	
t_{fs}	$t_f \approx t_w$	
b_w	$b_w = \left[\left(\frac{b_w}{t_w}\right)\left(\left(\frac{A_{st}-2b_a t_a}{1.327}\right)\right)\right]^{\frac{1}{2}}$	
t_w	$\frac{b_w}{\frac{b_w}{t_w}}$	
b_a	$2.08t + 0.688$ if $t \leq 0.3$ 1.312 if $t > 0.3$	b_a=0 for integral panel
t_a	$t_a = 0.7t_s$	t_a=0 for integral panel

With the application of composite materials, many research efforts have been made to develop an optimal design of composite stringer stiffened panels. Study initially applied on laminate plates, both symmetric and unsymmetrically composite flat plate [41, 42]. Vescovini and Bisagni [43] applied an optimization method to achieve a minimum weight design of composite stiffened flat and curved panels. Harrison [44] applied a genetic algorithm and a response surface approximation method in optimization of a composite stringer stiffened panel design to achieve a minimum weight. Optimal design of a composite stringers stiffened panel is still an attractive topic for many researchers.

2.2.3 Grid Structure

Grid structures are widely used in aerospace industry because of the advantages of their low-cost, long-lasting, and light-weight in enhancing the panels. Curved grid-structure-stiffened panels and shells are desirable building components in resisting buckling. In aviation industry, The McDonnell-Douglas Corporation (now part of The Boeing Company) holds the patent rights for development of the first aluminium isogrid, the earliest precursor of the modern Advanced Grid Structure (AGS). It has been studied for many decades for its potential to replace stringer stiffened panels, and sandwich panels [45]. An example of grid structure is shown in Figure 2.8.

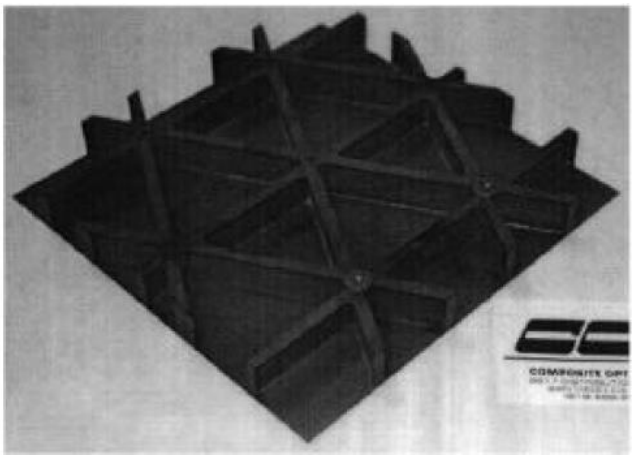

Figure 2.8 Grid structure [45]

In 1970, buckling behaviour of reticulated shell structures was studied by Forman and Hutchinson et al. [46] through an approximate equivalent shell analysis method and a discrete analysis method. Yamashita [47] investigated both metallic linear and elastic buckling characteristics of two-way grid shells of single layer. With the widely application of composite materials, Bert et al. [48] developed a differential quadrature method which is used for analysing buckling behaviour of anisotropic rectangular plates under various boundary conditions.

For cylindrical structures, Helms et al. [49] studied bending stiffness of cylinders stiffened with grid structures with in-plane loading condition as a preliminary stage for further analysis and trying to develop an optimization analysis. Kidane et al. [50] studied global buckling load of a cross and horizontal composite cylinder with grid stiffeners. A unit cell model was created and the equivalent bending stiffness of the cell is a superposition of the contribution of the stiffeners and the stiffness contribution of the shell. Energy method was applied for buckling load solution and buckling test was performed for a comparison. Delamination effect on buckling behaviour of a composite grid structure was investigated by Bai et al. [51] through numerical analysis method of a finite element model consists of a composite laminate element and 3 beam elements. The effects of configuration, size, and location of the delamination were modelled and the geometry effect of the stiffener was discussed. The results showed that the buckling load and modes are closely related to these parameters [51].

In 1996, Chen and Tsai [52] carried out a method of optimum design on an integrated equivalent stiffness model of a grid structure under in-plane bending and shear loading. The method considered multiple loads and failure mechanisms along with discrete design. The performance of the structure was compared with conventional laminates and metal grid structures. Jaunky et al.

[53] developed an optimal design strategy subject to global and local buckling for grid panels and shells. An improved smeared stiffener theory is used for global buckling and local buckling of skin and stiffeners were estimated separately. A large number of design variables including geometry and material properties parameters were considered in a discrete optimizer to achieve a minimum weight design. Similar work on grid panels and shells with curvature were studied by them later [54].

Bradshaw et al. [55] discussed the development of special structures for space frames or grids and pointed out its potential trends and evolution in the future. Gatta and Romano [56] introduced a design approach for fuselage barrel with composite grid structures. The approach starts from an analytical theory design and followed with FE model analysis with optimum design a minimum weight was achieved with 20% reduction in weight compare with a metallic reference baseline with a 30% reduction in manufacturing cost. In the near future, advanced grid structure may take the place of stringer stiffened panel and sandwich panels in aviation industry.

2.2.4 Sandwich Panel

Sandwich panel is another widely used structure type in aviation industry usually intended for control surfaces. It is easy to manufacture such structures and a lower cost involved when compared with stringer stiffened panel and grid structures. In general, sandwich panel is made of two top and bottom surfaces and filled with a core between the two surfaces. There is variety of combinations of surfaces and core materials starting from paper, wood, metal, to composite materials and some examples are shown in Figure 2.9.

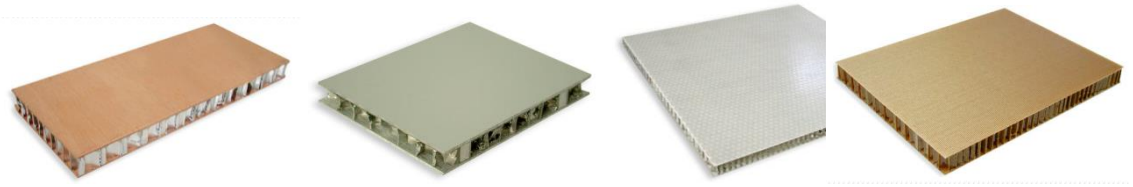

a) b) c) d)

Figure 2.9 Sandwich panel with different materials [57]

a) Wood/Aluminium b) Aluminium/Aluminium

c) Fiberglass/Aluminium d) Fiberglass/Nomex Honey Comb

In 1973, early research work on buckling load of composite sandwich panels based on experiments was carried out by Pearce and Webber [58] to determine global buckling and wrinkling loads for carbon fibre composite sandwich panels with in-plane pure compression load. Noor et al. [59] summarized computational models for sandwich panel and shells in his literature review including bifurcation buckling, local buckling, wrinkling, and post buckling. Experimental studies, optimization studies as well as geometrical considerations were all covered in this literature review. Some further work and future directions were also pointed out and outlined. Librescu and Hause [60] gave a summary about some developments during that time on modelling and stability of sandwich structures.

For in-plane loading, Frostig introduced a high order theory in buckling loads calculation for sandwich panel under compression load and concluded that for some structure configurations, local buckling is more critical than global buckling due to flexibility in out-of-plane [61, 62]. Post buckling behaviour of a geometrically imperfect sandwich panel was studied and the influence of design parameters with boundary conditions on stability was outlined and discussed [63].

The out-of-plane compressive behaviour was investigated by Côté et al. [64] on metallic honeycombs. With the introduce of transverse pin and applied on reinforcement of sandwich panels, the effect of this technique was studied and shows the pins cannot only improve stability against elastic buckling but also provide significant strength [65].

To achieve a minimum weight, many optimization algorithms were introduced and investigated [66, 67].

Some other related disciplines were also developed. Self-healing composite sandwich structures were investigated by Willams et al. [68]. The aim of this self-healing composite sandwich structure is to recover structure surface damage caused by impact and localized skin buckling. Zhang and Ashby studied the out-of-plane properties of honeycombs, which is used as the sandwich core, considering buckling, debonding, and fracture. The result shows their model has good agreements with earlier data and experiments [69].

2.2.5 Summary

In this section, the instability of metallic and composite plates has been discussed in Section 2.2.1. Back ground information, design and optimization methods of stringer stiffened panel, grid structure, and sandwich panels have been discussed and reviewed both for metallic and composite structures, see Section 2.2.1. Most of the research works discussed are focused on individual structure type and a crosswise comparison would be more helpful to structural engineer to determine the most appropriate structure type under a specific loading condition, see Section 2.2.2 to Section 2.2.4.

2.3 Morphing Structures

2.3.1 Morphing Techniques

The interest on morphing techniques has been increasing during the last decade due to their potential in enhancing aircraft performance and efficiency within a wide range of operating conditions. Beyond an improvement in the aerodynamic performance, it also has the potential to reduce noise emission

and save structural weight [70]. Although just a few of those concepts are shown to be practical and they are still far from real life applications, there are a growing number of researchers involved in developing new morphing techniques [71-74] and the research is no longer in its infancy.

Morphing structures can be categorized according to morphing methods: a) using internal mechanisms, b) piezoelectric actuation, and c) shape memory alloys (SMAs) actuation. The examples of these methods are shown in Figure 2.10.

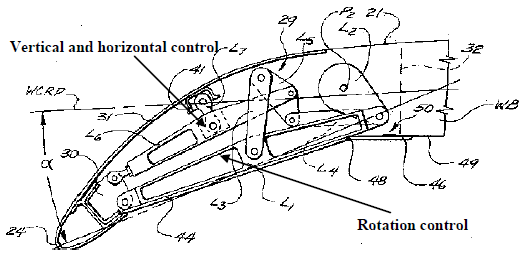

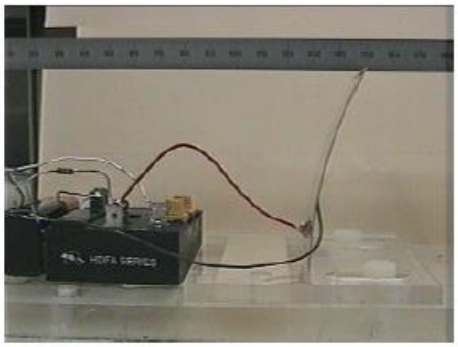

a) Internal mechanisms morphing [75] b) Piezoelectric actuation morphing [76]

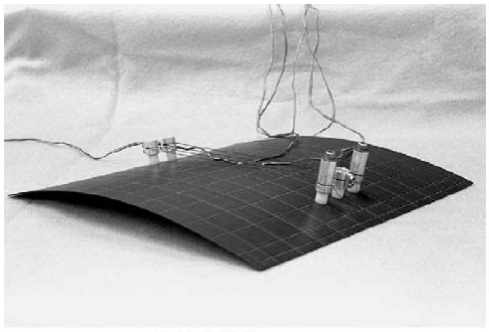

(a) $[90_4/0_4]_T$ laminate

c) Shape memory alloys morphing [77]

Figure 2.10 A classification of morphing aircraft by morphing methods

Most of the morphing methods of internal mechanisms are unable to avoid increasing considerable structure weight which in turn reduces their efficiency.

Piezoelectric actuation and SMAs can be used as an ideal actuation solution for morphing concepts without any considerable weight penalty, but they are limited in their output power and some of them might damage original structure resulting in loss of strength.

2.3.2 Morphing Techniques in Aviation Industry

Morphing techniques can also be categorized according to their morphing concepts into three main classes, namely, platform alternation, aerofoil profile adjustment, out-of-plane transformation [74], and see Figure 2.11 below.

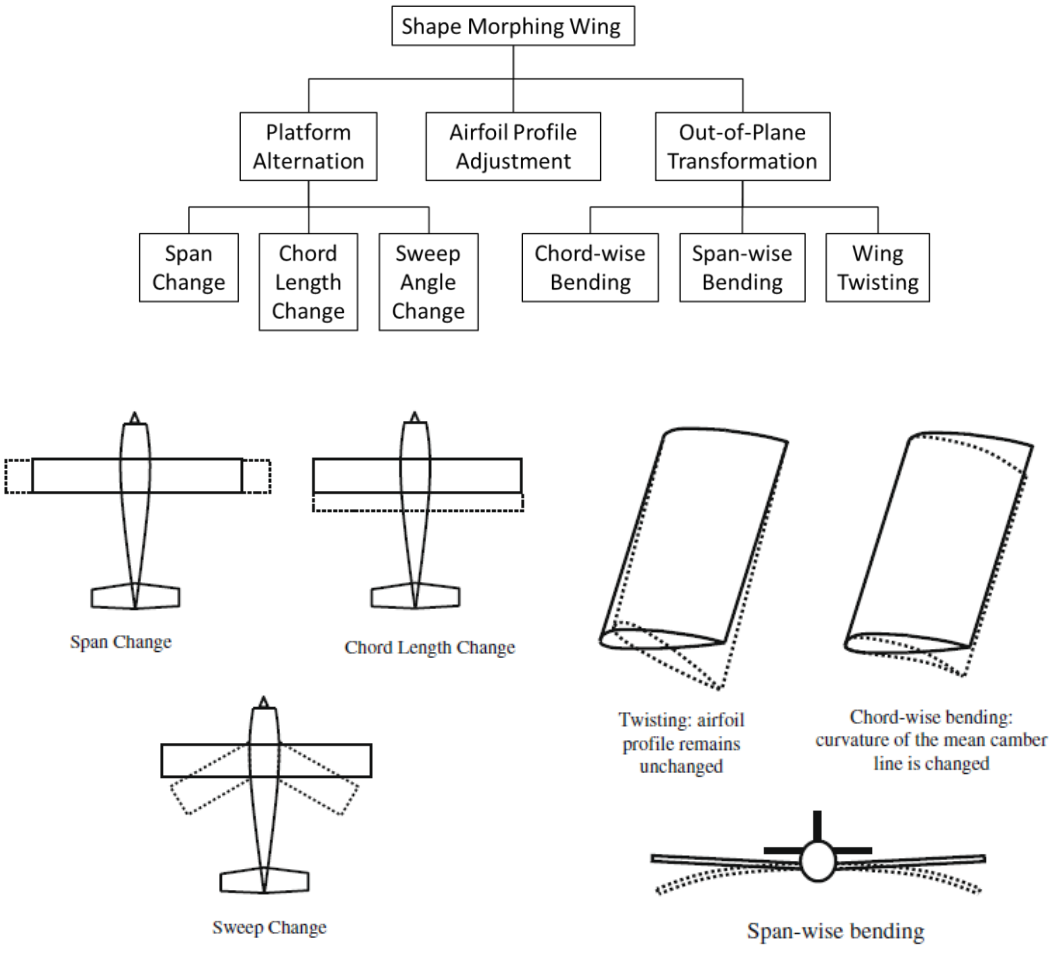

a) Platform Alternation b) Out-of-Plane Transformation

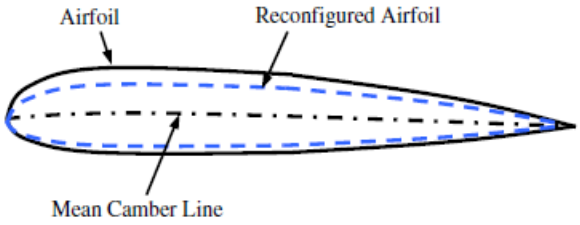

c) Air foil Profile Adjustment

Figure 2.11 A classification of morphing aircraft [74]

As an example of platform alternation, Grumman F-14 Tomcat as shown in Figure 2.12 is a multi-mission fighter aircraft with variable-sweep wing to meet its design targets as a platform for both an air superiority fighter and a long-range navel interceptor.

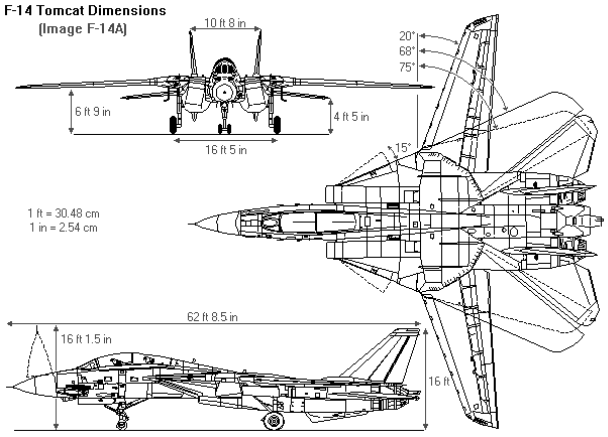

Figure 2.12 F-14 a variable-sweep wing multi mission fighter [78]

Sofla et al. [74] investigated an antagonistic SMA-actuated flexural structure concept. One of their two different concepts is shown in Figure 2-13, which is an example of out-of-plane transformation.

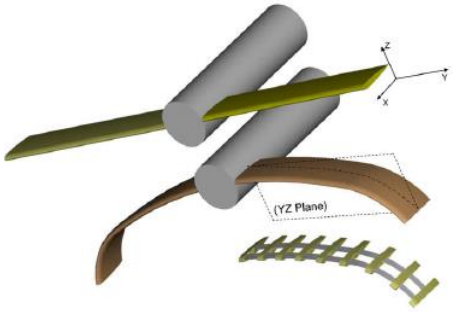

Figure 2-13 A transvers reforming wing concept [74]

To conclude, a successful design of morphing concept should achieve a balance among weight penalty due to actuation system, flexibility, strength, and instability problems.

2.3.3 Morphing High Lift Devices

There are various morphing concepts to achieve different objectives [70, 73, 79]. In order to have a high aerodynamic efficiency, configuration without a significant weight penalty, high lift devices are the most effective choice to be designed to morph. In this section the study is focused on morphing concepts for wing high lift devices of a subsonic commercial aircraft. Among the three morphing methods mentioned in the last section, the internal mechanism morphing concept is comparatively more reliable, efficient and safer for commercial aircraft. Some of the morphing high lift concepts are reviewed in this section with discussion on these concepts. Figure 2.14 is SADE project for smart high lift devices for next generation wing project [80].

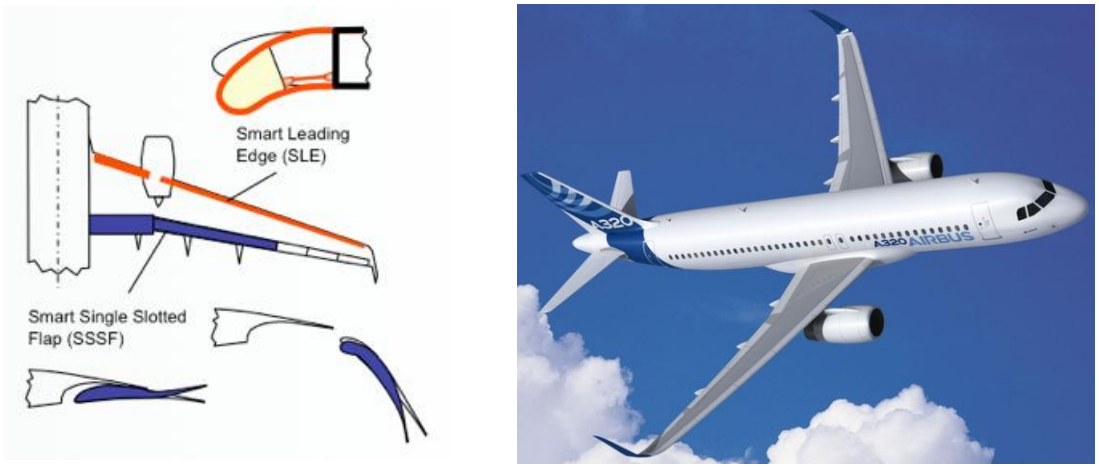

Figure 2.14 Smart lift devices for next generation wing [80]

As one of the essential high lift devices for take-off and landing, leading edge with morphing concepts were studied and according to the definition in the last section, morphing leading edges are out-of-plane morphing concepts. Regarding the actuation types, morphing leading edge concepts can be categorized into two main mechanism types, namely, linkage actuation system and an eccentric actuation beam system. The linkage system due to reliability has been applied in many morphing leading edge concepts. Airbus developed a drop nose system for A380 and it improves aerodynamic performance benefit from seamless morphing design [81].

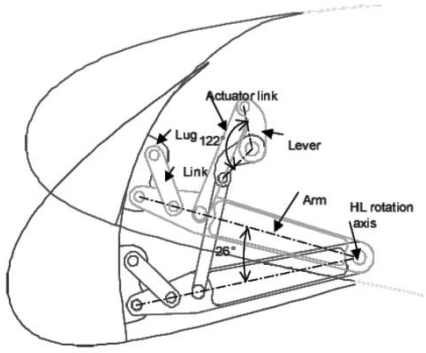

Figure 2.15 Airbus drop nose concept [81]

Guo developed an eccentric beam actuation beam concept [82, 83] as illustrated in Figure 2.16 based on the DAPAR's Eccentuator Beam Concept as illustrated in Figure 2.17. By rotating the beam from 0-90 degree, leading edge surface can deform along with the beam to meet the aerodynamic target shapes at any angle, see Figure 2.17.

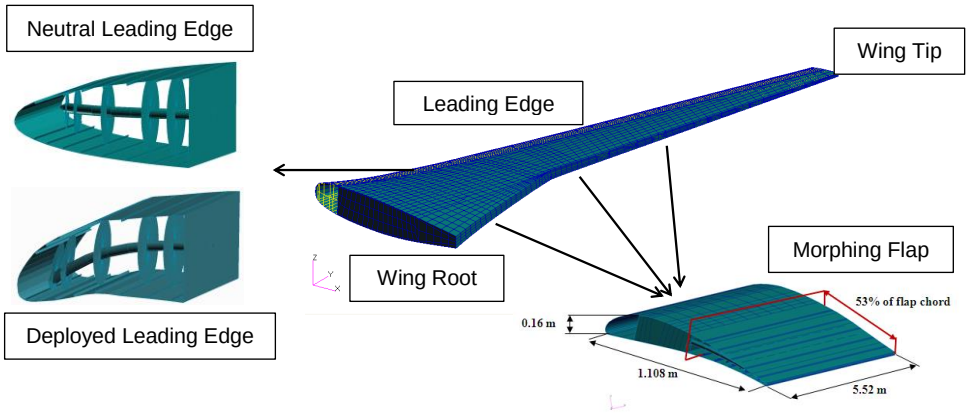

Figure 2.16 Morphing leading edge with eccentuator beams

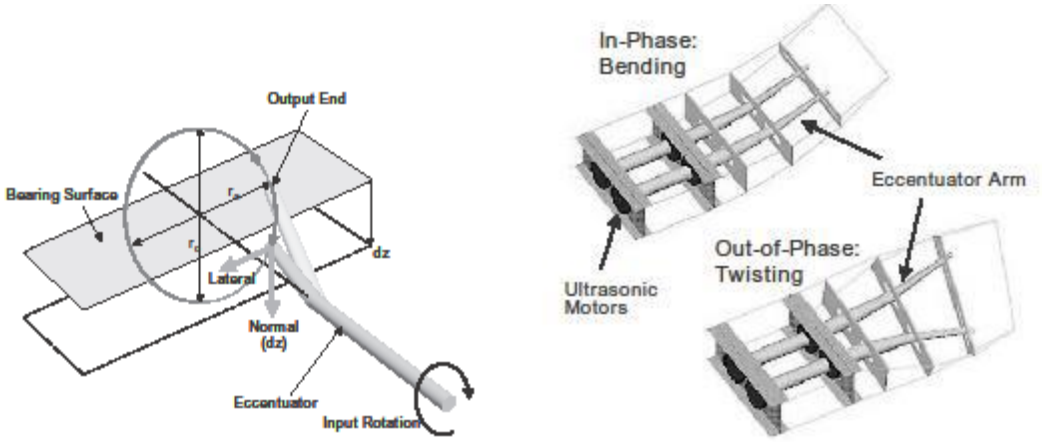

a) b)

Figure 2.17 An eccentuator beam concept [82]

For morphing flaps or trailing edge, Yin [84] studied a variable trailing-edge camber wing concept and the stiffness requirement of flexible skin of the concept. The main conclusion drawn is that a critical bending stiffness can be determined that beyond a value, in-plane stiffness has no contribution to the deformation of flexible skin [84]. Wildschek et al. [85] applied a morphing trailing edge device with electric actuation system on a composite blended-wing-body (BWB) aircraft for flight control. BWB configuration is a highly viable proposition

in the long term for its fuel efficiency in long-range transportation, but has difficulty in its control. Morphing trailing edge would help to overcome this problem with limited weight penalty. Pecora et al. [86] use morphing trailing edge to provide high efficiency aerodynamic profiles for different flight conditions.

In order to develop efficient morphing concepts, enormous efforts have been devoted to other related techniques to achieve an efficient design. To obtain a continuity surface wing, Chen et al. [87] introduced a genetic algorithm to minimize the error between aerodynamically optimized target structure shape and the deformed structure profile. A systematic approach is introduced by Liu et al. [88] to design compliant structures for a shape to meet design requirements. Optimization algorithms are also studied for target shape optimization for a most efficient morphing design. Secanell et al. [89] developed an optimization computer program based on a computational fluid dynamics solver and a sequential-quadratic algorithm to obtain a set of optimal airfoils. Power consumption of actuation system is another concern for morphing concept design. Gern et al. [90] investigated actuation power calculation to meet a morphing concept requirement and compared with conventional wing with traditional trailing edge flaps.

In this section, most of the morphing concepts reviewed are used to improve aerodynamic performance. These concepts can be categorized into linkage actuation and eccentuator beam systems. Although linkage actuation morphing system takes advantage of reliability, the eccentuator beam system has less weight penalty and comparatively more efficient.

2.4 Aeroelasticity

In the early aviation ages, flight speed was comparatively low and relatively low load was applied on the wing which resulted in less deformation and aerodynamic load variation. Structure engineers considered aircraft as a rigid body neglecting interaction among aerodynamic load, elastic structure response and inertia load. With the increasing flight speed and quest for minimum weight design aircraft designers met a wide range of problems during the World War II now categorised as aeroelastic problems. Collar introduced a triangle of interaction relationships among forces [91]. Aerodynamic force, elastic structure force and inertial force are included in this triangle [91] and aeroelastic phenomena are placed according to related forces as illustrated in Figure 2.18.

According to Figure 2.18, aeroelastic phenomena can be categorized based on their effect on aircraft design as flutter, buffeting, dynamic loads problems, load distribution, divergence, control effectiveness and reversal. Literature review in this section emphasised on flutter, dynamic loads problems, and load distribution. These topics can be further categorized into static aeroelasticity (static load distribution) and dynamic aeroelasticity (flutter, gust etc. as dynamic problems).

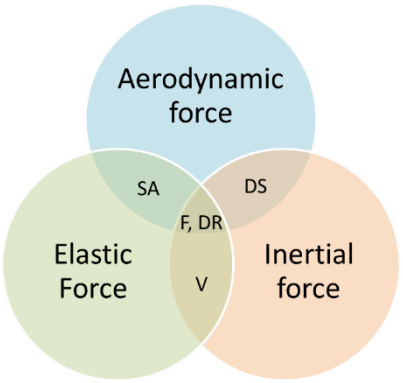

SA: Static Aeroelasticity F: Flutter DR: Dynamic Response

V: Vibration DS: Dynamic Stability

Figure 2.18 Aeroelasticity interactions

In this section, contents are divided into static aeroelasticity and dynamic aeroelasticity. In the static elasticity part, a review on aerodynamics force and structure stiffness coupling based on two different methods is carried out. On the dynamic aeroelasticity part, a review on the dynamic vibration motion equation and Theodoson's unsteady aerodynamics equation follow with review on flutter and gust development.

2.4.1 Static Aeroelasticity

Static aeroelasticity is the interaction between aerodynamic force and elastic force as displayed in Figure 2.18. From its definition, the time dependent terms are eliminated which leads to no velocity and acceleration terms in the equilibrium equations. In this way, damping force and mass properties have no effect on these phenomena. Since the flow in static aeroelasticity has been treated as steady flow, naturally steady aerodynamics tools can be applied to such problems avoiding complex unsteady aerodynamic load computation.

Static aeroelastic phenomena can be further subdivided into two classes mentioned in the introduction of this section. The first class includes load distribution and divergence. In this class, the aeroelastic effect due to an interaction between aerodynamic load and structural response is studied. Structural engineers work with these phenomena in aircraft design. The second class contains control and aircraft stability. These phenomena add control systems in elastic structure response and focus on stability and manoeuvre problems. Control system engineers concentrate on this class. As this piece of research work is mainly based on from a structural engineer's point of view, only the first class of phenomena related to load distribution and divergence are reviewed [92].

The static aeroelastic divergence problem is related to structural stiffness and artificial aerodynamic stiffness. An example of a cantilever uniform beam is given in Eq. (2.14) and Eq. (2.15).

$$K_b = {M}/{\emptyset} = {3EI}/{l}, \quad K_t = {T}/{\theta} = {GJ}/{l} \tag{2.14}$$

$$h_s = K_b + K_t$$

$$h_a = {H}/{\delta} = \frac{1}{2}\rho V^2 s_a {C_a}^2 b_2 \tag{2.15}$$

where $\emptyset = \mathrm{w}/\mathrm{l}$, $\theta = \mathrm{T} * \mathrm{l}/\mathrm{GJ}$ and w is out-bending-plane displacement.

The hinge moment acting on the control surface depends on structural stiffness and aerodynamic stiffness along with an equilibrium angle δ_e.

$$\mathrm{M} = (h_s + h_a) * \delta_e \tag{2.16}$$

The control surface divergence occurs when the magnitude of aerodynamic stiffness h_a equals to the structure stiffness h_s with a different sign. So the Divergence velocity can be determined as in Eq. (2.17)

$$V_{DIV} = \left(\frac{2h_s}{\rho s_a {C_a}^2 b_2}\right)^{\frac{1}{2}} \tag{2.17}$$

Using similar procedure, fuselage divergence equation can be developed Eq. (2.18).

$$V_{DIV} = \left(\frac{2K_b}{\rho s_f a_{1f} l_f}\right)^{\frac{1}{2}} \tag{2.18}$$

Due to aerodynamic force, a bending and torsional coupling effect is acting on the wing. Since the aerodynamic centre is generally ahead of the wing neutral axis, a nose up pitching moment is generated and results in an increase of angle of attack of the local section. In the linear region of lift coefficient C_L, the lift will increase and result in another increase in the angle of attack until a

stable point is met between aerodynamic force and structure elastic force. A swept forward wing design would enhance this twist divergence.

On the other hand, bending and torsion coupling on a swept back wing design leads to a nose down in the free stream direction, which consequently decreases the local free stream direction angle of attack further decreasing the lift of the wing section. Since less deflection in the inboard section, the load tends to shift from outboard to inboard as a compromise of the twist divergence and bending-torsion coupling effects.

Two methods can be employed in this load distribution problem as aerodynamic force and structure deflection iterations or direct aerodynamic stiffness and structure stiffness coupling. Aerodynamic force and structure deflection iterations can be carried out in the way of set up iteration of applying aerodynamic force to the structure and get the structure deflection for updating the aerodynamic force then repeat the iteration until it converges within an acceptable error range. To achieve a target lift for a wing (considering cruise condition lift), a two-stage loop should be carried out. The first stage is to find the stable defection under a specific angle of attack of the wing and the second stage is adjusting the angle of attack to adjust lift generated from the deformed wing. This method takes advantage of a simple coupling method with comparatively separate calculation for aerodynamic force estimation and structure deformation estimation. The shortcomings are that iterations should be carried out and data transfer from aerodynamic model to structure model maybe complex and take considerable work and cost.

An alternative way is to set up direct relationship between structural displacement and aerodynamic lift so that the structural stiffness and aerodynamic stiffness can be involved in one function. Aerodynamic model and structure model can be set up at the same time and set up splines to combine

structure deflections and the aerodynamic model deflections. A general form of a lift expression with aerodynamic model deflection in the usual notation is shown in Eq. (2.19).

$$\{P_k\} = \bar{q}[S_{kj}]\left([A_{jj}]^{-1}[D^1_{jk} + ikD^2_{jk}]\{u_k\} + \{w_j^g\}\right) \quad \textbf{(2.19)}$$

$\{u_k\}, \{P_k\}$ Displacements and forces at aerodynamic grid points

$[S_{kj}]$ Forces due to pressures at the aerodynamic control points

$[A_{jj}]$ Aerodynamic influence coefficient matrix, a function of Mach number (m), and reduced frequency (k)

$[D_{jk}]$ Substantial derivative matrix for the aerodynamic displacements

$\{w_j^g\}$ Downwash at Initial condition without structure deflection

Aerodynamic methods can be applied to compute the matrices $[S]$, $[D^1]$, $[D^2]$, and $[A_{jj}]$. An interpolation matrix $[G_{kg}]$ is introduced to relate structure gird points' deflections to the deflection of the aerodynamic grid points as shown in Eq. (2.20).

$$\{u_k\} = [G_{kg}]\{u_g\} \quad \textbf{(2.20)}$$

$\{u_k\}, \{u_g\}$ Displacements at aerodynamic grid points and structure points

Different spline theory models can be applied to obtain interpolation matrix $[G_{kg}]$.

For steady flows, there is no image part and rewrite Eq. (2.19) to get the aerodynamic stiffness in the structure model form with an empirical correction factor matrix $[W_{kk}]$.

$$[Q_{aa}] = [G_{ka}]^T[W_{kk}][S_{kj}][A_{jj}]^{-1}[D_{jk}][G_{ka}] \quad \textbf{(2.21)}$$

$[Q_{aa}]$ The forces at the structural grid points due to structural deformations

$[G_{ka}]$ The spline matrix

$[W_{kk}]$ A matrix of empirical correction factors to adjust each theoretical aerodynamic box lift and moment to agree with experimental data for incidence changes

Giesing, Kalman, and Rodden [93] suggested one way of obtaining these factors.

With the introduction of the aerodynamic influence coefficient matrix $[Q_{aa}]$, aerodynamic force can be directly applied to structure model and it varies along with structure deflection. This is also considered as aerodynamic stiffness subject to structure deflection. By introducing this aerodynamic stiffness matrix to the structure model a complete static aerodynamic model can be set up as in Eq. (2.22)

$$[K_{aa} - \bar{q}Q_{aa}]\{u_a\} = \bar{q}[Q_{ax}]\{u_x\} + \{P_a\} \quad \textbf{(2.22)}$$

$[K_{aa}]$ Structural stiffness matrix
$\bar{q}$ Flight dynamic pressure
u_a Structural displacement
u_x Aerodynamic control surface deflections and overall rigid body motions
$\{P_a\}$ Vector of applied loads
$[Q_{ax}]$ The forces at the structural grid points due to unit deflections of the aerodynamic extra points

This is the general equation for a direct coupling used for static aeroelastic analysis.

2.4.2 Dynamic Aeroelasticity

Dynamic aeroelasticity is a class of phenomena related to aerodynamic force, structure elastic force, and inertia force. The general dynamic motion equation is shown in

$$Ma + Dv + Ku = F \tag{2.23}$$

M, D, K	Mass, Damping, and Stiffness terms
a, v, u	Acceleration, Velocity, and displacement terms
F	Force terms

M is the structure mass, while damping terms including structure damping and aerodynamic damping terms are denoted by D. External force applied on the structure can be a pure unsteady aerodynamic force (flutter) or a combination of unsteady aerodynamic force along with a specific given load function (gust). The unsteady aerodynamics in Eq. (2.23) makes it difficult to solve for dynamic aeroelasticity analysis. In 1935, Theodorsen [94] first developed a reduced frequency method for flutter analysis in America. Much earlier, Frazer and Duncan [95] in England solved flutter problems with frequency dependent stiffness and damping terms. Lawrence and Jackson [96] compared these two methods and Hassig [97] further developed Frazer and Duncan's method by introducing complex springs to replace aerodynamic loads, which is later named p-k method. The following section gives a brief review of unsteady aerodynamics and methods for further discussion and literature review on dynamic aeroelasticity phenomena such as flutter and gust.

2.4.2.1 Unsteady Aerodynamics

In 1935, Theodorsen [94] solved flutter problem by introducing a complex function of reduced frequency k.

$$C(k) = F(k) + iG(k) = \frac{H_1^{(2)}(k)}{H_1^{(2)}(k) + iH_0^{(2)}(k)} \tag{2.24}$$

where $H_n^{(2)} = J_n - iY_n$, which is a combination of Bessel functions. Lift and pitching moment can be written as

$$L = \pi\rho b^2\left[\ddot{h} + U\dot{\alpha} - ba\ddot{\alpha}\right] + 2\pi\rho UbC(k)\left[\dot{h} + U\alpha + b\left(\frac{1}{2} - a\right)\dot{\alpha}\right] \tag{2.25}$$

$$M_y = \pi\rho b^2 \left[ba\ddot{h} - Ub\left(\frac{1}{2} - a\right)\dot{\alpha} - b^2\left(\frac{1}{8} + a^2\right)\ddot{\alpha} \right]$$
$$+ 2\pi\rho U b^2 \left(a + \frac{1}{2}\right) C(k) \left[\dot{h} + U\alpha + b\left(\frac{1}{2} - a\right)\dot{\alpha} \right]$$

In Eq. (2.25), the parameter b and a represent the semi-chord and the distance from semi chord over semi chord length respectively. An example of definition of $a = -0.9$ is given in Figure 2.19.

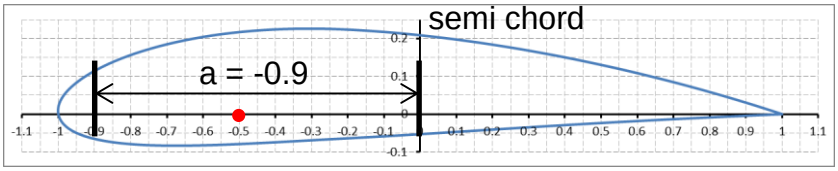

- AC is at ¼ chord (a=-0.5)

Figure 2.19 Definition of parameter a

A semi-empirical method was developed by ONERA (Office National d'Etudes et de Recherche Aerospatiales) in 1979 and lift coefficients were calculated through a set of differential equations developed from 1983 to 1990 [98-100]. This method was improved and extended by Petot [101] and Peters [102]. Bierbooms [103] compared this semi-empirical method with Theodorsen method and the results show that ONERA model gives better results but more computer time consuming.

Eq. (2.25) is developed based on a thin airfoil (flat plate) with small oscillations in incompressible flow. Many further studies have been carried out to extend or develop unsteady aerodynamics theories for more complex conditions and applications. Sun and Tang [104] use a computational fluid-dynamic analysis for their unsteady aerodynamics study of a model fly wing. Ho et al. [105] used an unsteady three-dimensional computational fluid dynamics model with an integrated distributed control algorithm for their flapping wing flyers study. Batina [106] introduced two different algorithms for the solution of the time-dependent Euler equations. One is based on Runge-Kutta integration method

and the other involves a modified Euler time-integration scheme [106]. Kreiselmaier and Laschka [107] developed a numerical based method unsteady Euler equation for an efficient and accurate unsteady load prediction in small disturbance conditions. The method can provide excellent and fast means for the prediction of unsteady forces.

2.4.2.2 Flutter

In dynamic aeroelasticity studies, flutter is one of the most characteristic and critical phenomena [108, 109]. Theodorsen developed a method to solve the flutter problem later named as K-method by introducing an artificial structure damping parameter g to basic dynamic motion equation Eq. (2.26) and rewrite in Eq. (2.27).

$$\left[-M\omega^2 + iD\omega + (1+ig)K - \left(\frac{1}{2}\rho V^2\right)Q(m,k)\right]\{u_h\} = 0 \qquad \textbf{(2.26)}$$

M	Mass matrix
ω	Circular frequency
D	Modal damping matrix
g	Artificial structural damping
Q	Aerodynamic force matrix
m	Mach number
$k = \frac{\omega b}{V}$	Reduced frequency
u_h	Modal amplitude vector

Eq. (2.26) can be written as

$$\left\{-\left[M + \frac{\rho}{2}\left(\frac{b}{2k}\right)^2 Q(m,k)\right]\frac{\omega^2}{1+ig} + D\frac{i\omega}{\sqrt{1+ig}} + K\right\}\{u_h\} = 0 \qquad \textbf{(2.27)}$$

Since flutter is a self-activated motion phenomenon, the right side of the Eq. (2.26) is zero due to no external force or moment. In Eq. (2.27), damping term D is multiplied with $\sqrt{1+ig}$ and the equation is valid only when flutter occurs

when $g = 0$. The flutter occurs only at the condition that a set values of Mach number (m), reduced frequency (k), and density (ρ) gives $g = 0$. Other solution which gives $g \neq 0$, are not valid and there is no physical meaning to the solution since g is an artificial damping. Crandall [110] stated the effect of damping in vibration theory. The K-method is a solution loop to get the finial valid condition $g = 0$ with various value of Mach number (m), reduced frequency (k), and density (ρ).

Following Theodorsen's research, many fluid-structure models were introduced. Kamakoti and Shyy [111] reviewed several robust fluid-structure coupled aeroelastic models with an efficient moving grid technique to account for structural deformations. Fully coupled model, loosely coupled model, and closely coupled model were reviewed along with aerodynamic solvers (governing equations for fluid equations, Navier-Stokes fluid flow solver, the geometric conservation law, and Turbulence modelling) and structure solvers (modal equations of motion and Newmark integration method). The interface procedure for fluid-structure solvers is also reviewed.

With the development of unsteady aerodynamic tools, flutter analysis has been applied to many research disciplines. Shubov [112] reviewed some research directions in simulation of flutter analysis. A collection of models of fluid-structure interaction were reviewed. The applications of these models cover topics of bending-torsion vibrations of coupled beams; flutter in transmission lines; flutter in rotating blades; flutter in hard disk drives; flutter in suspension bridges; and flutter of blood vessel walls. A review of unsteady transonic aerodynamics was carried out by Bendiksen [113] and the effort was focused on studying differences between nonlinear transonic aerodynamics and linear subsonic and supersonic aerodynamics from a theoretical and computational techniques point of view. Scanlan and Tomko [114] compared bridge flutter coefficients and airfoil flutter coefficient. An aeroelastic analysis of a full F-16

configuration under various flight conditions was processed by Geuzaine et al. [115].

Not only the studies on application on flutter analysis have continually been carried out, but also the flutter suppression and control has been another popular topic over the years. Active flutter suppression method was studied by Karpel [116] using state-space aeroelastic modelling. A comparison of State-Dependent Riccati Equation (SDRE) and Sliding Mode Control (SMC) approaches for flutter suppression was made by Elhami and Narab [117]. Passive suppressions of nonlinear panel flutter were studied by Moon and Kim [118, 119] using finite element method with active/passive hybrid piezoelectric actuators.

With the introduction of composite material and optimization methods, aeroelastic tailoring is now considered to be an important class of aeroelastic problems in aeronautical design. The historical background of aeroelastic tailoring and relative techniques is reviewed by Shirk et al. [120]. Guo [121] applied aeroelastic optimization to an aerobatic aircraft wing structure and results show that a considerable increase in flutter speed can be achieved with limited weight penalty. Genetic algorithm was introduced by Arizono and Isogai [122] to aeroelastic tailoring of a cranked-arrow wing to optimize flutter characteristics. Similar work was reported by Kameyama and Fukunaga [123] who also applied genetic algorithm in their aeroelastic tailoring work.

2.4.2.3 Gust

The difference between a gust analysis and a flutter analysis is that the external force term on the right side of Eq. (2.26) is no longer zero and Eq. (2.28) is the general form for gust analysis.

$$\left[-M\omega^2 + iD\omega + (1+ig)K - \left(\frac{1}{2}\rho V^2\right)Q(m,k)\right]\{u_h\} = \{P(\omega)\} \qquad \textbf{(2.28)}$$

Three conventional forms of gust velocity are known as ‘sharp-edged’ gust, ‘graded’ gust, and ‘1-cosine’ gust, see Figure 2.20.

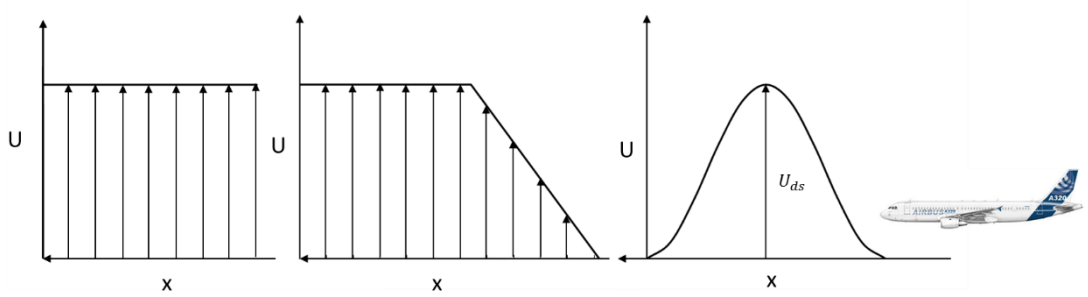

Sharp-edged Gust Graded Gust 1-Cosine Gust

Figure 2.20 Three conventional gust velocity forms

The ‘1-cosine’ gust form is the most popular form and the equation is given in Eq. (2.29).

$$u(t) = (U_{ds}/2)[1 - \cos(\pi t/T)] \quad \textbf{(2.29)}$$

u	Gust velocity
U	Design gust velocity
t	Time
T	Period

$$\mathrm{U}_{ds} = \mathrm{U}_{ref} \cdot \mathrm{F(g)} \cdot (H/350)^{\frac{1}{6}}$$

$$F(g) = 0.5 \cdot (F_{gz} + F_{gm}) \quad \textbf{(2.30)}$$

$$F_{gz} = 1 - (Z_{mo}/250000)$$

$$\mathrm{F}_{gm} = (R_2 \cdot \tan(\pi R_1/4))$$

U_{ref}	Reference gust speed
R_1	Maximum Landing Weight / Maximum Take-off Weight
R_2	Maximum Zero Fuel Weight / Maximum Take-off Weight
Z_{mo}	Maximum operating altitude

The fluid-structure models used for gust analysis are similar to those used for flutter analysis only the external load estimation is different. Wind forces acting on the structure is called gust factor G. The gust factor derivative method is

reviewed by Floris and De Iseppi [124]. Some other gust load calculation methods were introduced as follows.

1) The use of the envelope of the response process

2) The solution of the backward Kolmogorov equation

3) The use of some approximate formulae

Gust effects on different aircraft configurations have been studied by many investigators. Su and Cesnik [125] investigated the gust response of a highly flexible flying wing. Tang and Dowell [126] carried out gust analysis on a high-aspect-ratio wing and compared with experiments results.

Gust introduces extra load on wing structure leading to additional displacement of the aircraft. Gust alleviation devices are developed to reduce the effect of the gust and these devices can be divided into active and passive devices. Zhang et al. [127] applied active control surfaces for gust alleviation to a transonic wing and the results have shown that the root bending moment can be reduced by 60% to 80%. Active flow control technique applied by Xu et al. [128] can affect and suppress the fluid disturbances in order to alleviate gust load. The application of leading-edge separation control is investigated by Amitay et al. [129] for gust load alleviation. On the other hand, passive gust alleviation devices have been developed by many researchers. Sensburg et al. [130] applied both active and passive gust alleviation design to A300.

Optimization and aeroelastic tailoring can also help in gust alleviation. Vio and Cooper [131] performed optimization on a composite sensorcraft structure for gust alleviation.

2.5 Optimization in Composite Laminate Design

2.5.1 Optimization Method in Composite Material Design

Optimization methods can be categorized into four different classes: Gradient-Based Methods, Direct Search Methods, Specialized Algorithms, and hybrid methods. The classification of optimization methods are shown in Table 2.5.

Table 2.5 Classification of optimization methods [132]

Gradient-based methods	
• Vanishing the function's first gradient	• Quasi-Newton method
• Steepest descent	• Method of feasible directions
• Conjugate gradient	• Approximation schemes
Direct search methods	
• Partitioning methods	• Genetic algorithm
• Enumeration search	• Tabu search
• Simplex method	• Scatter search
• Random and greedy search	• Particle swarm
• Simulated annealing	• Ant colony
Special algorithm	
• Design with lamination parameters	• Discrete material optimization
• Layer-wise optimization	• Fractal branch-and-bound method
• Problem partitioning	• Knowledge-based methods

For Gradient-based methods, Sandhu [133] used vanishing the Function's First Gradient Method to find optimum fibre orientation for single layer laminate. Steepest descent was used for laminate sequence optimization alone or combined with other techniques [134, 135]. Davidon, Fletcher, and Powell [136] applied Quasi-Newton method for composite layup design and it became one of the most popular methods. Feasible direction method has been used within a combination with finite element method in composite laminate design [137, 138] and has been modified to overcome lost direction in highly non-linear constraints problems [139].

For Direct search methods, since Partitioning methods is limited by single design variable and Enumeration search should scan the whole design space for an optimum design these two design methods are not suitable for composite laminate optimization when a considerable design variables should be optimized. Simplex method is fast and accurate at a small number of design variables when the number becomes large it is less efficient than gradient based optimization methods [140]. Random and greedy search may not be able to find a better solution if a worse solution during the estimation is obtained. Genetic Algorithm has been applied widely in composite structure optimization with a variety of objective functions and constraints. It was developed to pick the fittest survivor within a considerable population. Genetic Algorithm is a global optimization technique which does not take a risk to end up with a local optimized solution. It is the most popular technique in optimizing the stacking sequence of a laminate component if the computational capability is not limited [141-144]. It has been applied for a variety of objective functions for laminate design and components design. The main problem for Genetic Algorithm is computational capability consumption and initial population selection.

Some special algorithms are applied to optimize a laminate with a comparatively small number of design variables. Design with Lamination Parameter Method reduces design variables by introducing the thickness of the laminate as a design variable instead of layup design variables. Layerwise Optimization Method optimizes the entire laminate by varying several layers' properties. Problem Partitioning Method splits the entire optimization into sub optimization problems by dividing design variables according to the nature of the design variables.

A hybrid method may take advantage of two or more optimization methods in order to achieve a better performance. Combinations of local optimization

methods with Genetic Algorithm are the most popular hybrid methods with a reasonable computation time and global optimization results [145, 146]. Local optimization methods can restart with several different initial design variables to obtain a global optimization result.

2.5.2 Optimization for Minimum Weight Design of Composite Structures

Gradient-based and direct search methods are two kinds of optimization methods widely used in variable stiffness composite structure optimal design for a minimum weight. The literatures related to minimum weight design with these two methods are reviewed in this section.

For gradient based method, Maksimenko et al. [147] applied a various search method combined gradient methods and a method of random search for a flat stiffened panel optimization to achieve a minimum weight. Ermolaev et al. [148] tried to use a modified gradient based method to optimize composite shells with taking natural frequencies as constraints. A gradient based method is applied for a minimum weight design of anisotropic fibre reinforced composites structure [149]. Guo et al. [150] applied a gradient based method for a composite wing minimum weight design with practical design consideration design variables were reduced and improved optimization efficiency. Though gradient based optimization may easy fall into local optimization results but many methods can be applied such as multi-level optimization and hybrid methods.

For direct search method, Nagendra et al. [151] applied a genetic algorithm in optimization of a blade stiffened composite panel and Kang and Kim [152] applied a genetic algorithm in optimization of a minimum weight subject post buckling. Direct search method was applied for aeroelastic tailoring of a composite wing with multi design constraints [153]. Hu [154] use Tabu search

method with random moves for composite genetic algorithm optimization and achieve a 26.14% reduction in weight. Direct search method provides global optimal design results but would take considerable computer time.

In this optimization literature review section, three categorizes of optimization methods are reviewed. Most commonly used optimization methods in minimum weight design are the gradient based methods and direct search methods. Both methods have been applied on many minimum weight optimizations and have been approved to be able to reduce considerable weight. In this research a gradient based optimization method is applied in minimum weight design with multi design constraints.

3 Optimal Structure Type Determination Subject to Buckling

An appropriate stiffened panel type should be determined before any further optimal minimum weight panel design against buckling can be carried out. Generally, the determination of a structure type for a specific component under a given loading condition is based on experience and former design practise. In this chapter, investigation of structure efficiency subject to resist instability under a given loading range was carried out within three structure types: stinger stiffened panel, sandwich panel, and grid structure. The buckling efficiency used in this chapter is a ratio of distributed load to structure mass. These structure types are widely used in aviation industry for different components under different loading conditions. The investigation is to evaluate and compare the efficiency of optimal design of these structure types in the load range of a commercial civil aircraft wing with morphing high lift device [155, 156]. The evaluation was carried out on panels which represent upper surfaces of the wing box of the aircraft stiffened with one of the three structure types. Theoretical method, finite strip method, and finite element method were used to obtain the evaluation results.

3.1 Topology of a Flat Panel under In-Plane Distributed Loading

Topology analysis was introduced in this section to show the main loading path of a flat panel under a specific loading condition and the variation of the main loading path according to the loading condition. The result of the topology study was used to show the potential of structure types in resisting buckling under a specific loading condition. The topology analysis was carried out through commercial FE package Patran/Nastran. A metallic panel of dimension 600x1200 mm as shown in Figure 3.1 was used in this topology optimization.

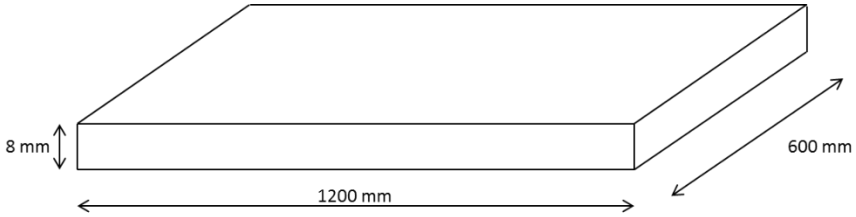

Figure 3.1 Geometry of topology plate

In Patran/Nastran, the panel was modelled with shell elements the material properties used for this panel are listed in the following Table 3.1.

Table 3.1 Material properties for topology optimization

E (N/mm^2)	7.20E+04	Poisson's Ratio	0.3	G (N/mm^2)	2.77E+04

Two load types, axial distributed compression load and shear distributed load, were applied onto the structure separately or in a combination. The two loading types are illustrated in Figure 3.2 and three load cases are shown in Figure 3.3.

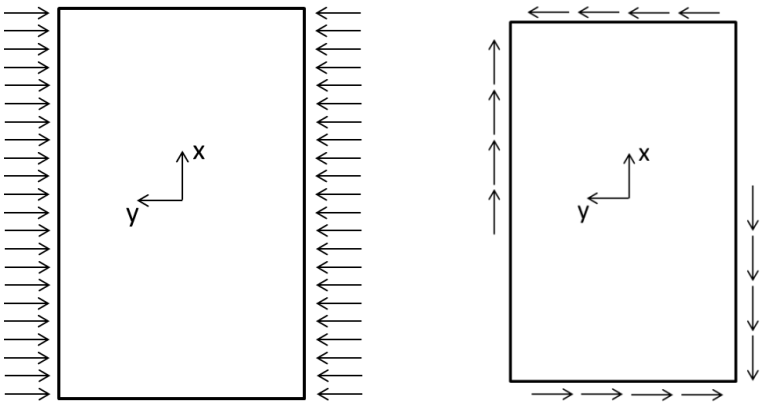

Axial compression load Shear Load

Figure 3.2 Axial compression load and shear load

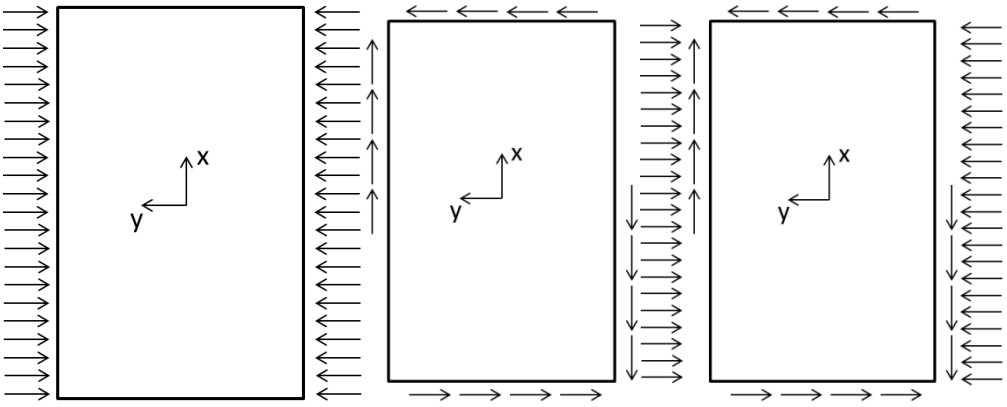

Figure 3.3 Three load case studies

The four corners were constrained in z direction and at the middle of every edge were constrained in the parallel direction. At the centre of the plate a full constrained was applied. The boundary condition is illustrated in Figure 3.4.

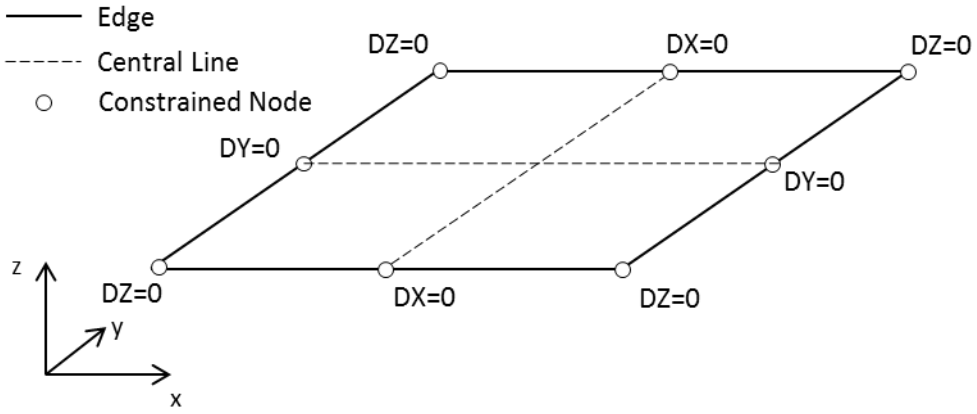

Figure 3.4 Boundary condition of topology analysis

Unit distributed loads were applied on the edges according to the load cases. The topology criteria were to remove minimum stress materials to achieve a minimum weight of the panel.

The topology analysis results are given in Figure 3.5. From Figure 3.5 a), the result shows under axial compression load, the load path parallel with the

loading direction this indicates that stiffeners should be arranged in parallel with the load to efficiently resisting deformation. The load-paths in Figure 3.5 b) and c) show that shear load drives load-path away from axial compression load direction with a specific angle and in a pure shear load condition the angle between load-path and axis is 45˚. Grid Structure is a reasonable structure type in this load condition. The results also indicated that a proper selection on structure type based on loading condition is really important to achieve an optimal design of a stiffen panel.

a) Axial Load

b) Shear Load

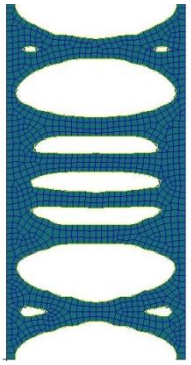

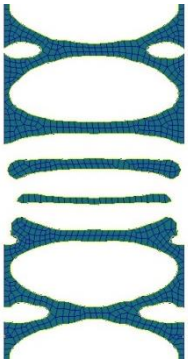

30% materials removed

60% materials removed

40% materials removed

c) Combined Load (30% Shear Load)

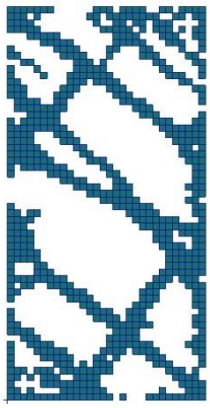

40% materials removed

Figure 3.5 Topology analysis results for three cases

Based on this topology analysis results, three structure types were taken into consideration in the buckling efficiency comparison in this chapter and they are metallic blade stringer stiffened panel, metallic cross stiffener grid structure, and composite sandwich panels. The blade stringer stiffened panel and metallic cross grid structure were chosen for the main load path results given in Figure 3.5 a) and c). The following sections firstly calculated optimal design for each stiffened structure type under distributed compression load subject to buckling and compared the efficiencies of the optimal design of these structure types and then evaluated efficiencies under combined loading conditions. Patran/Nastran FE package and ESDU finite-strip method packages were applied for these analyses.

3.2 Optimal Design of Three Structure Types Subject to Buckling under Axial Compression Loading

In this section, optimal design for each structure type was firstly calculated through corresponding methods respectively. At the end of this section, the efficiencies of the three structure types are plotted against distributed load N_x in the same chart used for comparison. The optimal design was carried out on the same panel given in Figure 3.6. Stringers were laid in y direction parallel to the distributed load direction. The distributed load (N_x) varies from 100 N/mm to 3000 N/mm covering a practical load range of the wing with morphing high lift devices of a 200 seats commercial aircraft [156].

3.2.1 Optimal Design of Stringer Stiffened Panel Subject to Buckling

The objective of this section is to obtain optimal blade stringer stiffened panels within a practical load range and plot their buckling efficiencies against applied distributed load. Emero's optimal design method [27] for stringer stiffened panel was applied in this section to obtain the optimal design. As stated in the

literature review, the method is an analytical one and it gives a set of design parameter ratios to determine cross-section dimensions for an optimal design of a stringer stiffened panel under a given distributed axial load and letting global and local buckling take place at the same time. Case studies were carried out and results given in Chapter 4 to ensure Emero's method provides an optimal design of panels stiffened with several stringer types and in this section the method is applied directly in blade stringer stiffened panel design.

Optimal design of blade stringer stiffened panel was carried out using the dimensions given in Figure 3.6 and the distributed compression load varied from 200 N/mm to 3000 N/mm with an increment of 200 N/mm at each step applied in y axis direction on edges parallel to x axis. The material properties for the design are given in Table 3.1. The optimal design ratios were picked from Emero's design table given in Table 2.2 as 0.65 for web height to stringer pitch and 2.25 for web thickness to skin thickness.

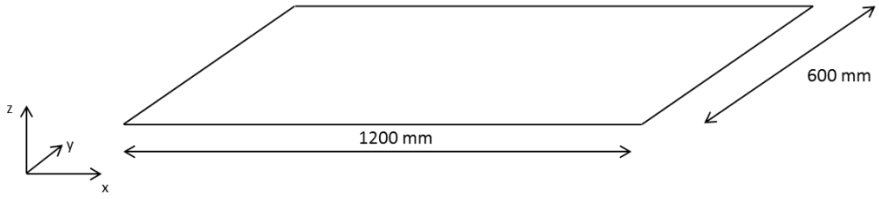

Figure 3.6 Basic geometry of the plate

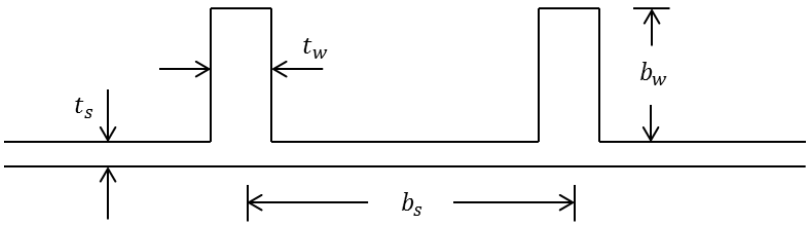

Figure 3.7 Definition of blade stiffened panel

The definition of geometry dimensions of the panel section are given in Figure 3.7 and the optimal designed results were calculated using Eq. (2.11) to Eq. (2.13) and results are listed in Table 3.2

Table 3.2 Optimal design results for blade stringer stiffened panel

N_x (N/mm)	t_s (mm)	b_s (mm)	b_w (mm)	t_w (mm)	Mass (kg)	N_x/Mass (kg)
3000	2.51	72.85	47.35	5.64	12.23	245.31
2800	2.42	71.61	46.54	5.45	11.69	239.45
2600	2.33	70.29	45.69	5.25	11.53	225.44
2400	2.24	68.90	44.78	5.05	10.95	219.23
2200	2.15	67.42	43.82	4.83	10.35	212.65
2000	2.05	65.83	42.79	4.61	10.04	199.11
1800	1.94	64.12	41.68	4.37	9.38	191.90
1600	1.83	62.26	40.47	4.12	8.96	178.57
1500	1.77	61.26	39.82	3.99	8.59	174.58
1400	1.71	60.21	39.14	3.85	8.22	170.41
1200	1.59	57.94	37.66	3.57	7.65	156.81
1000	1.45	55.36	35.98	3.26	6.99	143.06
800	1.29	52.35	34.03	2.91	6.21	128.83
600	1.12	48.72	31.67	2.52	5.41	110.81
400	0.92	44.02	28.62	2.06	4.45	89.83
200	0.65	37.02	24.06	1.46	3.13	63.86

The buckling stress of the geometry set at distributed load of 1500 N/mm shown in Table 3.2 was checked with ESDU package 0980016 [157] and FE package Patran/Nastran and a comparison of the results are given in Table 3.3. Taking the Patran/Nastran as the baseline, the error of Emero's method was 6.98% within an acceptable range and the comparison shows the results in Table 3.2 are reliable. FE model is illustrated in Figure 3.8 and boundary conditions for the FE stiffened panels in this chapter were obtained from analytical solution assumptions based on distributed moment method [38] and illustrated in Figure 3.9 with loaded edges simply supported and constrain all rotation degree of freedom, shear displacement constraints are applied at the middle of the edges.

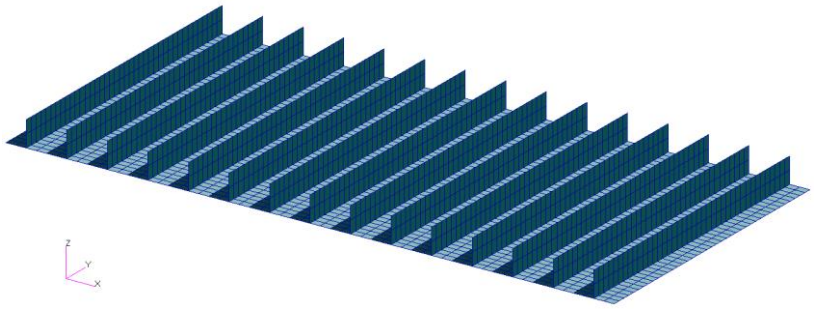

Figure 3.8 FE shell model for blade stringer stiffened panel

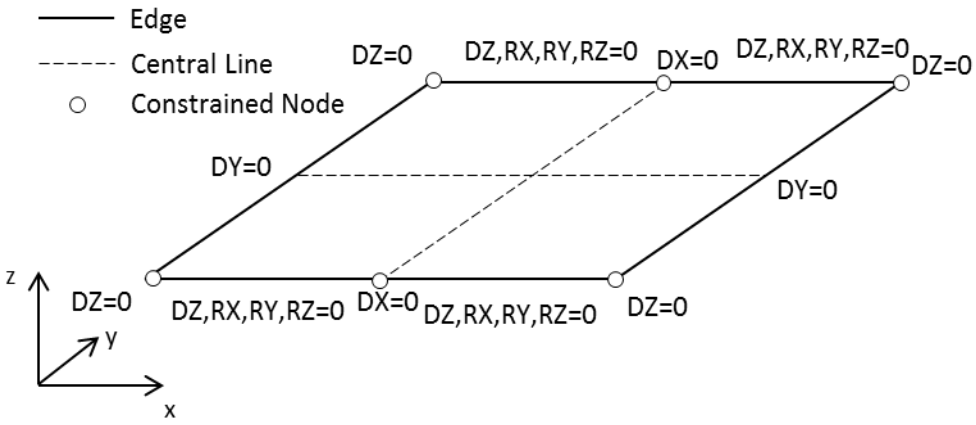

Figure 3.9 Boundary conditions for FE models

Table 3.3 Buckling stress comparison between different tools

N_x N/mm	Emero's Method N/mm^2	ESDU N/mm^2	Patran/Nastran N/mm^2
1500	344.3	346.8	322.3

The efficiencies of optimal designed panels against distributed buckling load are plotted in Figure 3.10. From Figure 3.10, it shows the efficiencies increase along with the distributed load. The efficiency curve is not smooth due to integer number of stringers should be fitted into a fixed width panel result in the pitch b_s is not perfectly match with the value given by optimal design method. This efficiency curve was compared with efficiency curves of optimal design of grid structure and sandwich panel in the later section within the same load range.

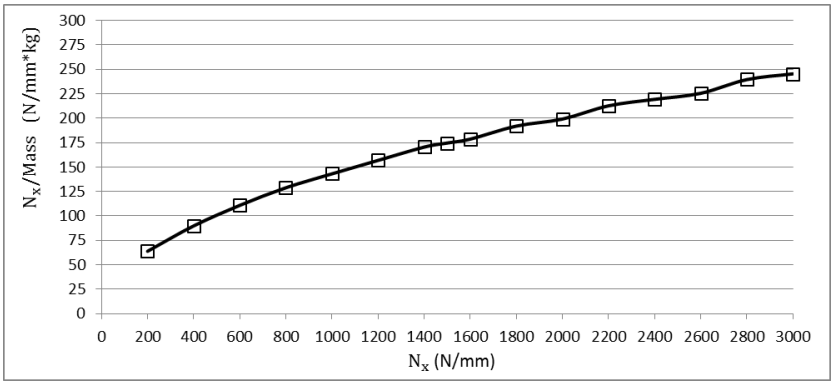

Figure 3.10 Efficiency of blade stringer stiffened panel

3.2.2 Optimal Design of Sandwich Panel Subject to Buckling and Winkling

This section is to calculate efficiency curve of optimal design of composite sandwich panels under distributed axial compression load within the load range. To achieve an optimal design of composite sandwich panel subject to buckling and wrinkling, parametric study on three design parameters as skin thickness, orientation layup of laminate, and the core height, were taken into consideration. Parametric studies on these design parameters were carried out and some key conclusions were drawn for optimal sandwich panel design. Parametric study was initially started from sensitivity studies of laminate ply orientation. The effect of skin thickness and core height were studied in the second stage. ESDU 88015 [158] and ESDU 80147 [159] were introduced as numerical tools to evaluate wrinkling and buckling stresses respectively. All the cases studied in this section were based on the panel geometry given in Figure 3.6.

With practical design concern, only two different ply layups, $[0^\circ/90^\circ]$ and $[45^\circ/-45^\circ]$ were used in this layup study and symmetric layups were applied. The composite material ply properties are given in Table 3.4.

Table 3.4 Composite ply properties

	E_x N/mm^2	E_y N/mm^2	G_{12} N/mm^2	V_{12}	ρ kg/mm^3	t_{ply} mm
IM7/8552	1.64E+05	1.00E+04	5.00E+03	0.3	1.58e-6	1.25E-01
airexR63	56	56	21	0.3	9e-9	

3.2.2.1 Parametric Study on Ply Orientations

Two different layup laminates with a skin thickness of 1mm were used in this parametric study as $[90^{\circ}/0^{\circ}/90^{\circ}/0^{\circ}]_s$ and $[45^{\circ}/-45^{\circ}/45^{\circ}/-45^{\circ}]_s$. The corresponding laminate properties are given in Table 3.5.

Table 3.5 Laminates' properties

	E_x MPa	E_y MPa	G_{12} MPa	V_{12}	t_s mm	Ply No.
[90˚/0˚/90˚/0˚]s	8.74E+04	8.74E+04	5.00E+03	3.45E-02	1mm	8
[45˚/-45˚/45˚/-45˚]s	1.80E+04	1.80E+04	4.22E+04	8.00E-01	1mm	8

The core was made of paper foam (airexR63) the properties are given in Table 3.4 and core height of the sandwich panel varied from 5.0mm to 40mm which is in the core height range recommended by Niu [40].

Table 3.6 Results for two layup parametric study

Layup	Core Height	Buckling Load	Layup	Core Height	Buckling Load
	mm	N/mm		mm	N/mm
[90/0/90/0]s	5	68.9	[45/-45/45/-45]s	5	60.4
	10	164		10	148
	20	375		20	352
	30	591		30	570
	40	807		40	792

ESDU package 80147 [159] for sandwich panel buckling distributed load calculation was introduced and buckling load results of sandwich structures made of two different layup laminates are given in Table 3.6 and plotted in Figure 3.11. All edges of the sandwich panel were simply supported.

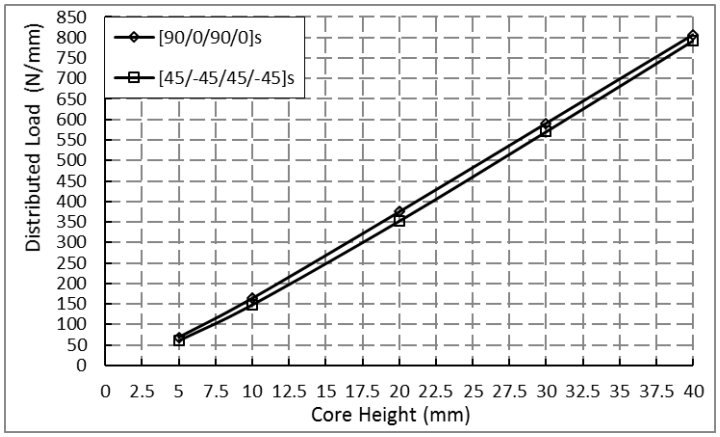

Figure 3.11 Parametric study of 0˚-90˚ laminate and ±45˚ laminate

From Table 3.6 and Figure 3.11, the results show that buckling loads of sandwich panels with face laminate stacking with $[0^{\circ}/90^{\circ}]$ layups are higher than the buckling loads of sandwich panels whose surface laminate stacked with $[45^{\circ}/-45^{\circ}]$ plies at the same core height under axial compression load. This is due to the in-plane bending stiffness of $[0^{\circ}/90^{\circ}]$ layups are higher than $[45^{\circ}/-45^{\circ}]$ layups. The $[0^{\circ}/90^{\circ}]$ layup laminate was used for sandwich panel surfaces in the following optimal design.

3.2.2.2 Parametric Study on Sandwich Panel Skin Thickness and Core Height Effect

Parametric study on skin thickness t_s and core height t_c with $[0^{\circ}/90^{\circ}]$ layup laminate was carried out and core height various from 5.0 mm to 40 mm as suggested [28]. At each core height case, skin thickness varied from 0.5 mm to 2.0 mm. In this Section ESDU 88015 [158] and ESDU 80147 [159] were used for buckling load and wrinkling load estimation respectively. The results are listed in Table 3.7 and plotted in Figure 3.12.

Table 3.7 Parametric study on skin thickness and core height

Layup	t_s	t_c	Mass	Buckling Load	Symmetric Wrinkling Load	Anti-symmetric Wrinkling Load	N_x/Mass
	mm	mm	kg	N/mm	N/mm	N/mm	N/mm*kg
[0/90]	0.25	5	1.03	27.1	132	Overall	26.32
	0.25	10	1.49	83.6	94.3	136	56.09
	0.25	20	2.41	240	67.1	111	27.82
	0.25	30	3.33	425	54.9	92.3	16.47
	0.25	40	4.26	625	47.6	80.6	11.19
$[0/90]_s$	0.5	5	1.60	45	704	Overall	28.15
	0.5	10	2.06	123	510	Overall	59.73
	0.5	20	2.98	314	365	400	105.34
	0.5	30	3.90	524	299	413	76.62
	0.5	40	4.82	742	260	390	53.90
$[90/0/90/0]_s$	1	5	2.74	68.9	1220	Overall	25.18
	1	10	3.20	164	902	Overall	51.30
	1	20	4.12	375	653	Overall	91.05
	1	30	5.04	591	537	598	106.55
	1	40	5.96	807	467	619	78.33
$[0/90/0/90/0/90]_s$	1.5	5	3.87	83.2	2890	Overall	21.48
	1.5	10	4.33	184	2170	Overall	42.45
	1.5	20	5.26	397	1590	Overall	75.53
	1.5	30	6.18	612	1310	Overall	99.07
	1.5	40	7.10	831	1140	Overall	117.06
$[0/90/0/90/0/90/0/90]_s$	2	5	5.01	92.3	4190	Overall	18.42
	2	10	5.47	195	3200	Overall	35.64
	2	20	6.39	408	2370	Overall	63.81
	2	30	7.32	626	1960	Overall	85.58
	2	40	8.24	841	1710	Overall	102.10

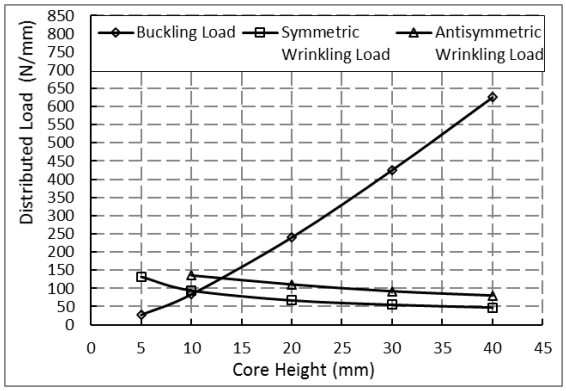

a) 0.25mm thickness skin

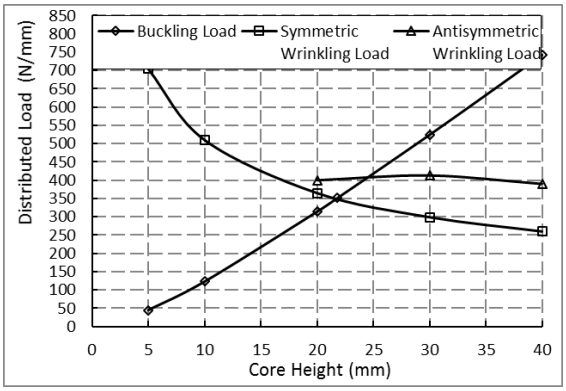

b) 0.5mm thickness skin

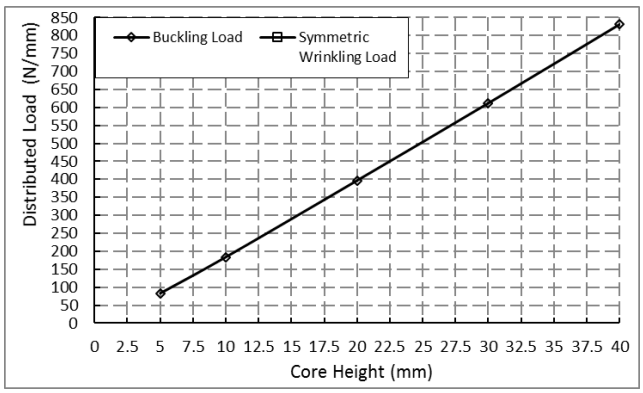

c) 1.5 mm thickness skin

Figure 3.12 Buckling loads of parametric studies of t_s and t_c

The most important observation from Figure 3.12 is that buckling loads of sandwich panels are sensitive to core height that the buckling load increases along with the increment of core height. A second observation is that with the increase of core height, the critical wrinkling load decreases and an intersection point of wrinkling load curve and buckling load curve at a specific core height for a constant skin thickness can be found. The distributed load at the intersection point increases with the skin thickness. A third observation is that within the study ranges of core height and skin thickness anti-symmetric wrinkling is comparatively less critical than symmetric wrinkling and buckling. Figure 3.12 c) indicates that above 1.5mm skin thickness, buckling is the main concern with in the practical core height range.

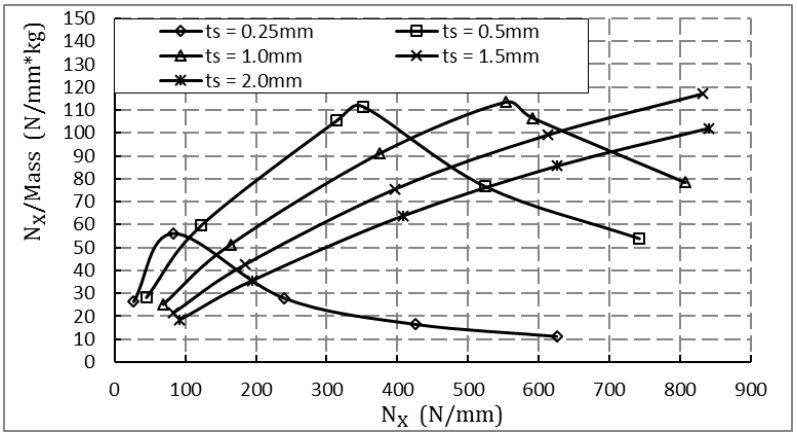

Figure 3.13 Structure efficiency against distributed load N_x

Figure 3.13 displays the buckling efficiency against distributed load. For a constant skin thickness, maximum efficiency can be achieved at the core height when buckling and wrinkling take place at the same time. Figure 3.13 also displays the trend for efficiency against distributed load with the increase of skin thickness that within a lower load range below 350 N/mm the buckling efficiency increases rapidly with distributed load and from 350 N/mm to 850N/mm within a skin thickness from 0.5mm from 1.5mm the maximum buckling efficiency is even and then drops with the increase of skin thickness. The efficiencies of optimal design of sandwich panels with optimal design values of core heights and skin thicknesses are given in Figure 3.14. The buckling efficiency of sandwich panel is limited to the core height and core stiffness in the high load range.

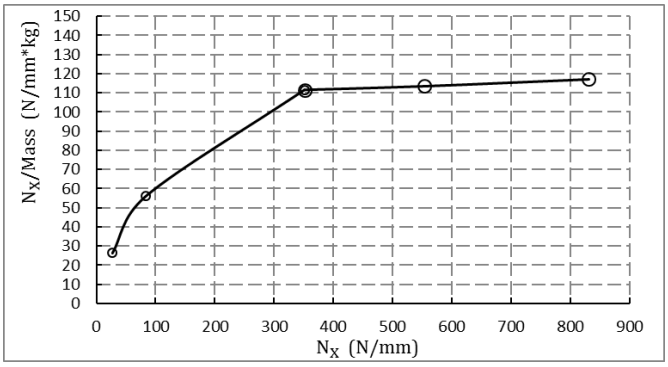

Figure 3.14 Efficiencies of optimal design of sandwich panels

3.2.3 Optimal Design of Grid Structure Subject to Buckling

Optimal design of grid structures were carried out in this section and the efficiencies are plotted at the end of this section. Commercial FE package Patran/Nastran is used in this section for buckling load calculation. Metallic grid structure used in this section for optimal design is a panel stiffened with blade stiffener in 0˚ and 90˚ as shown in Figure 3.15 and axial compression load is applied in the y direction along with 0˚ stringer. Optimal design considering different direction stiffener angle is not discussed here. The optimal design for the grid structure started from the Emero's optimal stringer stiffened panel design method results and transverse stiffeners were given in the same geometry dimensions.

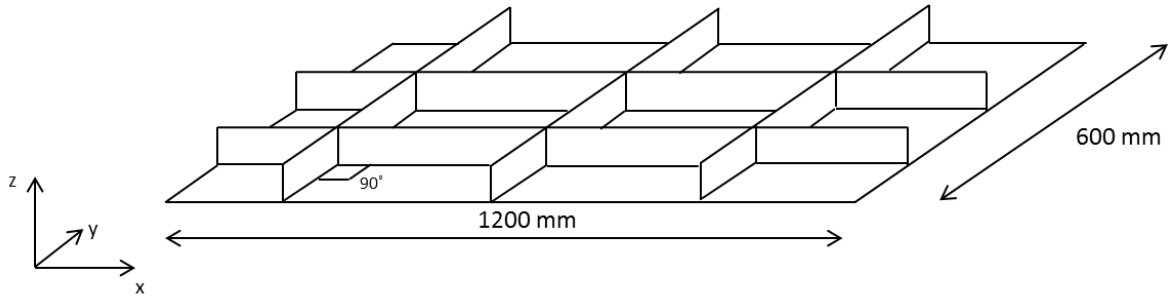

Figure 3.15 0˚ and 90˚ cross grid section

The optimal design equation and ratios of Emero's method is given in Table 3.8.

Table 3.8 Emero's optimal design equations and ratios of AGS [27]

Stringer Type	**Optimums Values**	**Dimensionless Geometric Expressions**
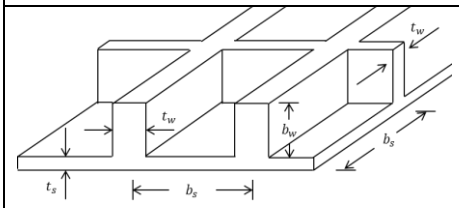 0˚-90˚ Unflanged Grid	$\epsilon_{max} = 0.656$ $r_{bw} = 0.65$ $r_{tw} = 2.25$	$\alpha = 1 + r_{bw} r_{tw}$ $\beta = .5\, r_{bw}^2 r_{tw}$ $\gamma = .333\, r_{bw}^3 r_{tw}$

Verification was carried out based on this method with Patran/Nastran. The verification model was obtained through Emero's optimal design method with a distributed load of 1400 N/mm and the design results are given in Table 3.9.

Table 3.9 Emero's grid structure optimal design results (1400 N/mm)

Distributed Load	**Design Dimensions**			
N_x (N/mm)	t_w mm	t_s mm	b_w mm	b_s mm
1400	3.85	1.71	39	60

The FE model was set up by the design results given in Table 3.9 with shell elements and corresponding edge pressure representing distributed load was applied to the edges parallel to x axis in the y direction in Figure 3.15. The boundary conditions are given in Figure 3.9. The all edges were simply supported and all rotational degrees of freedom on loaded edges were constrained. Linear buckling analysis was applied and the buckling load factor result to the analysis was 1.09. The first buckling mode shape is shown in Figure 3.16.

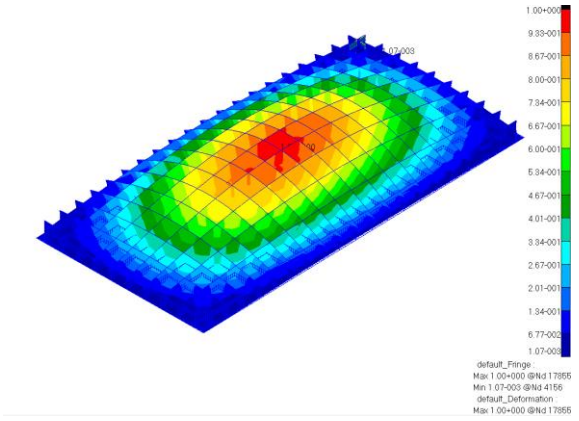

Figure 3.16 Global buckling mode of verification grid model

This analysis shows that the estimation of buckling stress based on Emero's method is 10% lower than the results given by FE method with the same geometry which means the method is comparatively conservative. The second

buckling mode shape is given in Figure 3.17 with a buckling load factor of 1.24 which is 13.8% higher than that of global buckling load factor (first buckling mode). The global buckling and local buckling load factors were close to each other.

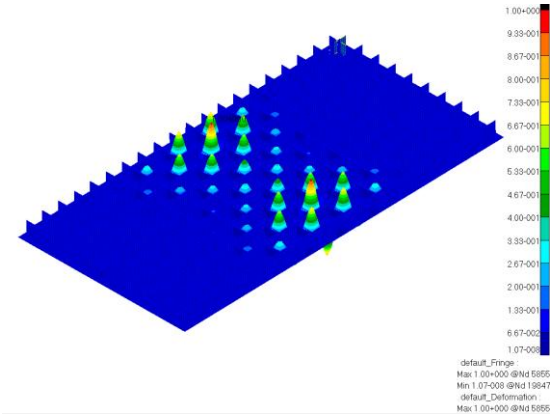

Figure 3.17 Local buckling mode of verification grid model

The reason for the local buckling load factor is 24% higher than estimation is that the local buckling coefficient for Emero's method was calculated neglecting transverse stiffener stiffness. Considering the 13.8% difference between local and global buckling load, the Emero's method provides an optimal cross grid structure design. Emero's method was further applied to more distributed load cases to obtain the buckling efficiencies of optimal design. The optimal design results are listed in Table 3.10 and plotted in Figure 3.18.

Table 3.10 Optimal design results of grid structure under axial compression

Distributed Load	**Design Dimensions**				**Mass**	**Efficiency**
N_x (N/mm)	t_w mm	t_s mm	b_w mm	b_s mm	M kg	$N_x/Mass$ N/mm*kg
950	3.17	1.41	35.45	54.55	10.76	88.26
1400	3.85	1.71	39.00	60.00	13.07	107.14
2150	4.78	2.12	43.33	66.67	16.19	132.77
3500	6.09	2.71	48.75	75.00	20.66	169.40

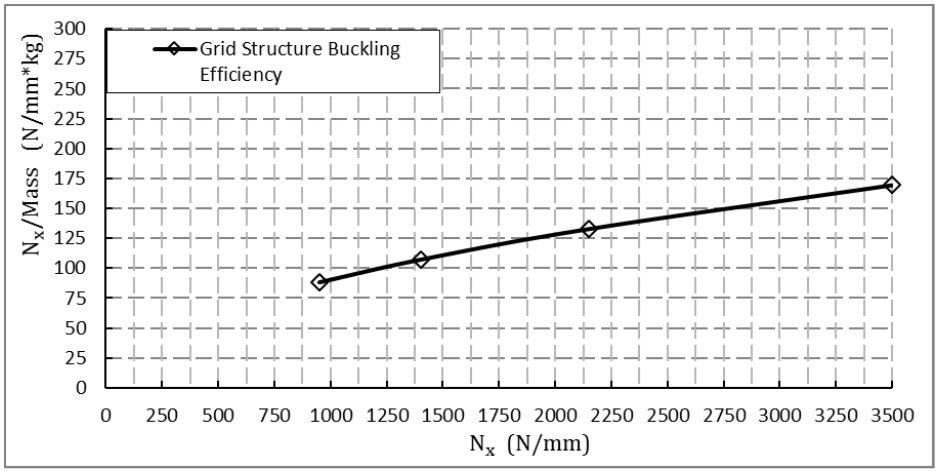

Figure 3.18 Efficiency of grid structure

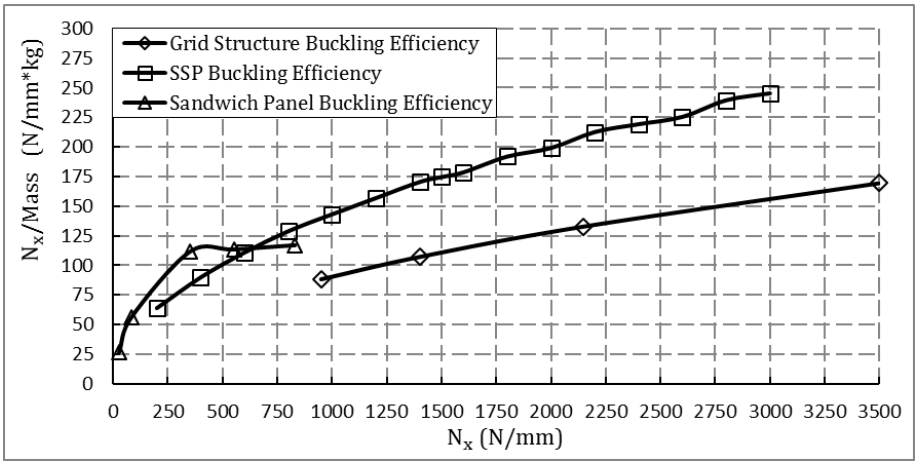

Figure 3.19 Efficiency of three structure types

The efficiencies of three structure types are shown in Figure 3.19. The figure shows that under uniaxial compression load, in the low distributed load range, below 750N/mm, sandwich panel is the most efficient structure type against buckling. When the compression load above 750N/mm, stringer stiffened panel becomes more efficient, this is because sandwich panels are limited by the core height limit, core stiffness, and wrinkling. Under compression load, the buckling efficiency of a grid structure is lower than other structure types in the whole load range.

3.3 Efficiency of Three Structure Types under Combined Loading

One of the practical load conditions is a combination of uniaxial distributed load and shear load and this load condition was considered in this buckling efficiency comparison. In this section, several load combination of axial compression and shear load were applied to the optimal structure models used in the early sections and the efficiency chart was re-plotted to illustrate the shear load effect on buckling efficiencies of three structure types. Patran/Nastran was used for elastic buckling analysis (no plasticity was considered) of stringer stiffened panel and grid structure models in this section. ESDU packages [158, 159] were used for buckling and wrinkling load analysis for sandwich panels.

The FE models for stringer stiffened panel and grid structure used in uniaxial buckling analysis were used in this analysis with shear distributed force applied on edges parallel to y axis in Figure 3.20. Four optimal design results at 950 N/mm, 1400 N/mm, 2150 N/mm, and 3500 N/mm were selected in this study. A shear load ratio was introduced to determine the shear force applied to the models. The shear load ratio varied from 10% to 30% which means the total shear force changed from 10% to 30% of the total compression force applied on edges parallel with X axis. The application of a combination load is illustrated in Figure 3.3 and the boundary condition is illustrated in Figure 3.20. Loaded Edges were constrained in displacement in Z direction and all rotational degrees of freedom and side edges were constrained in Z direction displacement. Four corner nodes were constrained in y direction.

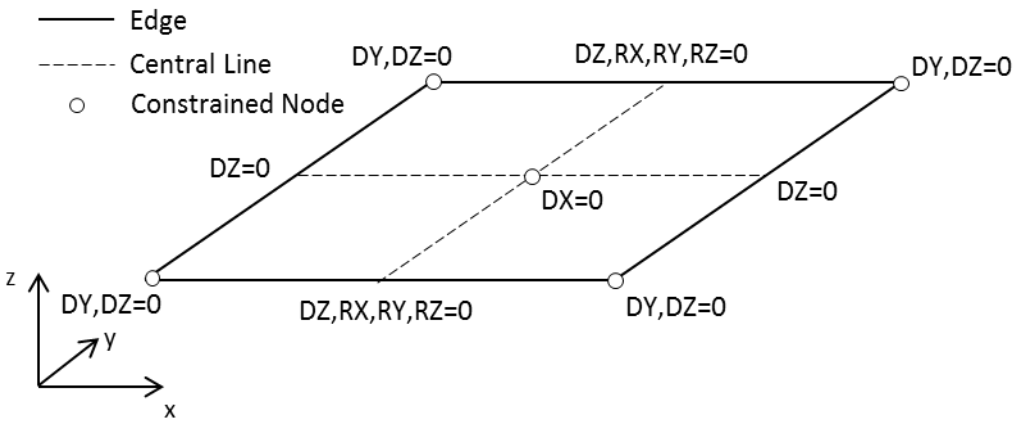

Figure 3.20 The boundary condition of a combination load case

An example of the loading and boundary condition of FE model is given in Figure 3.21. Red arrows represent compression distributed forces' directions and yellow arrows represent shear distributed forces' directions.

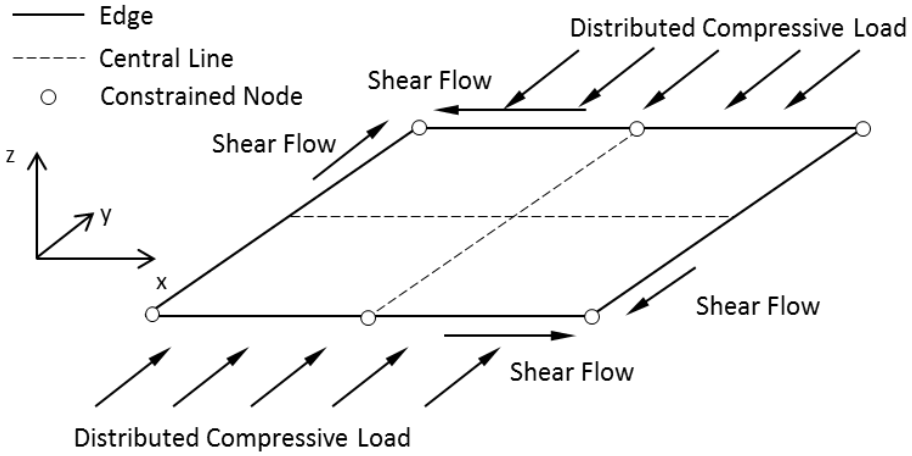

Figure 3.21 Load and boundary condition of FE model

The buckling analysis for stringer stiffened panel and grid structure under a combined load condition were at distributed compression load of 950 N/mm and 95 N/mm shear load (shear load ratio 10%). FE results are given in Figure 3.22 and Figure 3.23 buckling load from Nastran results are 836 N/mm (0.88) and 1012.7 N/mm (1.06) respectively. The buckling load factors are in the brackets. All the buckling results for combine load cases are listed in Table 3.11.

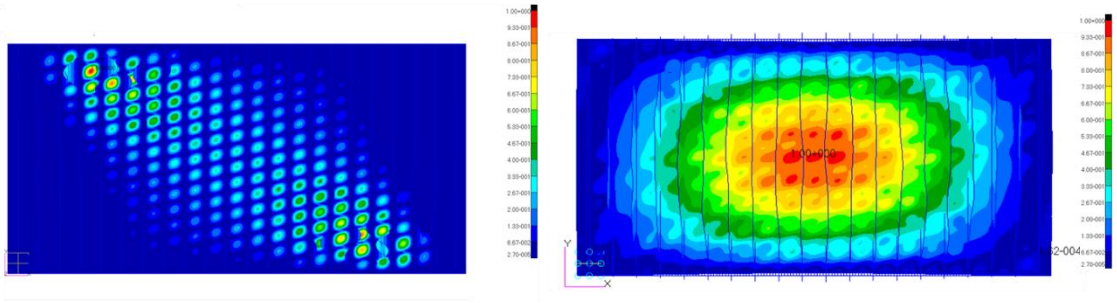

Local Buckling Mode (0.88) Global Buckling Mode (1.025)

Figure 3.22 Combined load buckling analysis results of stringer stiffened panel

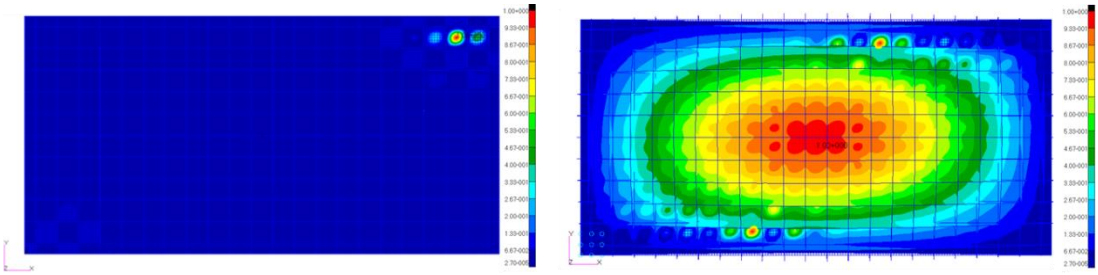

Local Buckling Mode (1.06) Global Buckling Mode (1.18)

Figure 3.23 Combined load buckling analysis results of grid structure

Table 3.11 Buckling efficiencies of stringer stiffened panel under combined loads

Stringer Stiffened Panels					
Shear Load Ratio	**Compression Load for Design N/mm**	**Shear Load Applied N/mm**	**Buckling Load N/mm**	**Mass kg**	**N_x/Mass N/mm*kg**
10%	950	95	776.65	6.75	115.00
	1400	140	1150.13	8.20	140.29
	2150	215	1835.58	10.16	180.68
	3500	350	3047.56	12.96	235.11
20%	950	190	619.1435	6.75	91.68
	1400	280	931.028	8.20	113.57
	2150	430	1516.8465	10.16	149.30
	3500	700	2591.47	12.96	199.92
30%	950	285	508.098	6.75	75.24
	1400	420	795.13	8.20	96.99
	2150	645	1269.274	10.16	124.93
	3500	1050	2192.68	12.96	169.16

Table 3.12 Buckling efficiencies of grid structures under combined loads

Grid Structures					
Shear Load Ratio	**Compression Load for Design N/mm**	**Shear Load Applied N/mm**	**Buckling Load N/mm**	**Mass kg**	**N_x/Mass N/mm*kg**
10%	950	95	1109.89	10.76	103.11
	1400	140	1678.18	13.07	128.43
	2150	215	2625.80	16.19	162.15
	3500	350	4171.65	20.66	201.91
20%	950	190	1062.29	10.76	98.69
	1400	280	1548.54	13.07	118.51
	2150	430	2441.755	16.19	150.79
	3500	700	4028.15	20.66	194.96
30%	950	285	949.99259	10.76	88.26
	1400	420	1388.912	13.07	106.29
	2150	645	2198.805	16.19	135.78
	3500	1050	3643.15	20.66	176.33

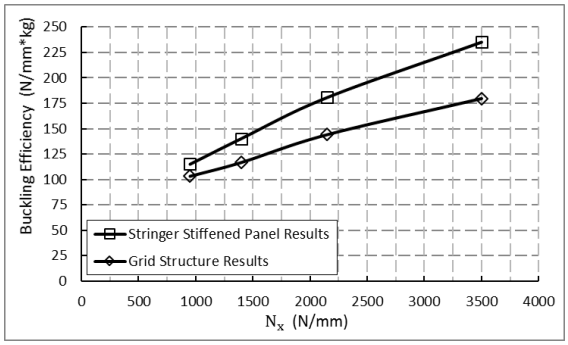

a) Combined Load (10% Shear Load)

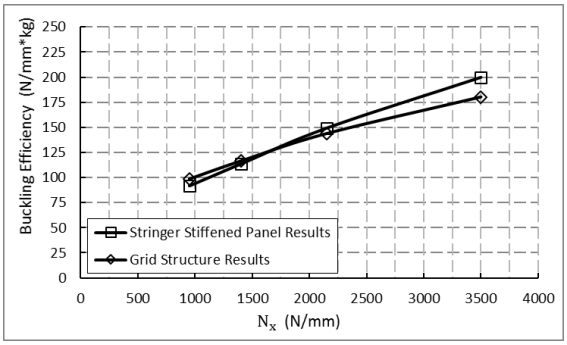

b) Combined Load (20% Shear Load)

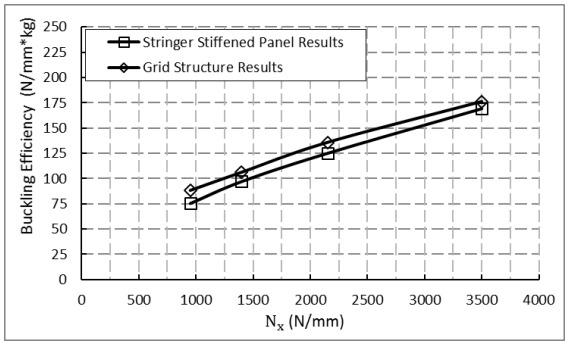

c) Combined Load (30% Shear Load)

Figure 3.24 Buckling efficiency comparison of stringer stiffened panel and grid structures

Table 3.13 Buckling efficiencies of sandwich panels under combined loads

Shear Ratio	t_s	t_c	Mass	Buckling Load	N_x/Mass	Shear Ratio	t_s	t_c	Mass	Buckling Load	N_x/Mass
	mm	Mm	kg	N/mm	N/mm*kg		mm	mm	kg	N/mm	N/mm*kg
10%	0.25	5	1.03	26.9	26.13	20%	0.25	5	1.03	26.8	26.03
	0.25	10	1.49	83.3	55.89		0.25	10	1.49	82.5	55.35
	0.5	21.8	3.15	348	110.59		0.5	21.8	3.15	341	108.37
	1	28.2	4.87	549	112.64		1	28.2	4.87	534	109.56
	1.5	40	7.10	824	116.07		1.5	40	7.10	806	113.53
	2	40	8.24	839	101.86		2	40	8.24	809	98.22
30%	0.25	5	1.03	26.5	25.74						
	0.25	10	1.49	81.1	54.41						
	0.5	21.8	3.15	330	104.87						
	1	28.2	4.87	511	104.84						
	1.5	40	7.10	769	108.32						
	2	40	8.24	777	94.33						

The buckling stresses of optimal sandwich panels under combined load are given in Table 3.13 calculated through ESDU 81047 [159] at three different shear load ratio and by comparing the results in Table 3.7 and Table 3.13, it shows that the shear load do not have a significant influence on the capability of sandwich panels in resisting buckling.

From Figure 3.24, the results show that with the increase of the shear load ratio, buckling efficiencies of stringer stiffened panel and grid structures both decrease. The local buckling of stinger stiffened panels are comparatively more sensitive to shear load than that of grid structures and their capability of resisting buckling rapidly reduce and with the shear load ratio more than 20% the grid structures become more efficient than stringer stiffened panels with the same stiffener dimensions with the stringer stiffened panel starting from the low load range. From the observation of the buckling modes in FE analysis results, under a combined load condition stringer stiffened panel tended to fall into local

buckling and the global/local buckling modes were still close for grid structures. It can be concluded that under a shear load ratio around 30%, sandwich panel is still the most efficient structure type in the low load range (0-800 N/mm) and grid structure is the optimal structure type in the rest of the load range.

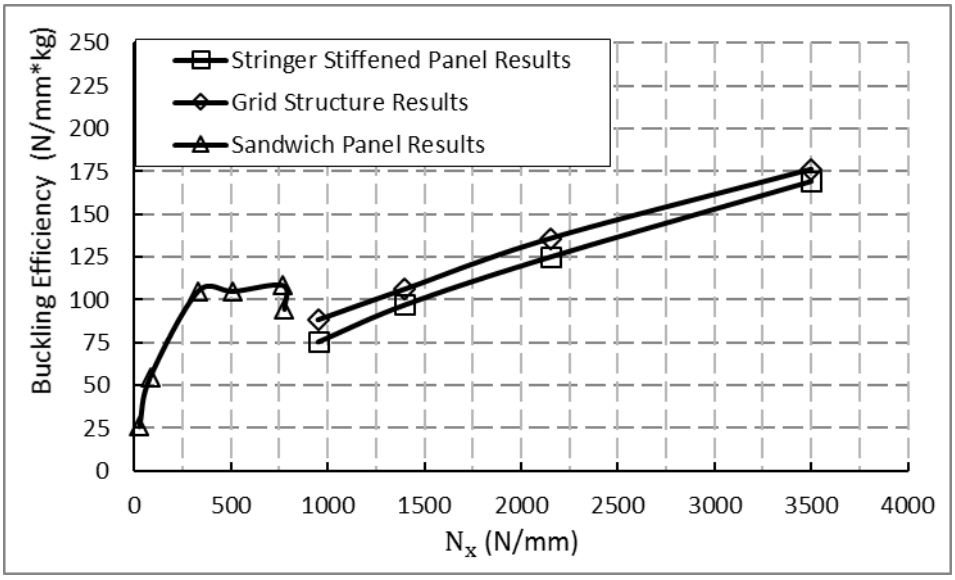

Figure 3.25 Efficiency under combined load of 30% shear force

3.4 Conclusion and Discussion

In this chapter, buckling efficiencies of three different optimal designed structure types, composite sandwich panels, metallic stringer-stiffened panels, and metallic grid structure were studied and compared to determine the most efficient structure type in a specific loading condition subject to buckling.

Under uniaxial compression load condition, the optimal design of sandwich panel was carried out starting from parametric studies of three design parameters, composite skin layup, sandwich panel core height, and skin thickness. The parametric study shows for the loading condition, an optimal design of sandwich panel can be achieved at a core height to let buckling and

wrinkling occur at the same loading with a skin layup of $[0^{\circ}/90^{\circ}]\mathrm{n}_s$ plies. For metallic stringer stiffened panel, Emero's optimal design method is applied. The design was verified through ESDU package and Patran/Nastran. The verification shows Emero's method gives buckling stress with less than 10% error compare with FE and ESDU package results. Emero's optimal ratio stiffeners were applied as transvers stiffeners in $0^{\circ}/90^{\circ}$ grid structures and from Patran/Nastran analysis results, it shows that the difference between the buckling load of local buckling and global buckling of these optimal design structures were around 10%. These structures were considered as metallic cross grid structure optimal design. The buckling efficiencies of these structures are plotted and compared. The comparison results showed that under axial distributed compression load, in the low distributed load range (750 N/mm in this case) sandwich panel is the most efficient structure type and in the rest of the load range stringer stiffed panels should be used.

Combined load conditions were considered by introduce a shear stress load factor to determine the shear load to axial compression load ratio. The buckling efficiencies of stringer stiffened panels and grid structures were calculated through Patran/Nastran with shear load ratio of 10%, 20%, and 30%. The results showed that stringer stiffened panels are sensitive to shear load ratio and the buckling stress reduce along with the increase of shear load ratio. For grid structures, the buckling stress gently decreases with the increase of the shear load ratio and with the increase of the ratio, grid structure starts to be more efficient than stringer stiffened panel from the low load range. At the shear load ratio of 30%, the efficiencies of grid structure were beyond that of stringer stiffened panel in the whole load range. Sandwich is not sensitive to the shear load ratio and in a combination load condition with 30% of shear load the buckling stress drops less than 10% compared with the axial compression load results. In these results, the sandwich panel is the most efficient structure type in the low load range (0-800 N/mm). With a shear load ratio less than 10%, stringer stiffened panel is still the optimal design within the rest of the practical

load range. For shear load ratios more than 20%, grid structure becomes more efficient than stringer stiffened panel in the low load range and when the shear load ratio over 30% grid structure is the most efficient structural type in the whole high load range.

From the study in this chapter, a guideline for structural engineers to determine the most effective structure type against buckling under a given load condition can be concluded. The comparison of buckling efficiencies of composite sandwich panel, metallic stringer stiffened panel, and metallic grid structure shows sandwich panel is the most efficient structure type in both load conditions in the low load range (0-800 N/mm). Under an axial distributed compression load, stringer stiffened panel should be used in the high load range (800–3500 N/mm) and under a compression and shear combined load condition, with the increase of the shear load ratio, grid structure becomes more efficient starting from the low load range and at around the ratio of 30% it becomes the optimal structure type in the entire high practical load range (800–3500 N/mm).

For a composite stringer stiffened panel or grid structure, the efficiency of the structure type would increase due to the high stiffness to weight ratio of composite material properties. The sandwich panels are still more efficient than composite stringer stiffened panels or grid structure in the low load range. In the later chapters, stringer stiffened panel is chosen as the structure type used in design because of its high performance against buckling within a wide load range.

4 Parametric Study of Optimal Composite Stringer Stiffened Panel Design

In this chapter, an optimal design method for metallic and composite stringer stiffened panels under compressive distributed load is investigated. The investigation started from case studies of Emero's optimal design method [27] for metallic stringer stiffened panels to explore the potential of the method and to extend it from single section to multi stringer stiffened panel design. Niu's practical design ratios [28] were introduced as realistic design constraints and design ratios of a practical optimal design should fall into these ranges. Essentially, a practical optimal design method is developed for optimal metallic stringer stiffened design based on Emero's optimal design method with practical design ratios. The design results using the modified method are verified through ESDU data sheets [157] and Patran/Nastran FE package. The results show that the method can provide a design of metallic stringer stiffened panel design with a difference of global and local buckling stress less than 10%.

The optimal method was further developed for composite stringer stiffened panels by replacing corresponding metallic stiffness terms in the equation with composite material stiffness for symmetric layup laminate skins and stringers. The design was verified through Patran/Nastran and the verification results of composite stringer stiffened panels designed with the method show that the method gave optimal design of composite stringer stiffened panel and let local buckling and global buckling of the design close to each other under a practical layup in a practical load range.

This design method provides optimal design of stringer stiffened panel with practical design constraints. Design tools were developed according to the methods for metallic and composite stringer stiffened panels design.

4.1 Emero's Optimal Design Method for Metallic Stringer Panels

4.1.1 Three Cases by Using Emero's Method

Emero's optimal design method [27] is introduced in Chapter 2 and applied in the optimal design of metallic stringer stiffened panel in Chapter 3. In this section an optimal design method of metallic stringer stiffened panel with practical design ratios is investigated. The optimal design method has been developed from Emero's optimal design method for metallic stringer stiffened panels [27]. Basically, Emero's method is based on applying Euler beam instability equation for global buckling estimation and distributed moment theory to calculate local buckling coefficient for local buckling stress estimation, by letting the global buckling equals to local buckling an optimal design can be determined. Euler equation and distributed moment method are developed from single beam under uniaxial compression load condition. A case study was carried out to verify whether the optimal design method originally developed for a single stiffener can be extended to a multi-stiffener panel.

The case studies that are carried out on a wing structure of a commercial aircraft [80] are displayed in Figure 4.1 and the spanwise loading distribution of the wing is shown in Figure 4.2. Three different load cases (500 N/mm, 2850 N/mm, 5250 N/mm) were taken along the span, which cover the whole range of load level. For each load case, three panels with different stringer types, blade, I section, and Z section were considered in the case studies. The sizes of panels vary from 5 stringer-skin sections to 15 sections with the same section geometry. The panel length is 600 mm and the panel width varies along with the stinger number and optimal design pitch of single section. The Young's modulus of the material is 7.20E4 MPa and the Poisson's ratio is 0.3.

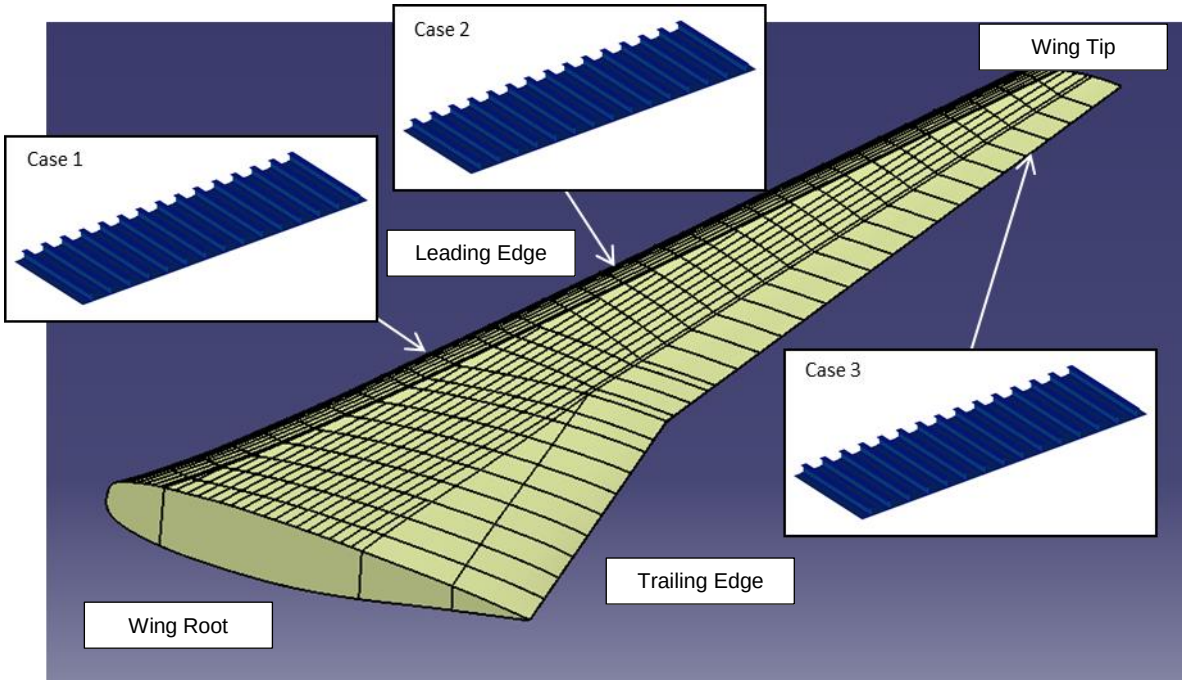

Figure 4.1 Three load cases panels' locations

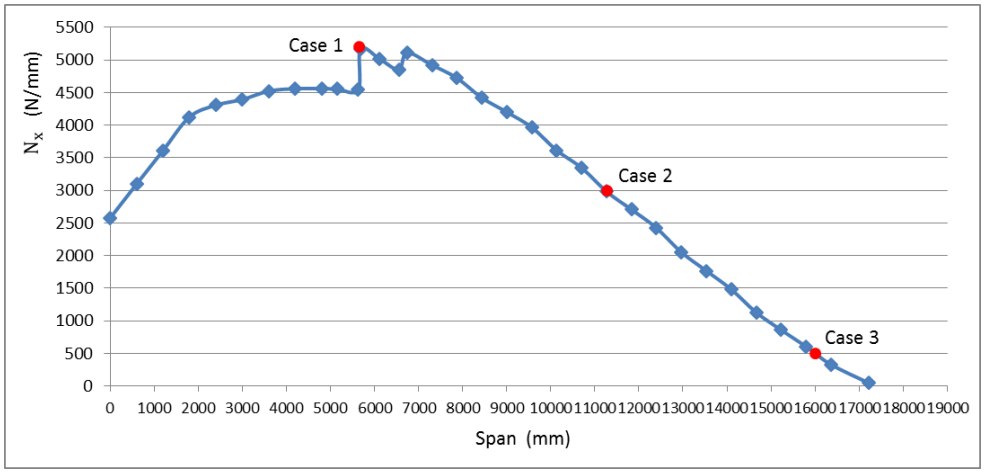

Figure 4.2 Distributed load along spanwise

The initial optimal design dimensions for the stringer and skin sections are calculated by using Emero's method for each loading case. Based on the parameter ratios from Table 3.8 and through Eq. (2.10) to Eq. (2.13), the initial panel section dimensions and buckling stress of blade stringer stiffened panel were calculated and listed in Table 4.1.

Table 4.1 Optimal design results

Distributed Load N/mm	Design Parameters						Design Results mm				Buckling Stress N/mm²
N_x	ε	r_{bw}	r_{tw}	α	β	γ	t_w	t_s	b_w	b_s	
500	0.656	0.65	2.25	2.4625	0.4753	0.206	2.303	1.023	30.257	46.549	198.39
2850	0.656	0.65	2.25	2.4625	0.4753	0.206	5.498	2.443	46.751	71.925	473.66
5250	0.656	0.65	2.25	2.4625	0.4753	0.206	7.462	3.316	54.465	83.793	642.87

4.1.2 The ESDU and FE Method Evaluation

The Emero's results were verified through ESDU 098016 package [157] and Patran/Nastran FE methods. The ESDU 098016 package [157] based on finite strip method provides a semi analytical and numerical analysis tool for calculating local and global buckling stress of metallic stringer stiffened panels. It is thus used here to compare and validate Emero's results. In the case study, simply support condition was applied to the panel side edges. Local and global buckling analyses were carried out separately. Stringer Number (NoS) varies from 5 to 15 and global/local buckling analyses were carried out respectively. The results are listed in Table 4.2.

```
Stringer shape: Blade
30 Stringers are used
input.pgd

material.mat
N
mm
1       15
0       0       0
0       0       0
54.465  7.462   1
83.793  3.316   1
41.896  1
41.896  1
600.000 1       1
1       1
```

a) ESDU 098016 Input File

```
------------------------------------------------------------
Panel Properties
------------------------------------------------------------
Panel section Area                0.104494E+05 mm^2
Distance of Centroid from z = 0   0.168679E+02 mm
Panel Bending Stiffness, EIyy     0.261010E+12 N mm^2
------------------------------------------------------------


------------------------------------------------------------
Buckling Results
------------------------------------------------------------
Buckling Strain                  -0.882128E-02
Buckling Stress                  -0.635132E+03 N/mm^2
Panel Buckling Load              -0.663674E+07 N
------------------------------------------------------------
```

b) ESDU 098016 Global Buckling Results

```
------------------------------------------------------------
Results for Local Buckling
------------------------------------------------------------
Step     L          Eps-cr     Sigma-cr    Buckling Load
         mm                    N/mm^2           N

  1 0.1000E+01 -0.384369 -0.276746E+05 -0.289182E+09
  2 0.2820E+02 -0.016487 -0.118709E+04 -0.124043E+08
  3 0.5540E+02 -0.009210 -0.663145E+03 -0.692946E+07
  4 0.8260E+02 -0.009658 -0.695405E+03 -0.726656E+07
------------------------------------------------------------
```

c) ESDU 098016 Local Buckling Results

Figure 4.3 ESDU 098016 input and output

FEM as a numerical method is also chosen to compare with the above two methods and results. The FE models for 5, 10, and 15 stringers panels with blade stringers were set up with 4-node shell elements. The blade stringer section definition is given in Figure 3.7. FE model of 15 blade stringers stiffened panel is shown in Figure 4.4. Unit pressure was applied to panel skin and stringer sections. The boundary conditions applied to the panel are illustrated in Figure 4.5 and loaded stringer edges were constrained in z direction displacement and all rotational degrees of freedom which were made the same as Emero's assumptions. Linear buckling analyses were processed for 5, 10, and 15 stringers stiffened panels' cases. The results are listed in Table 4.2.

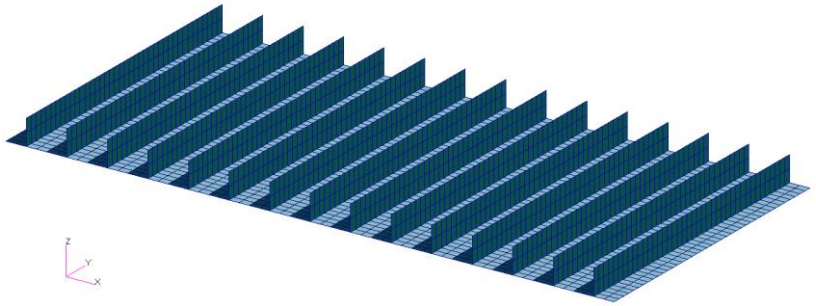

Figure 4.4 FE shell model for three structure types

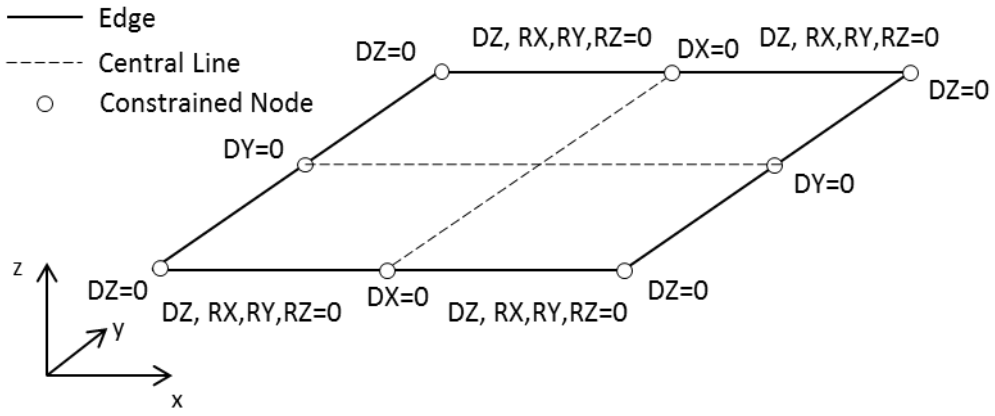

Figure 4.5 FE boundary conditions

Design results from Emero's method at three load cases are given in the initial optimal design dimensions for the stringer and skin sections are calculated by using Emero's method for each loading case. Based on the parameter ratios

from Table 3.8 and through Eq. (2.10) to Eq. (2.13), the initial panel section dimensions and buckling stress of blade stringer stiffened panel were calculated and listed in Table 4.1.

Table 4.1 and compared with ESDU 098016/Nastran. The buckling load factors, the buckling stress divided by applied stress, are calculated from the verification methods in Table 4.2.

Table 4.2 Emero's method compared with ESDU and Nastran

$N_x = 500$ N/mm							
	ESDU 98016			Nastran			Emero
NoS	Local	Global	Critical	Local	Global	Critical	
5	1.0361	1.0955	1.0361	1.0256	1.0692	1.0256	1.00
6	1.0340	1.0779	1.0340				1.00
7	1.0327	1.0647	1.0327				1.00
8	1.0318	1.0546	1.0318				1.00
9	1.0312	1.0468	1.0312				1.00
10	1.0308	1.0404	1.0308	1.0036	1.0111	1.0036	1.00
11	1.0305	1.0352	1.0305				1.00
12	1.0303	1.0308	1.0303				1.00
13	1.0301	1.0272	1.0272				1.00
14	1.0299	1.0241	1.0241				1.00
15	1.0298	1.0216	1.0216	0.9947	0.9989	0.9947	1.00

a) N_x = 500 N/mm

$N_x = 2850$ N/mm							
	ESDU 98016			Nastran			Emero
NoS	Local	Global	Critical	Local	Global	Critical	
5	1.0365	1.0391	1.0365	1.0266	0.9688	0.9688	1.00
6	1.0348	1.0276	1.0276				1.00
7	1.0339	1.0192	1.0192				1.00
8	1.0332	1.0129	1.0129				1.00
9	1.0327	1.0082	1.0082				1.00
10	1.0323	1.0047	1.0047	1.0209	0.9327	0.9327	1.00
11	1.0321	1.0020	1.0020				1.00
12	1.0319	1.0002	1.0002				1.00
13	1.0317	0.9991	0.9991				1.00
14	1.0316	0.9985	0.9985				1.00
15	1.0315	0.9984	0.9984	1.0198	0.9302	0.9302	1.00

b) N_x = 2850 N/mm

$N_x = 5250$ N/mm							
	ESDU 98016			Nastran			Emero
NoS	Local	Global	Critical	Local	Global	Critical	
5	1.0371	1.0157	1.0157	0.9987	0.9199	0.9199	1.00
6	1.0355	1.0062	1.0062				1.00
7	1.0345	0.9995	0.9995				1.00
8	1.0338	0.9946	0.9946				1.00
9	1.0334	0.9912	0.9912				1.00
10	1.0332	0.9888	0.9888	0.994	0.8916	0.8916	1.00
11	1.0330	0.9874	0.9874				1.00
12	1.0328	0.9868	0.9868				1.00
13	1.0325	0.9868	0.9868				1.00
14	1.0318	0.9872	0.9872				1.00
15	1.0315	0.9880	0.9880	0.9931	0.8921	0.8921	1.00

c) N_x = 5250 N/mm

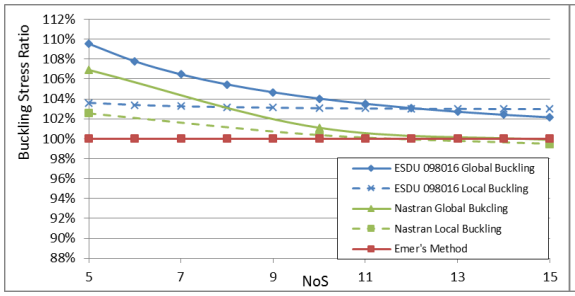

a) N_x = 500 N/mm

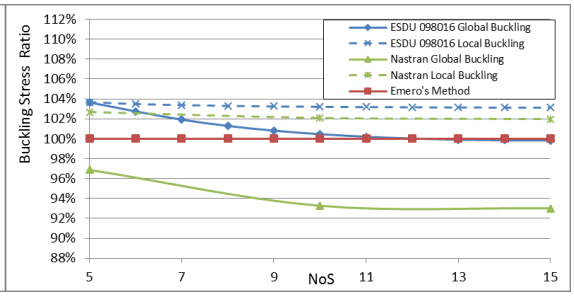

b) N_x = 2850 N/mm

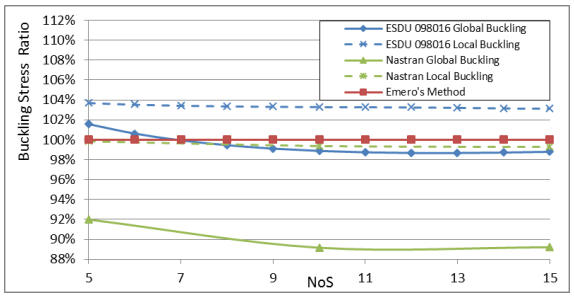

c) N_x = 5250 N/mm

Figure 4.6 Emero's method compared with ESDU and Nastran

From Table 4.2 a) and Figure 4.6 a), the results show that with the increase of stinger numbers, the buckling stresses of ESDU and Nastran results decrease to less than 2% error from the converge value when the number of stringers over 11. It is shown that at stringer number of 15 the buckling stress is stable and fully converged, so for later analyses a stiffened panel with 15 stringers pattern was applied. The global buckling stress is close to local buckling stress for the results from all methods. The error between Emero's optimal design method with ESDU and Nastran is 2% and 0.5% respectively at the distributed compression load of 500 N/mm.

By comparing all load cases, with the increase of distributed load, the global buckling stresses for both verification methods decreased and they converge at a stress level lower than local buckling in all load cases. The local buckling is less sensitive to stringer number compare with global buckling for both

verification methods which means less sensitive to boundary conditions in all case studies. The error between buckling stresses calculated using Emero's method and Nastran increased up to 10% at 5250 N/mm which is the upper boundary of the practical load range. The results show that Emero's method gives a good agreement with the ESDU results in less than 2% error within the load range.

From this case study, an optimal number of stringers can be obtained as 15 and the maximum deviation between Emero's and FE results is less than 10% within the provided load range for blade stiffened panel. The deviation is less 2% when compared with ESDU results. Similar studies have been carried out on I-stringer and Z-stringer stiffened panels with close trends and conclusions. What should be mentioned here is that the stringer pitch of optimal design from Emero's method was far less than 200 mm which is a practical design requirement for inspection and repair. It can be further concluded that Emero's method has a high buckling efficiency but cannot satisfy practical design requirements.

4.1.3 Practical Design Constraints by Niu

Emero's method provides optimal design under a given compressive distributed load. Niu [28] also provided a set of design ratios considering practical design requirements listed in Table 2.3 without providing any efficiency or buckling stress calculation method. The following case study is used to compare buckling efficiencies of stringer stiffened panels designed with the ratios from each method. Z section stringer was taken as an example and ESDU 098016 was used to estimate the buckling stress of the stiffened panels with design ratios. The flange length (b_f) was 40% of web height (b_w) and flange thickness was the same as web thickness. The stringer number of stiffened panel was 15 and the Emero's efficiency calculation method was applied to those panels designed with Niu's ratios. The material used in the section is the same as that

in Section 4.1.1. The upper boundary and lower boundary of Niu's design ratios are calculated and listed in Table 4.3.

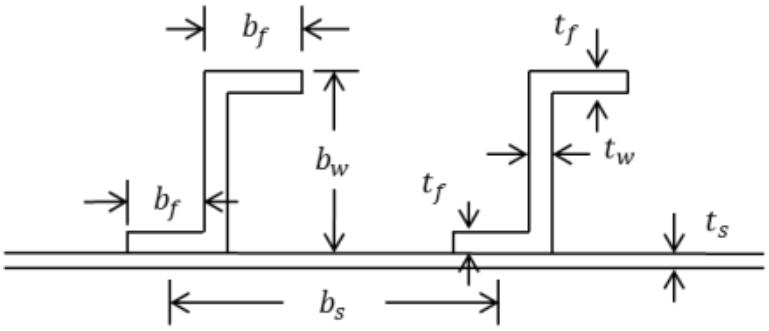

Figure 4.7 Parameter definition of Z section stringer

Table 4.3 Buckling efficient of Niu's design ratios

Upper Efficiency Boundary				
N_x N/mm	6185	2298	838	363.5
t_w/t_s	0.5	0.6	0.7	0.8
K	3.21	3.88	4.07	4.35
b_w/b_s	0.556	0.463	0.397	0.347
ε	0.685	0.628	0.551	0.498
b_w/t_w	20.00	20.00	20.00	20.01
Stress N/mm^2	713	416	235	147
t_s mm	5.78	3.68	2.37	1.64

Lower Efficiency Boundary				
N_x N/mm	9425	3503	1277	554
t_w/t_s	0.5	0.6	0.7	0.8
K	3.21	3.88	4.07	4.35
b_w/b_s	0.556	0.463	0.397	0.347
ε	0.685	0.628	0.551	0.498
b_w/t_w	18.00	18.00	18.00	18.00
Stress N/mm^2	880	514	291	182
t_s mm	7.14	4.55	2.93	2.03

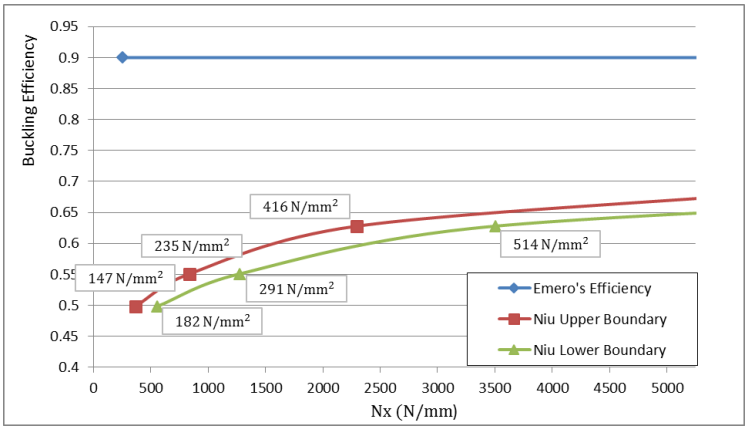

Figure 4.8 Efficiency of Emero's method compared with Niu's method

The results show that the buckling efficiency of Z stringer stiffened panel with Niu's design ratios varies from 0.5 to 0.68 along with the increase of distributed load. The efficiency difference between the upper and lower boundaries of Niu's design ratios is about 0.05 at a specific load within the load range. Compared with the efficiency of optimal design provided through Emero's method in Table 2.2, Niu's design is at least 25% less efficient.

4.1.4 Optimal Design Method with Practical Constraints

Niu's design ratios are not able to give section dimensions and buckling stress based on a given load condition. On the other hand, Emero's method is theoretical without practical constraints. A study was therefore carried out to combine Emero's design method within Niu's design ratios to design a practical stiffened panel of comparatively high efficiency against buckling. As an example, I-stringer section was taken in this case study with the selected practical design ratios are listed in Table 4.4. As discussed in the Emero's case study, the pitch given by Emero's optimal design method is too small for practical design so within the optimal design method a stringer pitch is given as a design constraint along with Niu' design ratios. Different from Emero's method with a given panel length, the method calculates the panel length subject to global buckling. If the length of the panel is less than this calculated panel length, it indicates local buckling occurs before global buckling.

Table 4.4 Niu's design ratios for Emero's method

$\frac{t_f}{t_w}$	$\frac{b_w}{t_w}$	$\frac{b_f}{t_f}$	$\frac{A_{St}}{A_{Sk}}$	$\frac{b_f}{b_w}$
1.0	18 - 22	6 - 8	0.5	0.4

The method gives a compromise optimal design of weight and practical requirements. A flow chart of the method is given in Figure 4.9

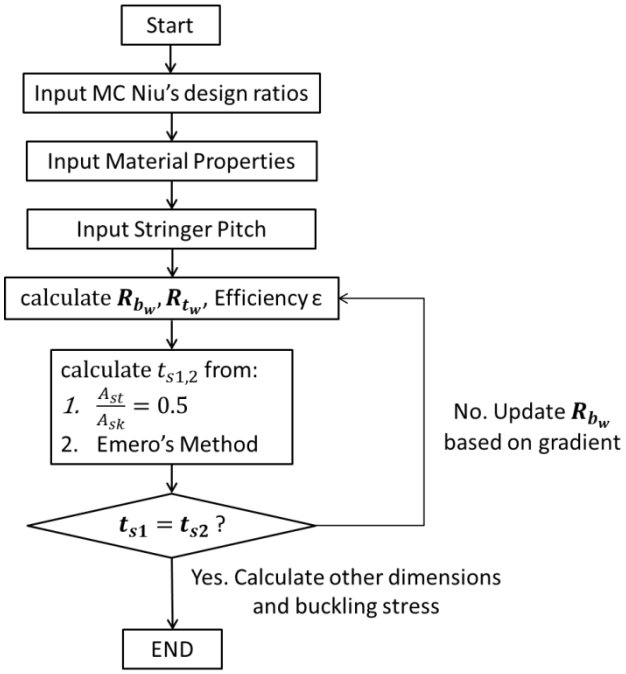

Figure 4.9 Flow chart for practical optimal design method

This method was applied to I section stringer stiffened panel design with distributed load 500 N/mm, 2850 N/mm, and 5250 N/mm. I section stringer stiffened panel geometry definition is given in Figure 4.10. A 15-stringer stiffened panel configuration was used. The design results verified through ESDU and Nastran are listed in Table 4.5.

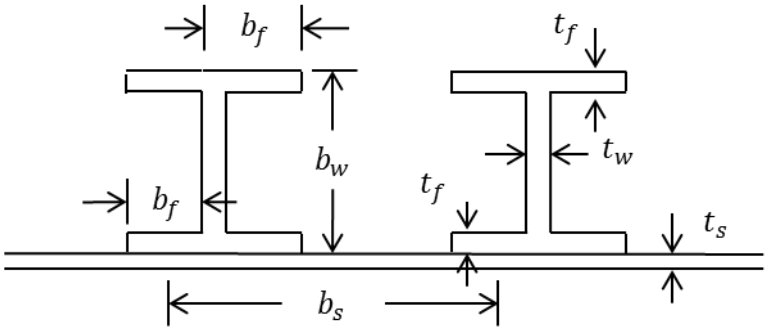

Figure 4.10 I section geometry definition

Table 4.5 Design results for I stringer stiffened panels

N_x = 500 N/mm		**Panel Length = 1450 mm**	N/mm²
b_f mm	19.64	**Emero's Buckling Stress**	95.73
t_f mm	2.73	**ESDU 098016 Results**	
b_w mm	49.10	Global Buckling Stress	96.60
t_w mm	2.73	Local Bukcling Stress	112.33
b_s mm	200.00	**Nastran Results**	
t_s mm	3.48	Global Buckling Stress	98.66
ε	0.37	Local Bukcling Stress	103.14

a) Design at N_x=500 N/mm

N_x = 2850 N/mm		**Panel Length = 1127 mm**	N/mm²
b_f mm	26.76	**Emero's Buckling Stress**	293.92
t_f mm	3.72	**ESDU 098016 Results**	
b_w mm	66.90	Global Buckling Stress	297.92
t_w mm	3.72	Local Bukcling Stress	328.17
b_s mm	200.00	**Nastran Results**	
t_s mm	6.46	Global Buckling Stress	304.40
ε	0.47	Local Bukcling Stress	300.31

b) Design at N_x=2850 N/mm

N_x = 5250 N/mm		**Panel Length = 1030 mm**	N/mm²
b_f mm	29.79	**Emero's Buckling Stress**	436.74
t_f mm	4.14	**ESDU 098016 Results**	
b_w mm	74.49	Global Buckling Stress	423.86
t_w mm	4.14	Local Bukcling Stress	473.60
b_s mm	200.00	**Nastran Results**	
t_s mm	8.01	Global Buckling Stress	437.27
ε	0.52	Local Bukcling Stress	447.60

c) Design at N_x=5250 N/mm

	Buckling Load Factor		
N_x N/mm	Emero's Results	ESDU 098016 Results	Nastran Results
500	1.00	1.01	1.03
2850	1.00	1.01	1.02
5250	1.00	0.97	1.00

d) Buckling Load Factor Summary

The results in Table 4.5 a) show that the method calculates a set of stringer stiffened panel geometry dimensions satisfying Niu's design ratios and practical stringer pitch at a distributed compression load of 500 N/mm. The global buckling stress and local buckling stress calculated through ESDU and Nastran of the panel were close within 5% deviation and the stress results had a good agreement with the buckling stress estimated through Emero's method. The efficiency was 0.37 and compared with the optimal buckling efficiency 1.00, the optimal practical design was less efficient than Emero's optimal design. From Table 4.5 a), b), and c), with the increase of the compression load, the buckling efficiency and buckling stress given by the method increases. From the buckling stresses calculated by ESDU and Nastran show that the method gives optimal design. The buckling load factors given in Table 4.5 d) and plot in Figure 4.11 show the method can be applied to the entire load range with a good agreement with ESDU and Nastran results and error is less than 3% for both ESDU and Nastran results.

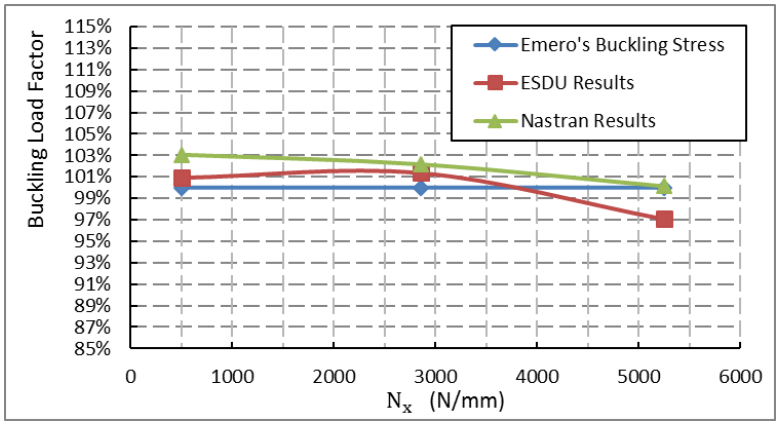

Figure 4.11 Buckling load factor plot of I stringer design

In this section, three case studies are carried out by applying Emero's optimal design method for practical optimal metallic stringer stiffened panel design. The case studies started from blade stringer stiffened panels designed through Emero's method at three load conditions within a practical load range. The results from this case study shows that through Emero's method was developed from single stinger section model with elastic boundary but the method can be applied to a multi-stringer stiffened panel and the estimation results are verified through ESDU 098016 and Nastran with less than 10% error in the whole load range. To compare the buckling efficiencies of optimal design and practical design with Niu's ratios, the second case study was processed. Buckling efficiencies of practical design increase along with the distributed load increase and the maximum efficiency of the upper boundary of the design within Niu's design ratios is 25% less efficient than Emero's optimal design. Emero's method cannot be applied in practical design due to unrealistic ratios and too small stringer pitch. A method is developed to make up this shortage with a combination of Emero's method and Niu's practical design ratios. The third case study was used to verify this method within the practical load range with a reliable design which can match ESDU and Nastran results. The results show that less than 3% error can be achieved for I section stringer stiffened panel with the method. The design results are optimal design with practical ratios although the buckling efficiencies were comparatively low to Emero's optimal

design ratios. The method was further applied to composite material stringer stiffened panels in the next section.

4.2 Optimal Design for Composite Stringer Stiffened Panels

4.2.1 Key Parameters Effect on the Application of Metallic Tool to Composite – Modules Sensitivity Study

Wang et al. [160] investigated optimal buckling design of composite stringer stiffened panels and concluded that buckling stress of a composite stringer stiffened panel is most sensitive to geometry ratios of panel cross section. Based on Emero's method for optimal geometry ratios for metallic stringer stiffened panels against buckling and the study on practical constraint of design ratios and stringer pitch, investigation in this section is focused on potential application of the method to composite stiffened panel design.

The sensitivity analysis of composite laminate buckling to the modules was carried out for a flat composite plate based on Classic Laminate Plate Theory for two-dimensional analysis. With shear deformation, the assumptions of Classic Laminate Theory remain except the deformed cross section plane may not keep normal to the neutral plane anymore. Classic Laminate Plate Theory is used in the section and the equilibrium equation for a laminate thin plate with in-plane and bending moment is given in Eq. (4.1):

$$D_{11}\frac{\partial^4 w}{\partial x^4} + 4D_{16}\frac{\partial^4 w}{\partial x^3 \partial y} + (2D_{12} + 4D_{66})\frac{\partial^4 w}{\partial x^2 \partial y^2} + 4D_{26}\frac{\partial^4 w}{\partial x \partial y^3} + D_{22}\frac{\partial^4 w}{\partial x^4}$$
$$+ B_{11}\frac{\partial^3 u_0}{\partial x^3} + 3B_{16}\frac{\partial^3 u_0}{\partial x^2 \partial y} + (B_{12} + 2B_{66})\frac{\partial^3 u_0}{\partial x \partial y^2} + B_{26}\frac{\partial^3 u_0}{\partial y^3}$$
$$+ B_{16}\frac{\partial^3 v_0}{\partial x^3} + (B_{12} + 2B_{66})\frac{\partial^3 v_0}{\partial x^2 \partial y} + 3B_{26}\frac{\partial^3 v_0}{\partial x \partial y^2} + B_{22}\frac{\partial^3 v_0}{\partial y^3} \quad \textbf{(4.1)}$$
$$+ p + N_x\frac{\partial^2 w}{\partial x^2} + N_y\frac{\partial^2 w}{\partial y^2} - 2N_{xy}\frac{\partial^2 w}{\partial x \partial y} = 0$$

For orthotropic laminates, the conditions are

$$A_{16} = A_{26} = 0$$
$$[B] = 0 \quad \textbf{(4.2)}$$
$$D_{16} = D_{26} = 0$$

These laminate property conditions with simply supported boundary conditions on edges gives Eq. (4.3) under a compression load applied in-plane x direction.

$$N_{x,critical} = \pi^2\left[D_{11}\left(\frac{m}{a}\right)^2 + 2(D_{12} + 2D_{66})\left(\frac{1}{b}\right)^2 + D_{22}\left(\frac{1}{b}\right)^4\left(\frac{a}{m}\right)^2\right] \quad \textbf{(4.3)}$$

The critical buckling stress can be obtained by putting n=1 and a positive integer m giving minimum N_x. In terms of buckling stress which is the Eq. (2.9)

$$\sigma_{cr,min} = \frac{2\pi^2}{tb^2}\left[(D_{11}D_{22})^{\frac{1}{2}} + D_{12} + 2D_{66}\right] \quad \textbf{(2.9)}$$

The composite laminates studied in this section were symmetric layup plies for practical application purpose providing zero terms in B matrix of ABD matrices and further leads to no in-plane and twist coupling which gives in Eq. (4.2). The ply properties of IM7/8552 are given in Table 3.4 and shell elements are used for this FE model. Four ply orientations were considered, (0˚, 90˚, and ±45˚) due to limited ply orientations were available for a laminate to stack with in industry.

The composite plate of 600x600 mm made of 16 ply symmetric layup laminate $[45/0/-45/90/45/0/-45/90]_s$ was evaluated through Patran/Nastran with the 1st buckling mode shown in Figure 4.12. The stiffness modulus of the D matrix of the laminate are listed in Table 4.6. The boundary condition was given in Figure 3.4. The edges were simply supported and X/ Y direction displacement constraints are applied at the centre of the edges. The buckling stress from FE results was 2.58 MPa which agrees very well with theoretical solution given in Table 4.7, the difference being less than 2%.

Table 4.6 [D] matrix properties of the laminate

	D_{11}	D_{22}	D_{12}	D_{66}
Modulus ($\mathrm{N/mm^2}$)	5.21E4	3.51E4	1.67E4	1.81E4

Table 4.7 Analytical buckling stress solutionn of the composite flat plate

t (mm)	b (mm)	σ (MPa)
2	600	2.62

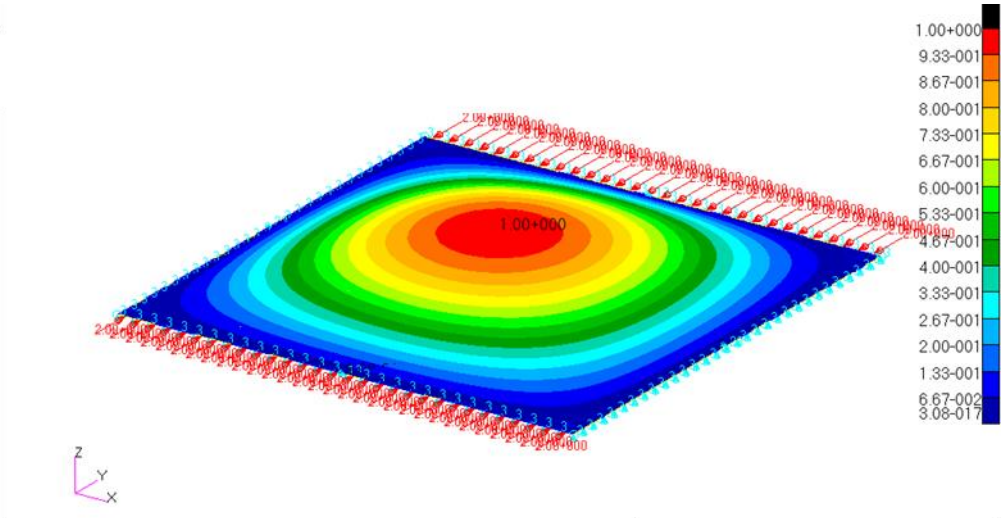

Figure 4.12 Global buckling mode of a composite plate

$$\{k\} = [D]^{-1}\{M\} = [d]\{M\}$$
$$\{e\} = [A]^{-1}\{N\} = [a]\{N\} \quad \textbf{(4.4)}$$

$$E_{bending} = \frac{1}{I}\frac{M}{k} = \frac{12}{t^3}\frac{1}{d_{11}} \quad \textbf{(4.5)}$$

$$E_{member} = \frac{1}{ta_{11}}$$

In order to extent Emero's optimal design method developed for metallic stiffened panels to composite stiffened panels, the equivalent laminate modulus of a quasi-isotropic composite plate was calculated first. The modulus in member and bending mode were used to calculate the buckling stress and compare with the composite laminate with the layup$[0/0/45/-45/45/-45/90/90]_s$. The two modulus 6.21E4 and 1.05E5 were used in the same plate as shown in Figure 4.12. The resulting buckling modes as shown in Figure 4.13 is similar to Figure 4.12 and the results are listed in Table 4.8.

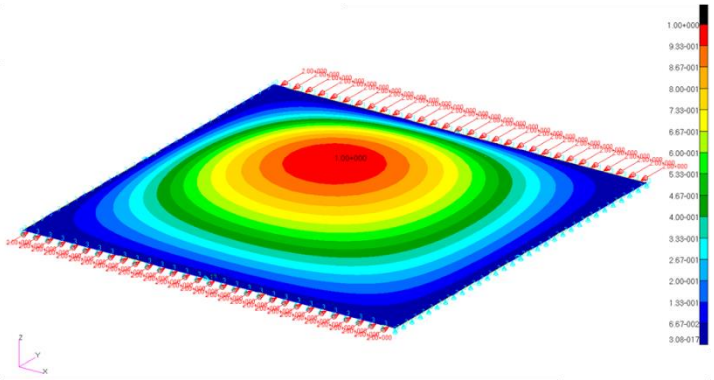

Figure 4.13 Global buckling mode of a quasi-isotropic plate

Table 4.8 Buckling stresses of dfferent modulu quasi-isotropic plates

	Member Modulus 6.21E4 (MPa)	**Bending Modulus 1.05E5 (MPa)**	**Composite Materials**
Buckling Stress (MPa)	2.59	4.2471	2.38

As shown in Table 4.8, the difference of the global buckling stress of the quasi-isotropic plate using the member modulus is about 8% from the composite laminate. The difference of global buckling stress of the plate using the bending modulus is 78% higher than that of the composite laminate. This is due to in plane compression loading is applied and the z direction displacement is

caused by in plane strain. So member modulus can be used as equivalent modulus in Euler equation for optimal design against buckling.

Recalling Eq. (2.8) and Eq. (2.9) and comparing them with those corresponding to the modulus terms of isotropic property plate and special orthotropic plate, an elastic modulus can be developed by replacing corresponding modulus terms in the equations for isotropic property plate calculation and shown in Eq. (4.6).

$$E_{local\ buckling} = \frac{1}{2}\left[(D_{11}D_{22})^{\frac{1}{2}} + D_{12} + 2D_{66}\right]\frac{12(1-\mu^2)}{t^3} \quad \textbf{(4.6)}$$

The elastic modulus calculated through the equation is used for local buckling estimation of the Emero's optimal design method.

In the optimal design method discussed in this section, the attention is drawn on optimal geometry shape rather than optimal layup as mentioned in beginning of this section. In order to obtain same elastic properties for skin and stringers required carrying out optimal geometry design, same layup but artificial ply thickness is applied. The laminate consists of 40 plies with a stacking sequence of $n[45/0/0/-45/90]_s$ and ply thickness of skin and stringer laminate is varying to fit in optimal skin. After optimal design, a post process can be carried out to trim stringer ply thickness to an ordinary thickness.

4.2.2 The Extension to Stiffened Panels (Effect of Layup Appears to be Sensitive)

In this section, the application of the optimal design method for a practical laminate composite stringer stiffened panels is verified. The optimal design method was firstly applied on a composite stringer stiffened panel of a laminate layup with 40% 0˚, 20% 90˚, and 40% ±45˚ plies at a distributed load of 2850 N/mm and then extend to the composite stringer stiffened panel design with

same laminate with distributed loads of 500 N/mm and 5250 N/mm covering the whole practical load range.

By replacing corresponding elastic modulus the optimal design method is developed for optimal design of composite stringer stiffened panels. The flow chart is the same as given in Figure 4.9. This method is applied to a 15 I section stringer stiffened panel design under a distributed compression load of 2850 N/mm and Patran/Nastran is used to evaluate this design. The composite material is IM7/8552 properties listed in Table 3.4 and 0˚, 90˚, and ±45˚ plies take 40%, 20%, and 40% respectively in the laminate layup for skins and stringers with a layup $\mathrm{n}[45/0/-45/90/-45/0/45]_s$. The boundary conditions for Patran/Nastran verification are given in Figure 4.5. The geometry dimensions of design results are given in Table 4.9.

Table 4.9 Optimal design of composite stringe stiffened panels

40/40/20			
$\mathrm{N_x} = 2850\ \mathrm{N/mm}$		**Panel Length = 1066 mm**	$\mathrm{N/mm^2}$
b_f mm	25.81	**Emero's Buckling Stress**	315.89
t_f mm	3.58		
b_w mm	64.53		
t_w mm	3.58		
b_s mm	200.00	**Nastran Results**	
t_s mm	6.01	Global Buckling Stress	337.78
ε	0.54	Local Bukcling Stress	300.38

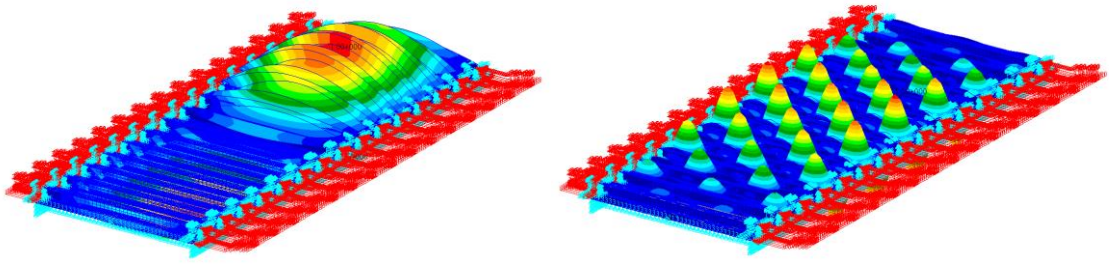

a) Global Buckling Mode b) Local Buckling Mode

Figure 4.14 Buckling of an optimal designed composite stringer stiffened panel

The buckling stress estimated through the method was about 4% higher than Nastran local buckling stress and shows that the method design gives an accurate estimation. The global buckling stress and local buckling stress estimated through Nastran is about 14% difference which shows the method can still provide an optimal design with global buckling stress and local buckling stress take place almost at the same loading.

The method was further applied to load cases of distributed load of 500 N/mm and 5250 N/mm. The same material, laminate layup and stacking sequence, and boundary conditions are applied. The Results are listed in Table 4.10 and buckling stresses are plot in Figure 4.15.

Table 4.10 Optimal design of composite stringer stiffened panel at different loads

40/40/20			
$N_x = 500$ N/mm		**Panel Length = 1450 mm**	N/mm^2
b_f mm	19.22	**Emero's Buckling Stress**	99.91
t_f mm	2.67		
b_w mm	48.06		
t_w mm	2.67		
b_s mm	200.00	**Nastran Results**	
t_s mm	3.34	Global Buckling Stress	115.15
ε	0.41	Local Bukcling Stress	101.52

40/40/20			
$N_x = 2850$ N/mm		**Panel Length = 1066 mm**	N/mm^2
b_f mm	25.81	**Emero's Buckling Stress**	315.89
t_f mm	3.58		
b_w mm	64.53		
t_w mm	3.58		
b_s mm	200.00	**Nastran Results**	
t_s mm	6.01	Global Buckling Stress	337.78
ε	0.54	Local Bukcling Stress	300.38

40/40/20			
$N_x = 5250$ N/mm		**Panel Length = 1030 mm**	N/mm^2
b_f mm	28.56	**Emero's Buckling Stress**	475.47
t_f mm	3.97		
b_w mm	71.39		
t_w mm	3.97		
b_s mm	200.00	**Nastran Results**	
t_s mm	7.36	Global Buckling Stress	478.90
ε	0.60	Local Bukcling Stress	440.12

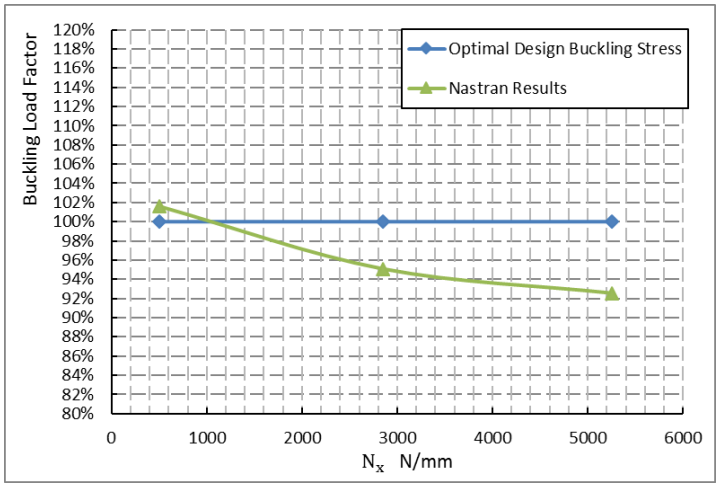

Figure 4.15 Buckling stress of optimal design at different loads

Table 4.11 Global and local buckling stress comparison

	Buckling Load Factor			
N_x N/mm	Global Buckling Stress MPa	Local Buckling Stress MPa	Optimal Bukcling Stress MPa	Global and Local Buckling Stresses Difference
500	115.15	101.52	99.91	13.4%
2850	337.78	300.38	315.89	12.5%
5250	478.90	440.12	475.47	8.8%

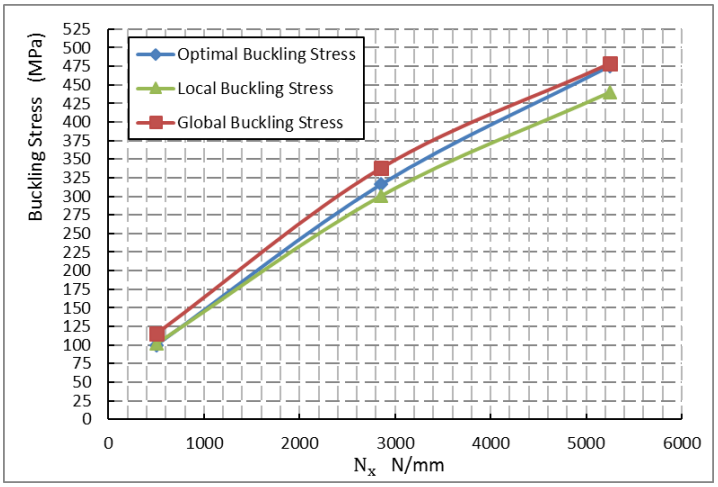

Figure 4.16 Buckling stresses under different loads

The results show that in the whole load range the buckling stress estimated through the optimal design method has a good agreement with Nastran results with a maximum difference about 7% at 5250 N/mm. Figure 4.16 illustrating buckling stresses, local buckling stresses, and buckling stresses estimated through optimal design method show that optimal buckling stress estimated lays between global and local buckling stress at the same distributed load. The difference between global and local buckling varies from 13.4% at 500 N/mm to 8.8% at 5250 N/mm and this result shows optimal design method can provide optimal design for composite stringer stiffened panels. In the lower load range, the optimal design method is comparatively conservative to Nastran calculated buckling stress. This shows the optimal design method can be used for a practical orientation ply type potion composite stringer stiffened panel design within practical load range.

4.2.3 The Effect of Key Parameters on the Application of Metallic Tool to Composite – Sensitivity Study of $\pm 45^{\circ}$ Plies Portion

In this section, sensitivity of the portion of ±45° plies in a laminate to buckling stress was studied. The sensitivity studies started from a distributed load 2850 N/mm and then were extended to distributed load 500 N/mm and 5250 N/mm which cover the whole practical design load range.

The effect of the portion of ±45° plies in the laminate at distributed load of 2850 N/mm was investigated by calculating buckling stresses of two different layups of $2[45/45/45/45/0/-45/-45/-45/-45/90]_s$ and $2[45/0/0/0/0/0/0/0/-45/90]_s$ respectively which give ±45° plies portion of 80% and 20%. The composite material properties are listed in Table 3.4 and boundary conditions used in Section 4.2.2 were applied. The section was designed with the optimal design method and results are summarized in Table 4.12 and Figure 4.17.

Table 4.12 Buckling stress and load factor of composite stringer stiffened panel at different ±45˚ ply portion

10/80/10			
$N_x = 2850$ N/mm		**Panel Length = 1450 mm**	N/mm^2
b_f mm	25.56	**Emero's Buckling Stress**	322.12
t_f mm	3.55		
b_w mm	63.90		
t_w mm	3.55		
b_s mm	200.00	**Nastran Results**	
t_s mm	5.90	Global Buckling Stress	307.95
ε	0.61	Local Bukcling Stress	367.09

70/20/10			
$N_x = 2850$ N/mm		**Panel Length = 1030 mm**	N/mm^2
b_f mm	26.28	**Emero's Buckling Stress**	304.71
t_f mm	3.65		
b_w mm	65.70		
t_w mm	3.65		
b_s mm	200.00	**Nastran Results**	
t_s mm	6.24	Global Buckling Stress	345.37
ε	0.55	Local Bukcling Stress	238.49

	Buckling Load Factor	
Portion	Emero's Results	Nastran Results
80%	1.00	0.96
40%	1.00	0.95
20%	1.00	0.78

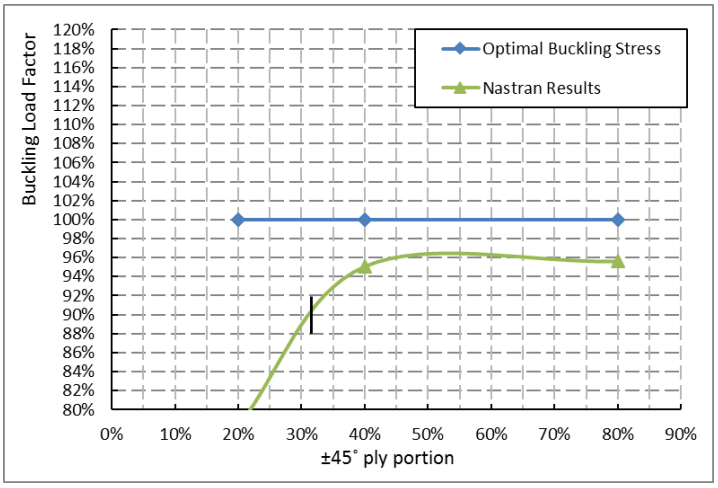

Figure 4.17 Buckling load factors at different ±45˚ ply portion

In Table 4.12, with the reduction of the ±45˚ ply portion, the difference between the buckling load factor estimated by Nastran and optimal design method is increasing up to 22% at a ±45˚ ply portion of 20%. If the ±45˚ ply portion is more than 30% the difference between optimal design method and Nastran estimation is less than 10%. The results are plotted in Figure 4.17.

The effect of the portion of ±45˚ plies to buckling stress in a laminate in the whole load range was investigated and the same two layups, material properties, and boundary conditions in the first sensitivity study were used. The results are listed in Table 4.13 and Figure 4.18.

Table 4.13 Optimal design of composite stringer stiffened panels at different ±45˚ ply portion

	Buckling Load Factor			
±45˚ ply portion	Global Buckling Stress MPa	Local Buckling Stress MPa	Optimal Buckling Stress MPa	Global and Local Buckling Stress Difference
80%	307.95	367.09	322.12	-16.1%
40%	337.78	300.38	315.94	12.5%
20%	345.37	238.49	304.71	44.8%

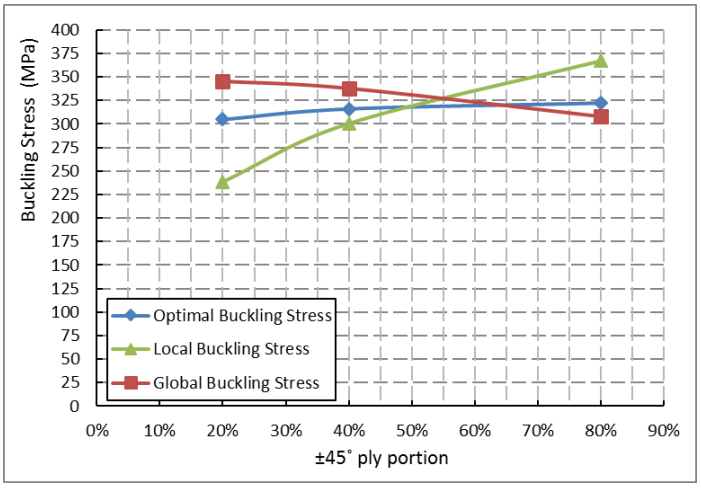

Figure 4.18 Buckling stress at different ±45˚ ply portion

The buckling stresses plotted in Figure 4.18 show different trends of local buckling and global buckling stress with the variation of ±45˚ ply portion at the distributed load 2850 N/mm. With the increase of ±45˚ ply portion, the local buckling stresses increases while global buckling stress decreases, and the intersection of global and local buckling stress at around 60%. Within the ±45˚ ply portion from 35% to 75%, the difference between global and local buckling stresses is less than 15%. Similar trends can be found at distributed load of 500N/mm and 5250 N/mm within a deviation of 10%.

From these results, the conclusion can be drawn that for composite ply IM7/8552 I section stringer stiffened panels with a practical symmetric layup (±45˚ ply portion from 35% to 75%) within the practical load range (500 N/mm to 5250 N/mm), optimal design method provides a design with buckling stresses less than 10% error with Nastran estimation and the difference between global and local buckling stresses is less than 15%.

4.3 Tools Developed for Optimal Stringer Stiffened Panel Design

4.3.1 Preliminary Sizing of Metallic Skin-Stringer Panels

This VB based design tool is developed for metallic stringer stiffened panels optimal design with practical design constraints [161]. The tool contains four stringer types options (Z section, J section, I section, and blade stringer) for optimal design. The internal method for geometry calculation is introduced in Section 4.1.4. The interface and the flow chart are given in Figure 4.19. The tool calculates the optimal section dimensions with the input design parameters with constraint ratios and call ESDU 098016 [157] for buckling stress estimation.

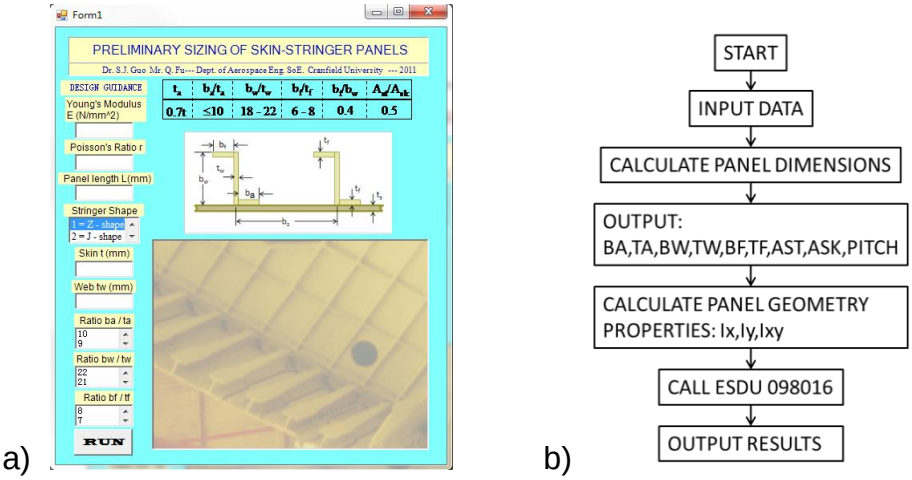

Figure 4.19 Interface and flow chart of ISoSSP V1.1

a) Interface of ISoSSP V1.1 b) Flow Chart of ISoSSP V1.1

The inputs are material properties, stringer type, skin and web thickness and Niu's design ratios an example is illustrated in Figure 4.20.

The difference between global and local buckling stresses is within a 10% deviation range. This tool provides a quick, reliable, and optimal design option for metallic stringer stiffened panels design at panel design stage.

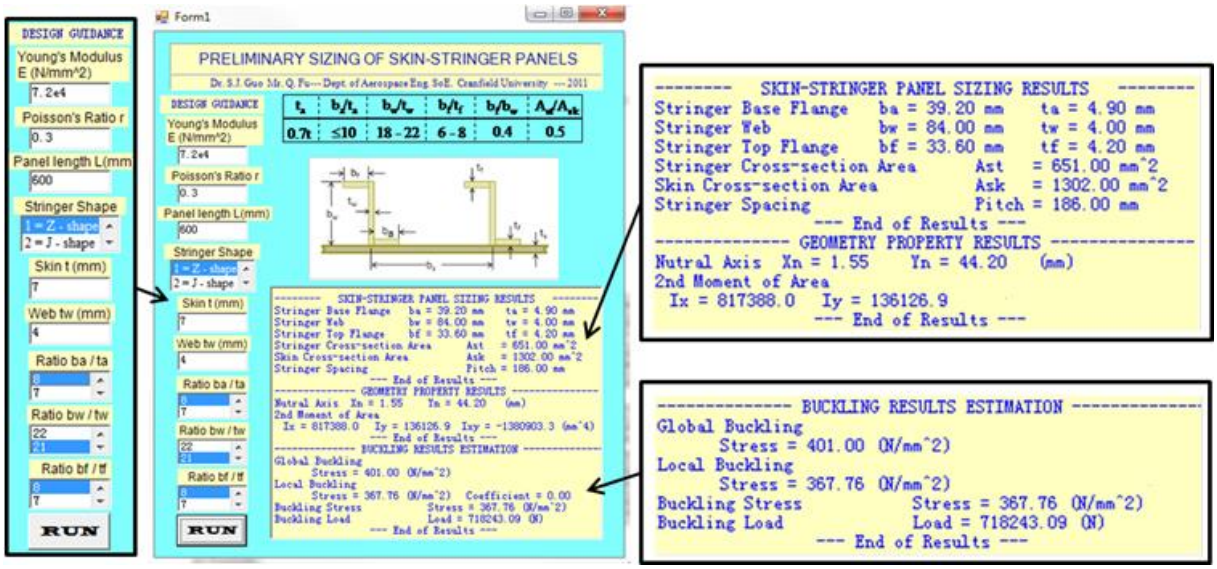

Figure 4.20 Input and output interface

4.3.2 Preliminary Sizing of Composite Skin-Stringer Panels

A FORTRAN based design tool was developed for composite stringer stiffened panels design [162]. The tool currently only contains blade section and I section stringer design options. The internal method is introduced in Section 4.2 and the output file is in a Nastran beam element input format can be directly input into Patran/Nastran. The flow chart of the tool is given in Figure 4.21.

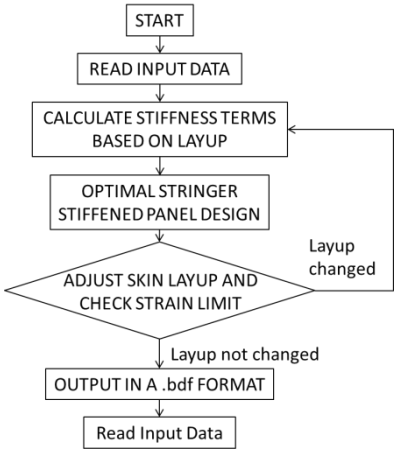

Figure 4.21 Flow chart of Preliminary Sizing for Composite Stiffened Panels

An example of the fixed format input and output of the tool is given in Figure 4.22.

a)

```
! Section ID | output type 1=.bdf 2=.pgd | stringer type (>0 US/ <0 LS) | Load Factor
1  1  4 1.00

! bw/tw | bf/bw | Ast/Ask | tf/tw
18.0 0.4 0.5 1.0

! Nx | bs | Panel Length
5250.00 200.00 600.0

! E1 | E2 | Poisson's Ratio | G12
164000. 12000.  .32     5310.

! Number of Layer | Ply thickness | Basic layup
5 0.125 45.0 0.0 0.0 -45.0 90.0

END
```

b)

```
PBARL   1                       I
        75.747  57.408  57.408  3.987   3.987   3.987
$ Maximum Panel Length: 980.010  | Stringer Pitch: 200.000  | Optimal Skin Thickness: 7.438
MAT8    1       164000. 12000.  0.320   5310.
PCOMP   1
        1       0.125   45.0    YES     1       0.125   0.0     YES
        1       0.125   0.0     YES     1       0.125   -45.0   YES
        1       0.125   90.0    YES     1       0.125   45.0    YES
        1       0.125   0.0     YES     1       0.125   0.0     YES
        1       0.125   -45.0   YES     1       0.125   90.0    YES
        1       0.125   45.0    YES     1       0.125   0.0     YES
        1       0.125   0.0     YES     1       0.125   -45.0   YES
        1       0.125   90.0    YES     1       0.125   45.0    YES
        1       0.125   0.0     YES     1       0.125   0.0     YES
        1       0.125   -45.0   YES     1       0.125   90.0    YES
        1       0.125   45.0    YES     1       0.125   0.0     YES
        1       0.125   0.0     YES     1       0.125   -45.0   YES
        1       0.125   90.0    YES     1       0.125   45.0    YES
        1       0.125   0.0     YES     1       0.125   0.0     YES
```

Figure 4.22 Input and output files

a) Input file ‘ratio.txt’ b) Output file ‘stringer.bdf’

The tool was used in the panel design stage of the composite wing in Chapter 5 and Chapter 6 and checked with ESDU 03001 [163] with a practical layup the difference between global and local buckling is less than 15%. This is an easy, reliable and optimal design tool for composite stringer stiffened panels.

4.4 Conclusion and Discussion

This chapter investigated an optimal design method for composite stringer stiffened panels with practical design constraints and considerations. The investigation started from optimal design of metallic stringer stiffened panel design method developed by Emero. Case studies were carried out and validated with ESDU package and Patran/Nastran FE commercial package. The results show that Emero's optimal design method developed from single stringer-skin section with elastic boundary can be further expended to multi-stringer stiffened panels. The results also show the increase of stringer number the buckling stress estimated through ESDU packages and Patran/Nastran converges to a constant value when the stringer number is over 15. It was verified that Emero's design method gives optimal design of metallic stringer stiffened panels.

Though Emero's method gives optimal metallic design results, it ignores realistic considerations so Niu's practical design ratios were introduced along with Emero's method. As case study shows the efficiencies of design with Niu's design ratios were comparatively at least 25% less efficient than the efficiencies of Emero's optimal design. A combined optimal design method was developed and verified with three load cases covering a practical load range indicated the method is able to give optimal design method with in all the load range with less than 3% error comparing with FE results and less than 7% difference between global buckling stress and local buckling stress of the panel.

By comparing the buckling stress of a composite flat plate and the buckling stress of an isotropic flat using the member modulus of the composite layup as the elastic modulus, the result shows the difference between buckling stresses was about 8%. By replacing corresponding elastic modulus in the optimal design method, the method can be applied to composite stringer stiffened panel design. Different design were estimated at different loads and orientation ply portions show that for composite IM7/8552 I section stringer stiffened panels with a practical symmetric layup, ±45˚ ply portion from 35% to 75% within the practical load range, optimal design method provides an optimal design with calculated buckling stress less than 10% error with Nastran estimation and buckling stress difference between global and local buckling is less than 15%.

If compare buckling stresses of optimal design of aluminium stringer stiffened panel given in Table 4.5 and those of different ply orientation portion composite stringer stiffened panels at a distributed load of 2850 N/mm in Table 4.13, the results are shown in Figure 4.23.

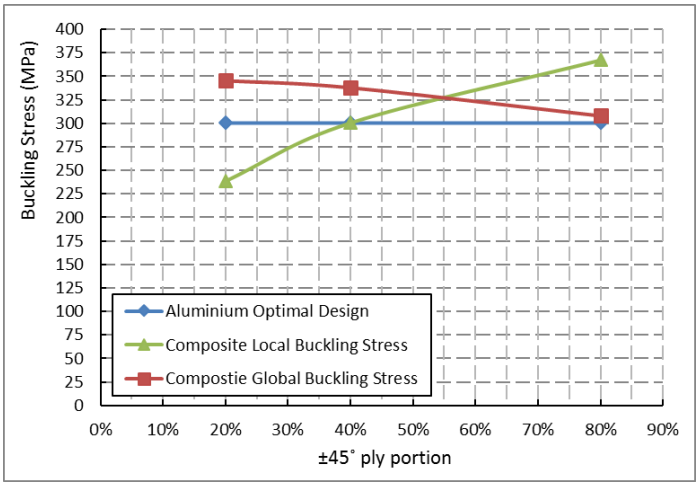

Figure 4.23 Buckling stress of aluminium and composite stiffened panel at N_x= 2850 N/mm

From Figure 4.23, it shows if ±45˚ ply portion less than 40% or more than 80% the buckling stress of aluminium stringer stiffened panel is higher than composite stringer stiffened panels but the weight of aluminium panel is 1.85 times of composite stringer stiffened panel. In the rest of the region the buckling stress of composite panel is less than 10% higher than that of aluminium panels. It shows composite stringer stiffened panel is only benefit from its low density. In the low ±45˚ ply portion range, composite stringer stiffened panel tends to buckle in a global mode and in the high ±45˚ ply portion range, the composite stringer stiffened panels fall into local buckling.

The composite optimal design method for stringer stiffened panel was applied in the initial wing panel design in the next chapter.

5 Optimization of a Composite Wing with Multi Constraints

Minimum weight design has always been one of the main challenging targets in aircraft design. For this reason, composite materials are introduced to aviation industry not only because of their high specific strength and stiffness but also the feasibility of laminate layup tailoring for engineers to achieve optimal design and desirable aeroelastic effects. Necessary directional stiffness can be achieved by optimizing the fibre orientations at minimum weight penalty [164]. To make a full use of the potential, many optimization methods have been developed and applied to composite structures such as ant colony algorithm [160] and genetic algorithm (GA) [165]. Some optimization methods have been reviewed by Ghiasi et al. [166] in the cases of constant stiffness design and variable stiffness design [167].

Aeroelastic stability is another important area which makes use of the directional stiffness properties of laminated composites. The divergent speed of a forward swept wing can be increased by aeroelastic tailoring, i.e. optimizing the laminate layup [168, 169]. The influence of unsymmetrical laminate layup and stiffness coupling on the aeroelastic behaviour of a composite wing was studied by Lottali [170] amongst others. Further study was carried out on the effect of elastic tailoring and warping restraint on the flutter instability and dynamic response of composite aircraft wings by Qin et al. [171]. In previous research, both gradient-based deterministic optimization method and GA were applied and results were compared in aeroelastic tailoring of composite wing structures [172, 173].

When compared with the above simplified wing models in previous research work [172-174], a high fidelity FE structure model with a large number of design

variables will no-doubt lead to more time consuming optimization process [175]. In the current study, a large aircraft composite wing with morphing leading edge subject to multi constraints is taken up as an example. Aeroelastic and geometric nonlinearity effect on the load distribution and analysis of high aspect ratio wings has been considered. An external gradient-based optimization code [176] as optimizer was integrated with Nastran as structure FE model solver [177]. A pre-processor was setup to group the ply thickness of the same fibre orientation as independent design variable. This reduces the total number of design variables. A post-processor was also setup to tailor the ply thickness to the standard manufacture figure. In this particular case, the composite wing upper surface weight was reduced by 19.84% after the optimization process.

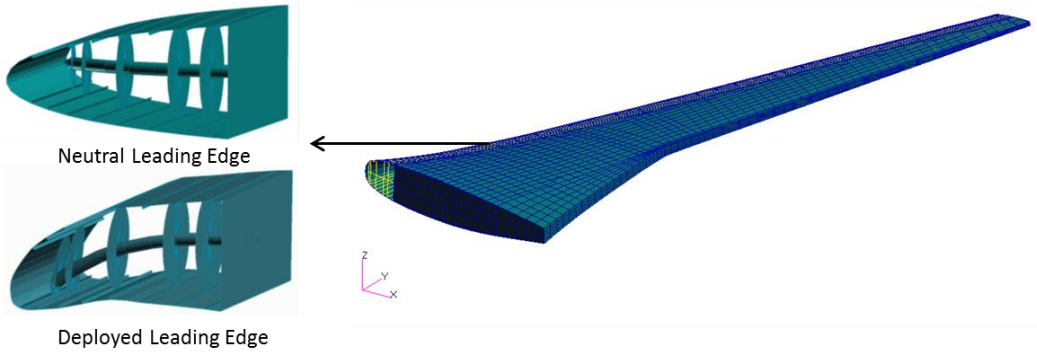

Figure 5.1 Composite wing with morphing leading edge

In this chapter a minimum weight optimization process of a composite wing with morphing leading edge [178] subject to strength, buckling and aeroelastic stability constraints is investigated. Based on the wing geometry and aerodynamic loading, an initial design of the wing structure was conducted. Static aeroelastic analysis was carried out to determine loading during cruise. Multi-constraints optimization was performed by using a gradient-determined optimizer [176] and MSC Nastran as a structural FE modelling and analysis solver. In the static aeroelastic analysis, the wing tip displacement and twist angle along the span are extracted which representing bending and torsional stiffness. By comparing these result, the bending and torsional stiffness contribution of a morphing leading edge (LE) to the entire wing are assessed

and compared with a conventional leading edge. The results show that the stiffness for the morphing LE in neutral position and deployed position has almost the same stiffness and the difference is negligible. The bending and torsional stiffness of a morphing leading edge are slightly lower than that of a conventional leading edge. In the optimization process, the wing structure is divided into ten sections along the span. During the pre-processing to deal with the skin laminate layup, the ply thickness of the same fibre orientation was grouped in one independent design variable. This result in the total design variables in each wing section reduced to the number of specified fibre orientations of the laminate. A post-processing was carried out to tailor the ply thickness to the standard figure. In this case study, weight of the upper surface of the composite wing was reduced by 19.84% after the optimization.

5.1 The Wing Model and Analysis Methods

5.1.1 Technical Data for the Composite Wing

The composite wing as illustrated in Figure 5.2 is designed for a commercial airliner with 200-seats equipped with smart high lift devices [178]. Some technical data used in the aircraft design is listed in Table 5.1. Spanwise wing aerodynamic load at the cruise condition was calculated by CFD method shown in Figure 5.3. In the initial design stage, the aerodynamic load results and ultimate load factor of 3.75 are taken along with structure weight and fuel weight. A two-spar configuration is taken for the initial design of the composite wing. The front spar is located at 13.1% chord at root and 37% at wing tip; the rear spar is at 60% chord from root to kink and 75% at tip. The wing upper and lower skin panels are made of carbon epoxy IM7/8552 with properties shown in Table 5.2. The front spar and rear spar are made of aluminium and properties are made of aluminium with young’s modulus of 7.2E4 MPa and Poisson’s ratio 0.3.

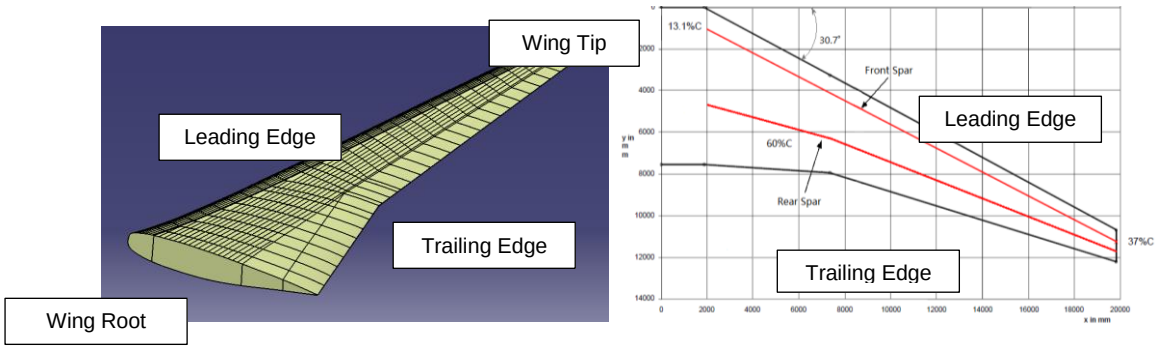

Figure 5.2 Platform and geometry of the wing example

Table 5.1 Some technical data of the aircraft design

Description	Values
Wing span, m	39.6
Fuselage length, m	35.57
Maximum take-off mass, kg	110000
Lift Coefficient (C_L)	0.5
Design cruise Mach	0.8
Cruise altitude, m	9450
Design mission range, km	5556

Table 5.2 Material properties (carbon /Epoxy composite, IM7/8552)

Description	Values
Longiudinal Young's Modulus, GPa	164
Transverse Young's Modulus, GPa	12
Shear Modulus, GPa	5.31
Poison's Ratio	0.32
Longitudinal Tensile Strength, MPa	2724
Longitudinal Compressive strength, MPa	1690
Transverse Tensile Strength, MPa	111
Transverse Compressive Strength, MPa	246
Shear Strength, MPa	120
Density, kg/m^3	1570
Ply thickness, mm	0.125

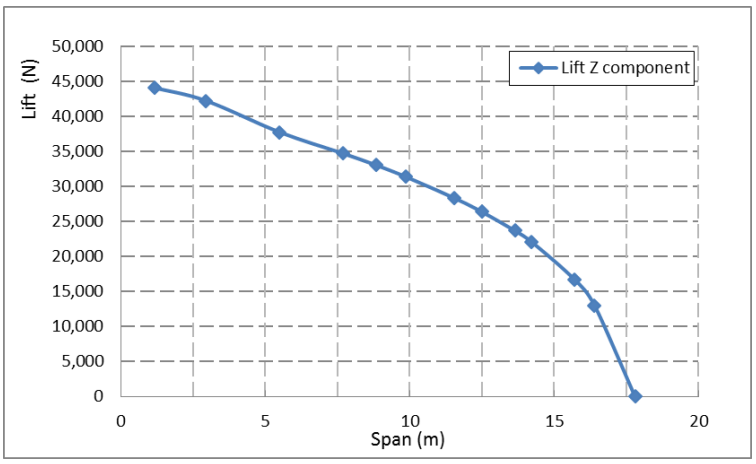

Figure 5.3 Wing spanwise aerodynamic load

The aerodynamic load is shown in Figure 5.3 and the structure and fuel mass distribution estimation is displayed in Figure 5.4. The ultimate distributed load is given in Figure 4.2. Ten spanwise design sections with independent design variable are shown in Figure 5.5.

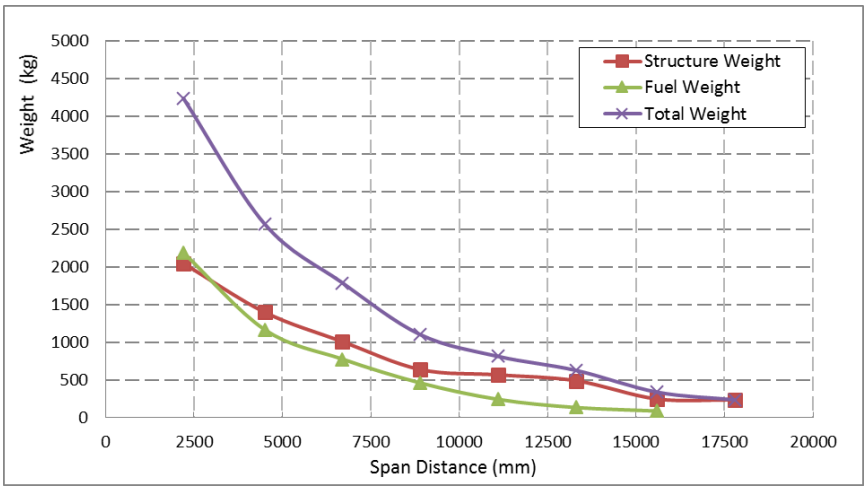

Figure 5.4 Structure and fuel mass distribution

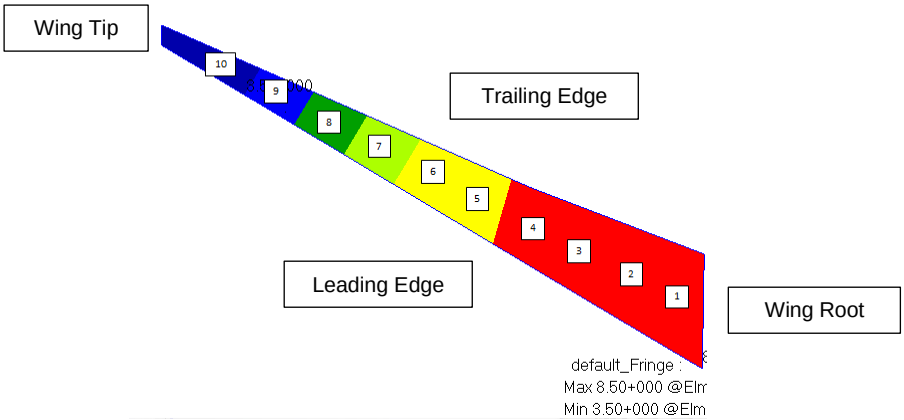

Figure 5.5 Spanwise design sections

5.1.2 Initial Panel Design Subject to Buckling and Strain

The composite wing skin panels were designed subject to buckling and strain requirements for each design section. I section stringers and T section stringers were used for wing upper and lower skin panels respectively. Practical optimal design method for composite stringer stiffened panel subject to buckling introduced in Chapter 4 was applied for initial panel design and strain limit is 4000$\mu\varepsilon$. The spanwise distributed load is given in Figure 4.2 and the layup of the composite laminate is symmetric with a stacking sequence of $n[45/0/0/-45/90]_s$. For upper wing panels, they are designed subject to buckling and strain limit is applied to lower wing skin panels.

The initial practical stringer stiffened panel design ratios are listed in Table 5.3 and the composite skin thicknesses of initial panel design results are given in Table 5.4. The front spar, rear spar, and ribs are made of aluminium designed to against buckling under shear load and spar thicknesses are given in Figure 5.6.

Table 5.3 Practical design ratios for initial design

$\frac{b_a}{t_a}$	$\frac{b_w}{t_w}$	$\frac{b_f}{t_f}$	$\frac{A_{St}}{A_{Sk}}$	$\frac{b_f}{b_w}$

7.2	18	7.2	0.5	0.4

Table 5.4 Initial panel design results

Upper Skin Panel Skin Thickness (mm)				
Section 1	Section 2	Section 3	Section 4	Section 5
6.75	7.5	7.5	7.5	7.25
Section 6	Section 7	Section 8	Section 9	Section 10
7	6.5	6	4.75	3.5
Lower Skin Panel Skin Thickness (mm)				
Section 1	Section 2	Section 3	Section 4	Section 5
5.75	8	8	9	8.75
Section 6	Section 7	Section 8	Section 9	Section 10
8	6	3.5	3.5	3.5

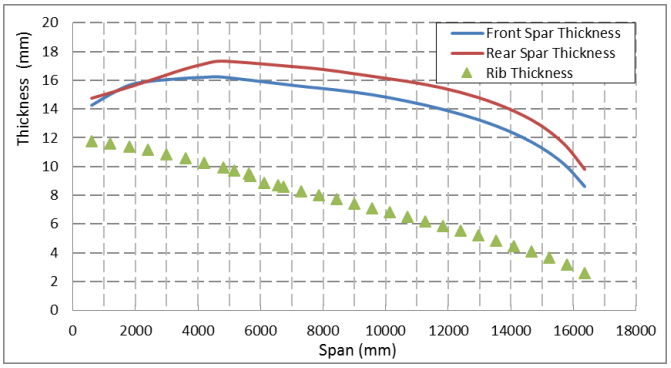

Figure 5.6 Front spar and rear spar thickness

5.1.3 Initial Design FE model and Results

Based on the initial design results in the last section, finite element model was set up. Between ribs there are three spanwise elements and one chord wise element between stingers. Beam elements are used to model spar caps and stringers. Upper and lower skins, ribs, spars are modelled with shell elements. MPCs are applied to connect stringers to skins. Different laminates materials are applied for each design section according to the initial panel design results. Aluminium with Young's modulus of 7.20E4 MPa is applied on front spar, rear spar, and ribs. The ultimate aerodynamic load is applied at 25% of the chord

(aerodynamic centre) at each design section ribs. The wing root is clamped. The FE model is given in Figure 5.7.

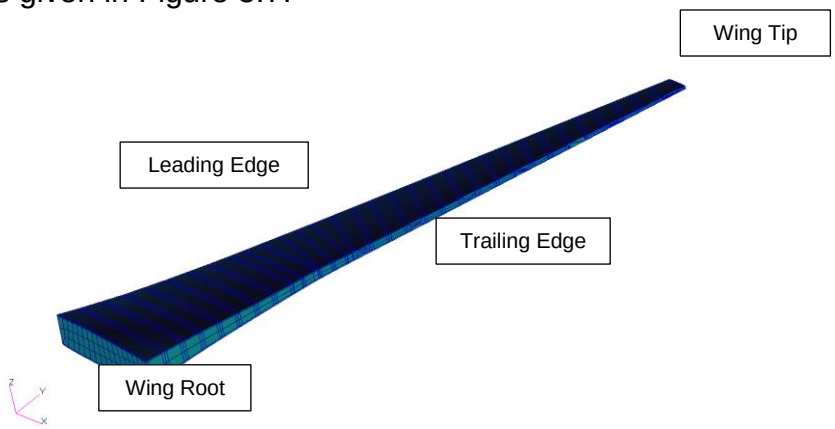

Figure 5.7 Composite wing FE model

In structure analysis, the maximum strain of the laminate under damage tolerance consideration is limited to 4000 $\mu\varepsilon$ and the expression is given as

$$\begin{Bmatrix} \varepsilon_x \\ \varepsilon_y \\ \varepsilon_{xy} \end{Bmatrix} = \begin{Bmatrix} \varepsilon_x^o \\ \varepsilon_y^o \\ \varepsilon_{xy}^o \end{Bmatrix} - z \begin{Bmatrix} k_x \\ k_y \\ k_{xy} \end{Bmatrix} \quad \textbf{(5.1)}$$

where ε_x^o, ε_y^o, ε_{xy}^o represent the strain in the mid-plane of a laminate; k_x, k_y, k_{xy} are the laminate curvature; {ε} is the total strain at the layer in z-coordinate measured from the mid-plane. For all strain plots, the blue regions are in compression and the red regions are in tension. For all failure index plots, high value regions are in red and low value regions are in blue. The strain is plot in Figure 5.8 and it shows the maximum strain is 3980 $\mu\varepsilon$ and 3890 $\mu\varepsilon$ for upper and lower surface at wing root section respectively.

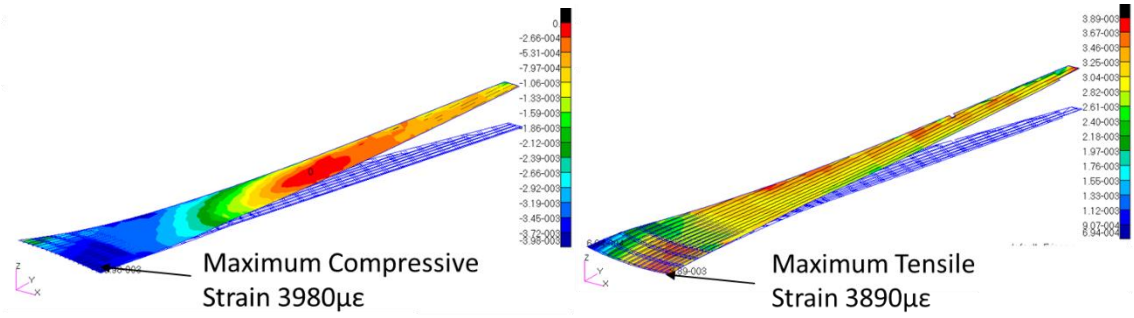

a) Upper surface strain plot b) Lower surface strain plot

Figure 5.8 Strain results of initial design

The buckling analysis was processed for the entire wing to check panel and wing composite stability. The first bucking mode is show in Figure 5.9 at wing tip panel between rib 27 and rib 28 with a buckling load factor of 1.17 which indicates current design can sustain 1.17 times ultimate load applied.

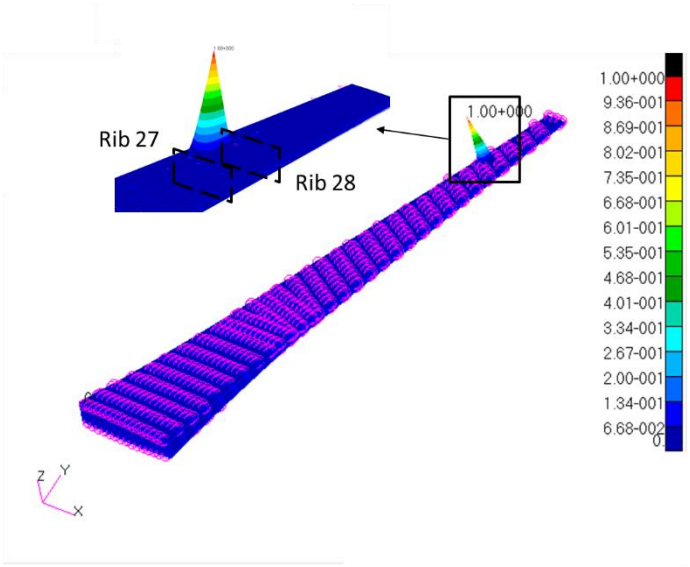

Figure 5.9 First buckling mode (local buckling)

The FEA results show that initial optimal panel design satisfies strain and stability requirements.

5.2 Static Aeroelasticity Analysis and Updated FE Model Considering Load Shift

5.2.1 Static Analysis

The aim of static aeroelastic analysis is to determine the final load distribution considering aeroelasticity at cruise condition which should be applied to the wing FE model for optimization. Meanwhile the stiffness of a conventional

leading edge and the morphing leading edge designed by Morishima et al. [83] were compared. The conventional leading edge is modelled by replacing the eccentuator beam with a rib which has the same material properties and weight. The static aeroelastic analysis flow chart is given in Figure 5.10. The initial load is given in Figure 5.3. Iterations started from initial angle of attack (1.88˚) given by commercial CFD code ANSYS CFX analysis at cruise condition, based on local lift coefficients in Table 5.5 calculated from CFX results, local angle of attack calculated from elastic twist, and initial geometry twist, aerodynamic forces of 13 spanwise wing segments were calculated and applied to the FE model at 25% of the chord of each load applied segment section rib [179]. By calculating local aerodynamic forces and adjusting wing angle of attack, total lift after twist was adjusted to meet the total cruise lift requirement.

Table 5.5 Local spanwise lift coefficient

Initial Wing Angle of Attack (˚)		1.88		
Entire Wing C_L		0.5		
Entre Wing C_L Slop		0.1108		
Entire Wing C_{L0}		0.2917		
Local AoA ID	Span Location (m)	Initial C_L	C_L Slop	C_{L0}
1	1.2	1.033	0.09391	0.39322
2	2.4	-0.002	0.10341	0.518
3	3.6	-1.124	0.11537	0.68397
4	4.8	-2.159	0.12926	0.87766
5	5.63	-2.835	0.14008	1.03164
6	7.03	-2.974	0.14711	1.08377
7	8.71	-3.241	0.15421	1.15947
8	10.33	-3.405	0.1607	1.2232
9	11.94	-3.493	0.1673	1.28085
10	13.55	-3.607	0.17124	1.3255
11	15.16	-3.759	0.16129	1.26778
12	16.77	-3.992	0.1054	0.84423
13	17.82	-4	0.08091	0.64415

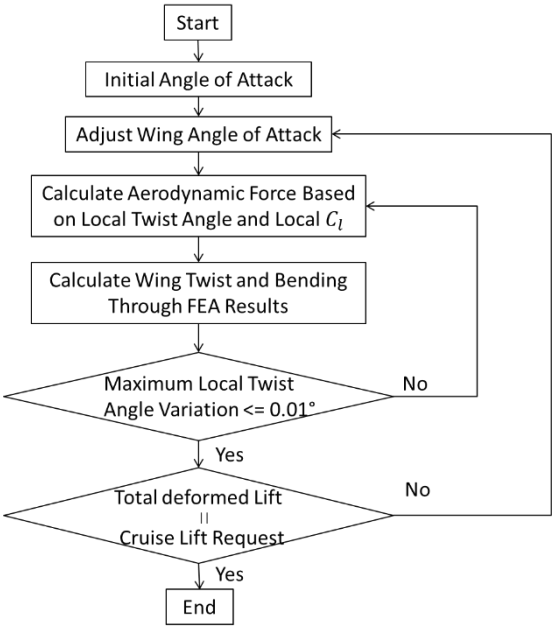

Figure 5.10 Flow chart of static aeroelastic analysis

(a)

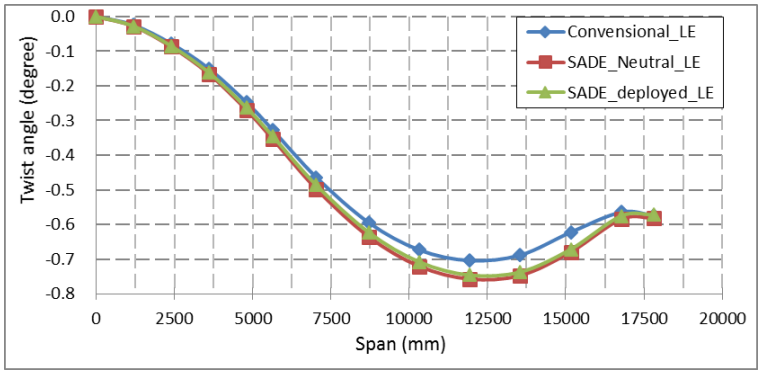

(b)

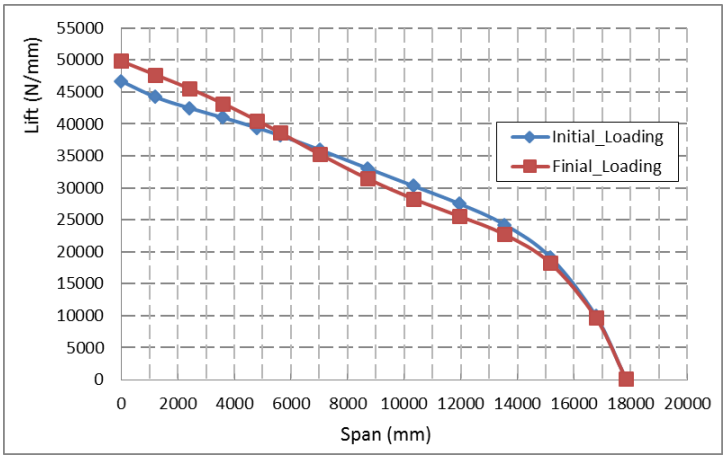

Figure 5.11 Static aeroelastic analysis results

a) Spanwise twist angle

b) Resulting aerodynamic load distribution

Spanwise free stream direction twist angle variation is plot in Figure 5.11 a) show that negative twist angle was generated due to the coupling of bending and twist from the deformation of the composite wing. The static aeroelastic analysis results show that the twist angle varies from root to tip where the tip twist angle is -0.58° and the minimum twist angle is -0.76° located at 3/4 of the span as displayed in Figure 5.11 a). The magnitude of the negative twist decreases to the wing tip due to less bending deformation in the region against pitching up moment generated by the aerodynamic forces.

As a consequence of negative twist angle, outboard local aerodynamic forces decreased compared with initial loads. To compensate this aeroelastic negative effect, the angle of attack at wing root was increased from 1.88° to 2.33° to meet the total lift demand at cruise. It is noted that the spanwise load distribution is shift from outboard to inboard wing as displayed in Figure 5.11 b) comparing with initial lift distribution. This reduces the load bending moment at the wing root. The finial aerodynamic load with ultimate load factor was applied to the wing structure for further analysis and optimization.

By comparing the twist angle results of conventional leading and morphing leading edge in Figure 5.11 a), it shows that the maximum negative twist angles locate at the same location for both models. The traditional LE provides a little greater bending and torsional stiffness to the entire wing than morphing leading edge. It indicates the morphing leading edge is more flexible than a conventional design but within a maximum twist angle difference around 8%. The twist angle results of a neutral leading edge and a deployed leading edge were close to each other and can be concluded that the stiffness for this morphing leading edge at two working conditions had almost the same torsional stiffness contribution to the entire wing.

Comparison of the stiffness was also made between the morphed LE and that in neutral position under the same initial loading condition. The twist angle curves of these two conditions and tip displacement have negligible difference.

To study the stiffness contribution of the morphing leading edge to the entire wing, a unit twist and bending moment were applied at the wing tip section of the wing box only model and the wing box model equipped with morphing leading edge. The bending stiffness was assessed as wing tip displacement and the wing twist angle was measured and used to compare the twist stiffness. The results showed that the contribution of the morphing leading edge was less than 5% so that the optimization was applied only on the wing box model.

5.2.2 Strength Analysis with Updated Loading Results

The strength of the wing is rechecked after aeroelasticity analysis to validate the effect of the lift shift. The strain of the composite is evaluated and laminate failure index based on Tsai-Wu criterion [180] is used to assess the structure strength.

$$f_1\sigma_1 + f_2\sigma_2 + f_{11}\sigma_1^2 + f_{22}\sigma_2^2 + f_{66}\sigma_6^2 + 2f_{12}\sigma_1\sigma_2 < 1 \quad \textbf{(5.2)}$$

where $f_1 = 1/F_{1t} - 1/F_{1c}$, $f_{11} = 1/(F_{1t}F_{1c})$; $f_2 = 1/F_{2t} - 1/F_{2c}$, $f_{22} = 1/(F_{2t}F_{2c})$; $f_{66} = 1/F_6^2$, $f_{12} = G/\sqrt{F_{1t}F_{1c}F_{2t}F_{2c}}$; and F_{1t}, F_{1c}, F_{2t}, F_{2c} represents the lamina tensile and compressive strength in longitudinal direction-1 and in transverse direction-2 respectively; F6 is the shear strength and a factor G = -0.5.

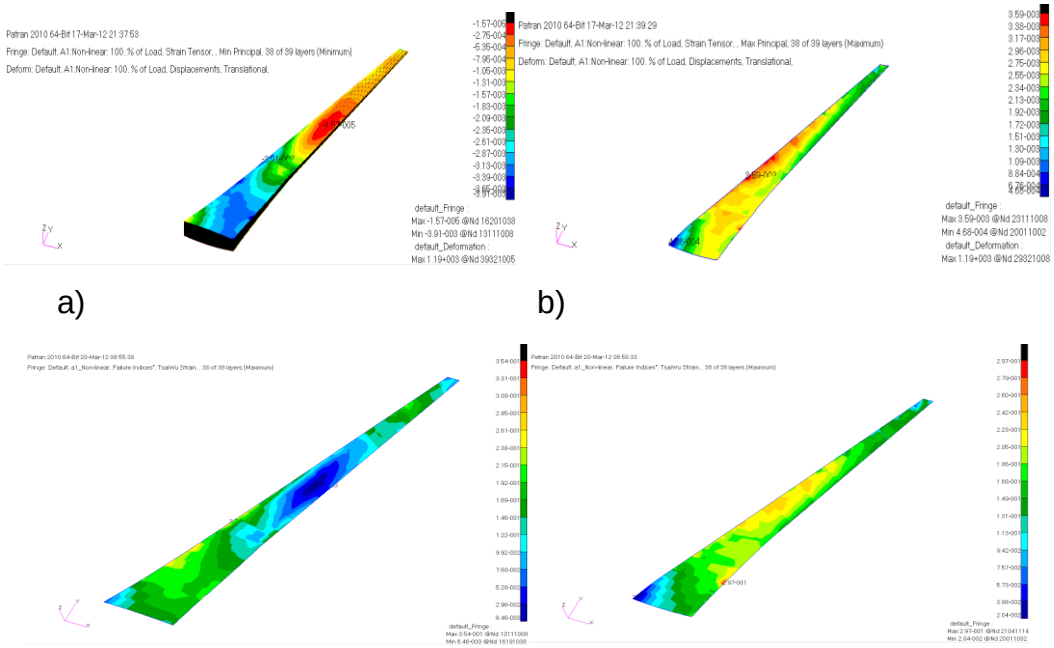

a) b)

c) d)

Figure 5.12 Wing strain and failure index results:

a) Upper surface Strain (ε) b) Lower Surface Strain (ε)

c) Upper surface Failure Index d) Lower surface Failure Index

The strain and failure index of upper and lower surfaces are plot in Figure 5.12. From Nastran FE results, the maximum strain under the loading is 3900$\mu\varepsilon$ occurring at middle span of the upper skin as shown in Figure 5.12 a). For the lower surface the maximum strain is 3500$\mu\varepsilon$ strain located around the mid-span as shown in Figure 5.12 b). The failure indexes for upper and lower skins are 0.35 and 0.3 respectively located at the same region as the maximum strain.

5.2.3 Flutter Analysis

In the aeroelastic analysis, Doublet-Lattice lifting surface theory is applied to calculate unsteady aerodynamic force. The wing aerodynamic model is divided into inner wing and outer wing with planar trapezoidal segments with the sides

parallel to the flow direction. In the inner wing section a higher mesh density was used to consider large pressure gradient and downwash discontinuity. For inner wing 100 panels were created and outer wing having 100 panels.

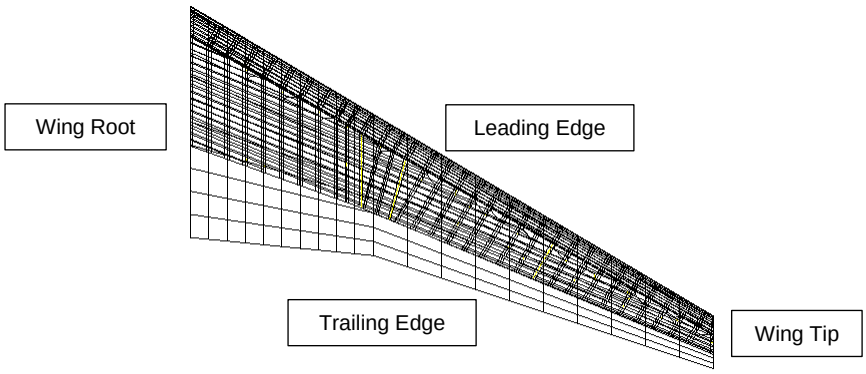

Figure 5.13 Structure mesh and aerodynamic mesh

Structure mesh and aerodynamic grids are coupled through a surface spline for aeroelastic analysis displayed in Figure 5.13. The basic equation for flutter analysis by the P-K method can be described as follows [93].

$$\left[-M_{hh}P^2 + \left(B_{hh} - \frac{0.25\rho cV Q_{hh}^I(m,k)}{k}\right)P + \left(k_{hh} - \frac{1}{2}\rho V^2 Q_{hh}^R(m,k)\right)\right]\{u_h\} \quad \textbf{(5.3)}$$

$$P = \gamma k + ik$$

where M_{hh}, B_{hh}, and K_{hh} are the modal mass, damping, and stiffness matrix respectively; m is Mach number; k is reduced frequency; u_h is the modal amplitude vector, sometimes called modal participation factors. Q_{hh}^R and Q_{hh}^I are the real and imaginary parts of Q_{hh}. The parameter γ is the transient decay rate coefficient which depends on the amplitude of successive cycles. By giving a set of initial reduced frequencies and interactions by updating k and γ solutions, the results will converge and the flutter speed can be determined.

In flutter analysis, the first bending modes and the first twist modes are considered as shown in Figure 5.14 the first 3 bending modes are at 3.94 Hz, 11.68 Hz, and 23.16 Hz and the frequency of first torsion mode is 25.26 Hz.

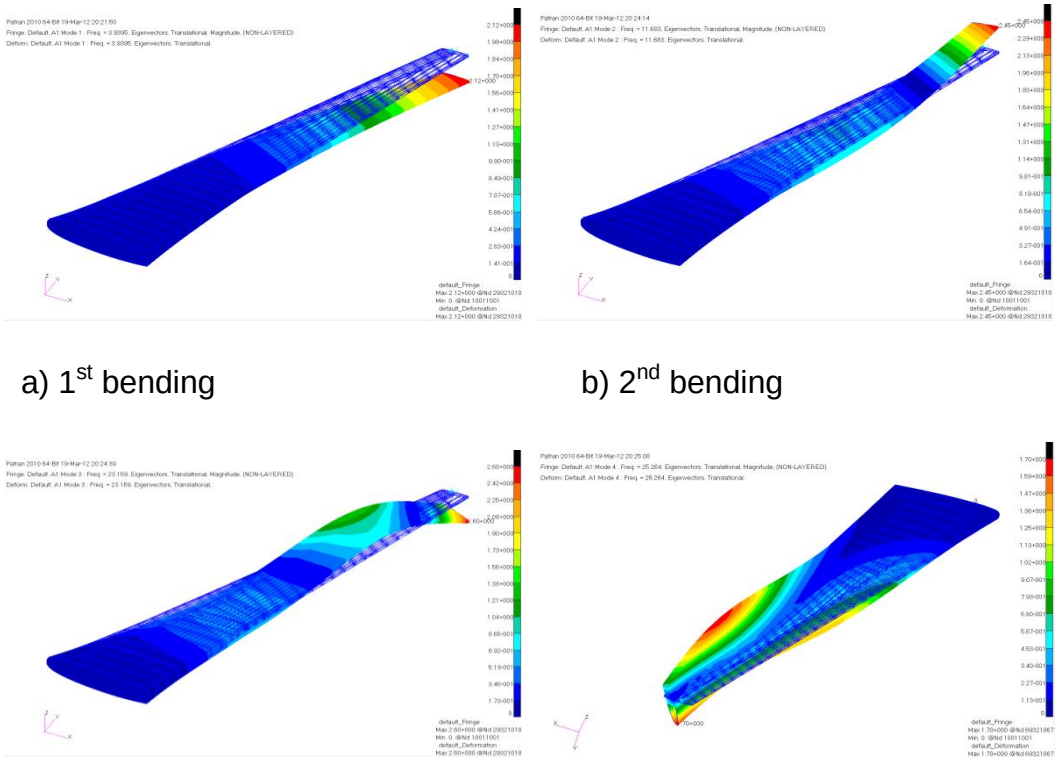

a) 1st bending b) 2nd bending

c) 3rd bending d) 1st torsion

Figure 5.14 First four mode shapes

The flutter analysis results are obtained using P-K method and the results are plot in Figure 5.15. V-g and V-f plotted are used to illustrate the results. The result shows that the flutter speed is around 780 m/s for the first bending mode.

a) 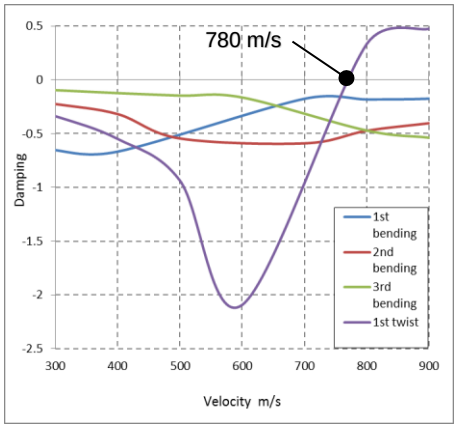

b) 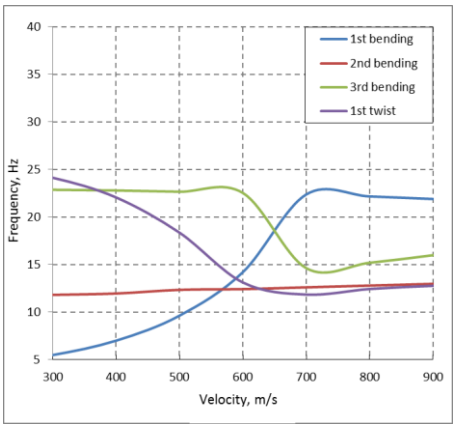

Figure 5.15 Flutter results of initial wing design: (a) V-g plot (b) V-f plot

The initial design analysis results shows that the strain level was kept relatively low in most wing sections. The flutter speed is much higher than the design requirement. All these indicate that there are some optimization potential for further structure weight saving.

5.3 Optimization of the Wing Structure

The optimization is to achieve a minimum weight within multi design constraints. A Gradient-based determination method [176] is used as optimizer along with MSC Nastran package applied as a structure model solver to get constraints response and calculate objective function for this multi constraint optimization problem. In this section, the optimization was applied to the upper surface of the wing box as an example.

5.3.1 Pre-Process for Optimization

In optimization, individual ply thickness and fibre orientation can be taken as independent design variables. However this would result in a considerable number of design variables and slow optimization process. To reduce the

design variables, the ply thickness of the same fibre orientation was summed and grouped as one design variable for each wing skin section. By keeping the initial laminate stacking sequence and taking layup symmetry into account, the design variables can be further reduced. In the current case, there are four different thicknesses for the ply orientation of +45, -45, 90 and 0 degree. The resulting design variables for the 10 sections of upper skin panels are reduced to 30.

5.3.2 Optimization for Minimum Weight

The objective for this optimization is to minimize the structure weight of the upper surface of the composite wing box. The design variables as discussed in the former section were the ply thickness of the same fibre orientation in the laminate. Multi constraints are applied to this optimization including the maximum strain limited to no more than 4000 $\mu\varepsilon$ and the critical buckling load factor great than 1.0. The lower boundary of flutter speed is set as 1.15V_D [181] by considering airworthiness. The multi-constraint problem to achieve a minimum weight is as follow:

$$\begin{cases} MinW\ (X) \\ \varepsilon(X) \leq 4000\mu\varepsilon \\ BLF \geq 1.0 \\ V_f(X) \geq 1.15V_D \\ X = [t_1, t_2, \cdots t_n] \end{cases} \quad \textbf{(5.4)}$$

In the optimization, the total iteration number is 450 and the main computation time consumption is from Nastran Nonlinear solver 106. The optimization results show a reduction in upper surface of the wing weight from 625kg to 501kg which is 19.84% compare with the initial design as show in Figure 5.16. The maximum strain on the upper surface is 3980$\mu\varepsilon$ just under the constraint as shown in Figure 5.17. For lower surface, the maximum strain is increased from

the initial design to 3550$\mu\varepsilon$. It is also noted that the maximum strain is located at a slightly different position of the wing from the initial design. The improved strain distribution on each design section indicates a more even loading for better use of materials. After optimization, the results of maximum Failure Index increased to 0.414, buckling load factor reduced to 1.016 and optimized flutter speed of 633.5 m/s indicate that the optimized wing satisfies all the specified design requirements.

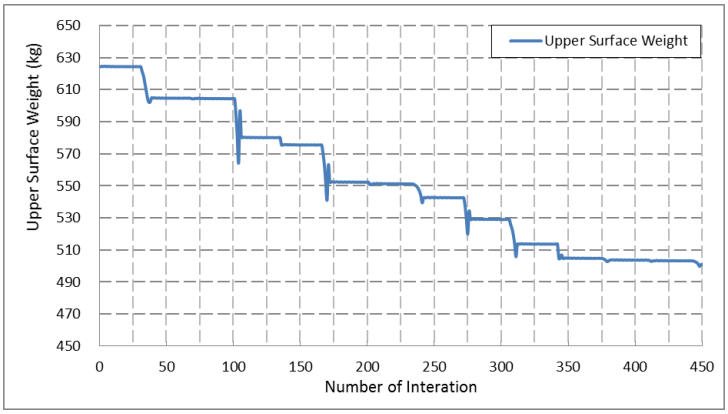

Figure 5.16 Weight reduction results of the optimization process

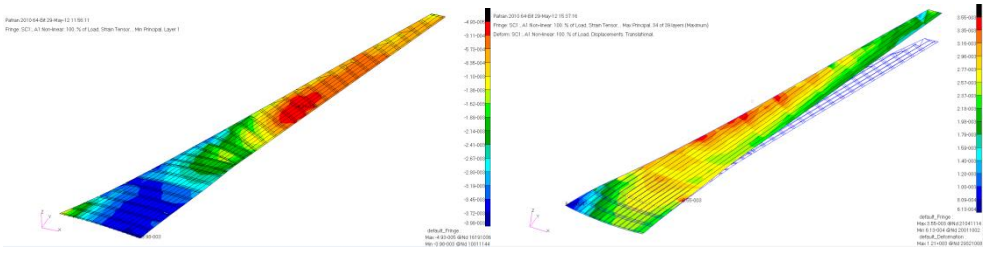

(a) Upper skin (b) Lower skin

Figure 5.17 Strain of the optimized wing under ultimate load

5.3.3 Post-Process of Optimization

The post processing is carried out to trim manually the individual ply thickness to meet practical design set in manufacture process. The total ply number for each fibre orientation type is scale to the closest integer number and times the

standard ply thickness 0.125mm. Then the laminate stacking sequence is rearranged according to the total ply numbers in the layup [(45/0/0/-45/90)n]s. The trimmed skin thickness and ply numbers of each ply type is given in Table 5.6.

Table 5.6 Layups after optimization post-process

Section ID	No. of 0˚ Ply (before trim)	No. of 45˚ Ply (before trim)	No. of 90˚ Ply (before trim)	Skin Thickness (mm)
1	28 (27)	12 (9)	4 (4)	5.5
2	24 (24)	20 (17)	4 (4)	6
3	28 (26)	28 (26)	4 (4)	7.5
4	24 (23)	28 (26)	4 (4)	7
5	20 (21)	20 (23)	4 (4)	5.5
6	12 (11)	20 (23)	4 (4)	4.5
7	8 (8)	20 (23)	4 (4)	4
8	8 (8)	12 (14)	4 (4)	3
9	16 (17)	16 (18)	4 (4)	4.5
10	8 (9)	12 (15)	4 (4)	3

The strength was performed again for the wing structure after the post process. Fig 10 shows the strain results after post process. The maximum strain after post process remains 3980$\mu\varepsilon$ although located at a slightly different location from before the post process.

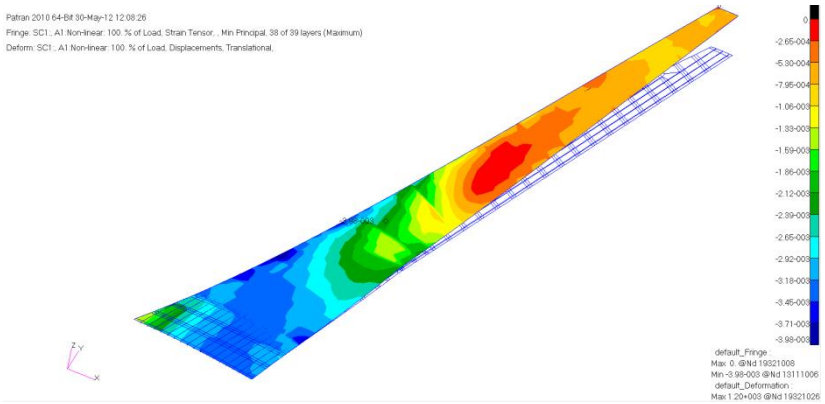

Figure 5.18 Strain of upper skin after post process of laminate layup

5.4 Conclusion

This chapter presents a case study on optimization of a composite wing with morphing leading edge with multi constraints. The initial design of upper and lower wing surface panels are based on the optimal composite stringer stiffened panel method developed in Chapter 4. FE wing model was then set up and strength was checked through non-linear geometry analysis. Static aeroelastic was carried out to find out final wing loading considering wing deformation. Initial model check shows maximum strain, failure index, buckling, and flutter speed met the design requirement. The stiffness of the morphing leading edge was studied, the results show that the deflection of the wing equipped with neutral positioned and deployed leading edges are close. Both leading edges have limited stiffness contribution to the entire wing.

Optimization was carried out with new spanwise lift distribution calculated in the static aeroelastic analysis. The objective is to achieve a minimum weight and strain, buckling, and flutter speed are taken as optimization constraints. The ply thickness of each ply orientation type in each design section was taken as individual design parameters. Optimization result shows that a 19.84% reduction in upper surface weight was achieved. Post-process was applied to calculate practical ply number based on total thickness of the ply type in each design section. After post-process, the strength was rechecked and still meet design requirement.

6 Optimal Design of a Passive Gust Alleviation Device for a Composite Wing

The chapter is aimed at optimizing a passive gust alleviation device (PGAD) mounted at the wing tip of the composite wing optimized in Chapter 5 which is taken as the baseline wing in this chapter for minimum gust response optimization. Compared with previous research work on various passive gust alleviation technologies investigated [182, 183] and similar types of sensorcraft [184-190], the PGAD investigated in this chapter is a potential option as an effective and optimal design. The concept of PGAD is illustrated in Figure 6.1 (a) which is a segment of the wing mounted at the wing tip where is the most efficient location to release bending moment at wing root mounted. The segment is connected to the rest of the wing with a torque spring as shown in Figure 6.1 a). By locating hinge location ahead of the aerodynamic centre of the section, PGAD can generate a nose down pitching moment to alleviate the aerodynamic force and reduce gust response in displacement and load. As a result of this wing tip negative twist, a nose down pitching moment is generated to the entire wing and reduces aerodynamic load during gust as shown in Figure 6.1 b). Also, the PGAD concept can be used to reduce the aerodynamic drag of the aircraft. This can be achieved by mounting the device section to the wing tip while keeping the associated loads from the higher bending moment small by creating a favourable, passive deformation of the surface.

The effectiveness of the PGAD depends upon three key design parameters (hinge shaft location, torque spring, and dimension of the device) and the wing dynamic behaviour. The baseline composite wing (not PGAD equipped) was tailored by optimizing the wing structure in Chapter 5. The torque spring stiffness and the location of the rotational shaft determine the twist angle of the device and the wing, measure of gust alleviation, and the responsive speed of PGAD. The dimension of the device scales the amount of gust response and

the flight performance during normal condition should also be considered. The area on the device in front of the axis is affected by the gust first and since this piece of area is ahead of the neutral axis, the device will try to rotate itself in a sense of nose-up within a very short period. After that, the device will then rotate in the opposite direction. In this chapter, the investigation focuses on optimization of hinge shaft location and torque spring stiffness for minimum gust response.

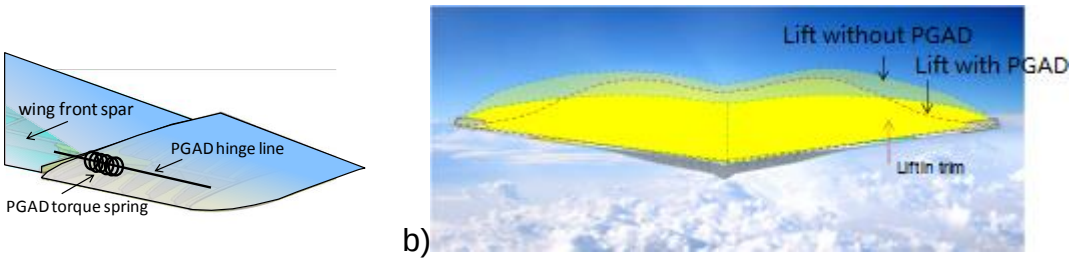

a) b)

Figure 6.1 PGAD concept and lift distribution

a) PGAD at wing tip

b) Lift distribution on a flying wing aircraft with and without PGAD

6.1 Baseline Wing Model and Simplified Beam Method

6.1.1 The Baseline Wing Structural Model

In the investigation of this chapter, the baseline wing model is the FE wing model optimized in Chapter 5. The basic geometry data and technical data of the wing are given in Figure 5.2 and Table 5.1. The properties of the composite ply material used for the composite wing stringer stiffened panels are given in Table 5.2. The wing structure made of spars, ribs and stringer reinforced skins was modelled by applying finite element (FE) commercial package Patran/Nastran. Optimal design method for composite stringer stiffed panels developed in Chapter 4 was applied and aerodynamic loading was updated considering static aeroelasticity effect. Optimization was then carried out to

obtain the baseline model for this investigation. Technical data of the optimized wing is given in Table 6.1. The layups of ten spanwise design sections after optimization post-processing are given in Table 5.6. The natural frequency of the first four modes of the optimized wing is given in Table 6.2 and relative displacement normalized mode shapes are given in Figure 6.2.

Table 6.1 Technical data of the wing after optimization

Maximum Strain με	Failure Index	Buckling Load Factor	Flutter Speed m/s
3980	0.44	1.016	633.5

Table 6.2 Nature frequencies of the first four modes

	Mode 1 1st Bending	Mode 2 2nd Bending	Mode 3 3rd Bending	Mode 4 1st Torsion
Frequency (Hz)	3.667	11.10	22.62	24.68

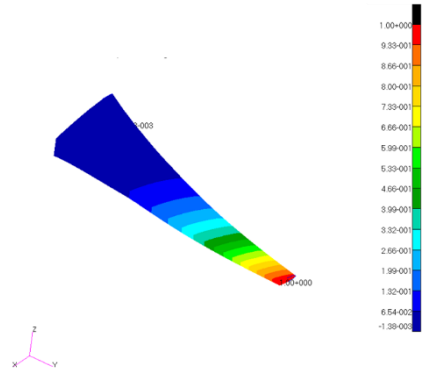

a) 1st Bending

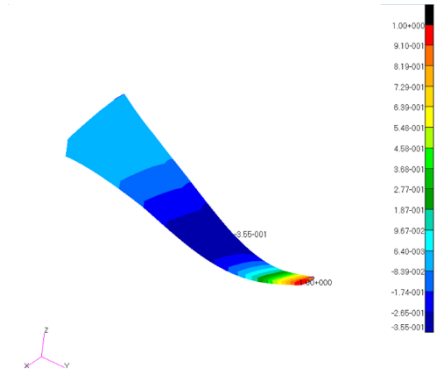

b) 2nd Bending

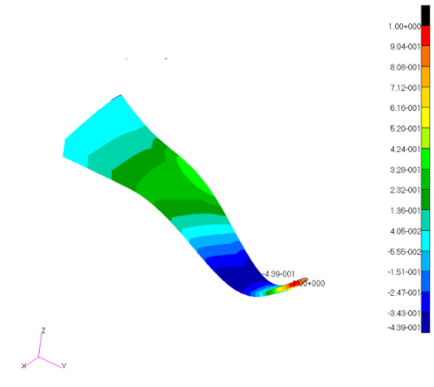

c) 3rd Bending

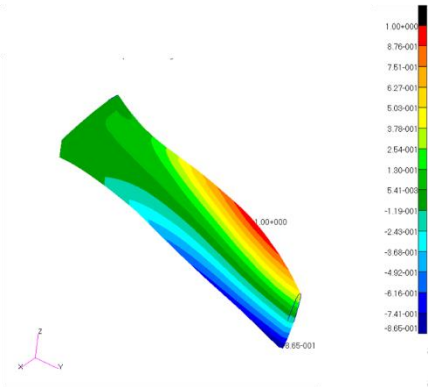

d) 1st Torsion

Figure 6.2 First few mode shapes of the optimized wing

The PGAD is applied at the wing tip by replacing a spanwise segment of 1 m as shown in Figure 6.3.

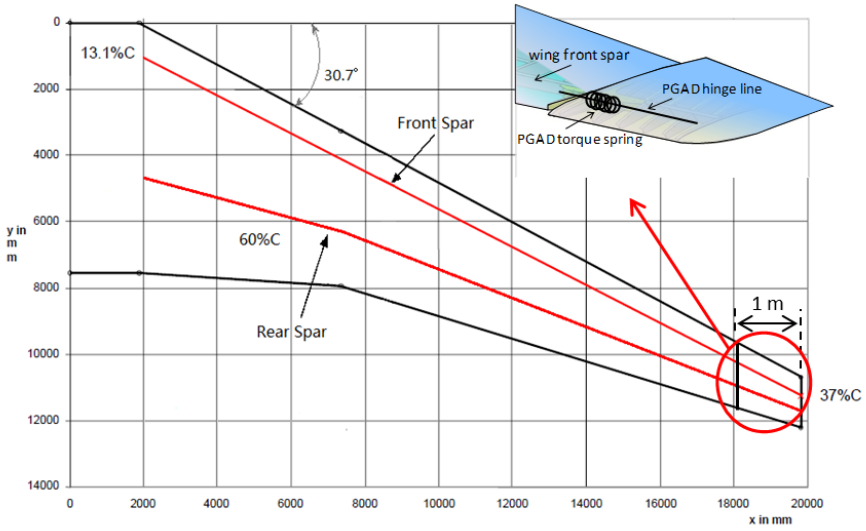

Figure 6.3 PGAD location on the wing

6.1.2 Simplified Wing Beam Model

6.1.2.1 Wing Simplified Method

A composite beam model is applied in the investigation to represent the optimized wing structural model. This thin-walled beam model is to evaluate the gust response of the wing equipped with PGAD regarding the aeroelastic coupling effects. The method developed by Armanios and Badir [191] and the dynamic stiffness method [192] used are described as below. In the composite wing box modelling process, the wing was divided into 20 spanwise segments and each segment was modelled as a uniform thin-walled double-cell box beam between the leading edge and rear spar. By assembling these box beams, the whole wing structure model can be obtained. Eq. (6.1) shows the relationship between the bending moment M_x, torque M_y and the transverse and twist deflections at the end of an anisotropic thin-walled closed-section beam.

$$M_y = C_{22}\emptyset' + C_{23}h''$$
$$M_x = C_{23}\emptyset' + C_{33}h'' \quad \textbf{(6.1)}$$

where C_{ij} representing the stiffness coefficients of each segment is calculated on the basis of its geometry, material properties, and integration along its cross sectional circumference

$$\begin{cases} C_{22} = \dfrac{A_e^2}{\oint(1/C(s))ds}, C_{23} = A_e\dfrac{\oint(B(s)/C(s))zds}{\oint(1/C(s))ds} \\ C_{33} = \oint\left[A(s) - \dfrac{B(s)^2}{C(s)}\right]z^2ds + \dfrac{[\oint(B(s)/C(s))zds]^2}{\oint(1/C(s))ds} \end{cases} \quad \textbf{(6.2)}$$

where A_e is the enclosed area of the cross section. A(s), B(s) and C(s) are given below.

$$A(s) = A_{11} - \frac{(A_{12})^2}{A_{22}},\ B(s) = 2\left[A_{16} - \frac{A_{12}A_{26}}{A_{22}}\right],\ C(s) = 4\left[A_{66} - \frac{(A_{26})^2}{A_{22}}\right] \quad \textbf{(6.3)}$$

The parameters A_{ij} in Eq. (6.3) are the coefficients of stiffness matrix (A) which is the stiffness of composite skin and spar webs of the closed-section beams. According to the force-deflection relationships in Eq. (6.1) and stiffness definition, the stiffness coefficients C_{33} , C_{22} and C_{23} actually represent the bending rigidity (EI), torsion rigidity (GJ), and bending-torsion coupling rigidity (CK) of the wing box beam. The model includes the bending stiffness contribution of the fourteen stringers to the wing box.

The dynamic stiffness matrix method [192] was subsequently applied in the dynamic analysis. In this method, the equations of motion for each of the thin-walled box beams are given in Eq. (6.4). The bending-torsion stiffness coupling was considered while the transverse shear deformation and warping effect are neglected.

$$EI \cdot h'''' + CK \cdot \emptyset''' + m \cdot \ddot{h} - m \cdot X_a \cdot \ddot{\emptyset} = 0 \quad \textbf{(6.4)}$$

$$GJ \cdot \emptyset'' + CK \cdot h''' + m \cdot X_a \cdot \ddot{h} - I_p \cdot \ddot{\emptyset} = 0 \quad \textbf{(6.5)}$$

where $h'''' = \partial^4 h/\partial y^4$, $\ddot{h} = \partial^2 h/\partial t^2$, $\emptyset'''' = \partial^3 h/\partial y^3$and $\ddot{\emptyset} = \partial^2 h/\partial t^2$. An exact solution for the displacement function $h(y)$ and $\emptyset(y)$ can be obtained. This exact solution of the displacements at both ends of the beam are used to create a dynamic stiffness matrix for a box beam. The dynamic stiffness matrix for the whole wing box structure is then obtained by assembling all the wing box beam stiffness matrices along the spanwise direction.

6.1.2.2 Wing Beam Model

The geometrical dimensions of 21 wing sections for 20 spanwise wing segments are obtained through CATIA model given in Figure 5.2 and 20 panel elements are used for each segment section shown in Figure 6.4 with 8 panel elements for upper and lower surfaces respectively. The bending and torsional stiffness of the leading edge, front spar, and rear spar are considered in the model. The bending and torsional stiffness of the trailing edge is not included.

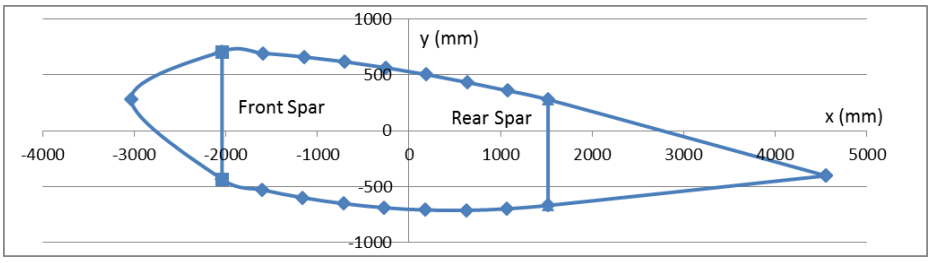

Figure 6.4 Segment section panel elements at wing root

The composite stringer stiffened panel dimensions are obtained from optimization results in Section 6.1.1. The section bending and torsional stiffness of wing skin and upper/lower stringers are calculated separately and the total section stiffness is the superposition of skin, stringer, and spar stiffness. The

mass of each segment is estimated based on the structural mass and fuel mass distribution plotted in Figure 5.4.

The neutral axis of the wing was assumed at 40% of the chord at each wing section and the coordinates of the neutral axis locations in the global coordinate system is given in the following Table 6.3 and Figure 6.5. The dihedral effect is not considered. The wing tip beam element between Node 20 and Node 21 is used for PGAD device segment with 1m spanwise length.

Table 6.3 Neutral axis location at each wing segment

Section ID	X (m)	Y(m)	Z(m)	Section ID	X(m)	Y(m)	Z(m)
1	3.04	0.00	-0.27	**2**	3.68	1.68	-0.13
3	3.90	2.24	-0.08	**4**	4.11	2.80	-0.03
5	4.33	3.36	0.01	**6**	4.54	3.92	0.06
7	4.76	4.48	0.11	**8**	4.97	5.04	0.16
9	5.19	5.60	0.21	**10**	5.67	6.57	0.29
11	6.15	7.55	0.38	**12**	6.63	8.52	0.46
13	7.11	9.49	0.55	**14**	7.59	10.46	0.64
15	8.07	11.44	0.72	**16**	8.55	12.41	0.81
17	9.03	13.38	0.89	**18**	9.51	14.35	0.98
19	9.99	15.33	1.07	**20**	10.47	16.30	1.15
21	10.91	17.19	1.23				

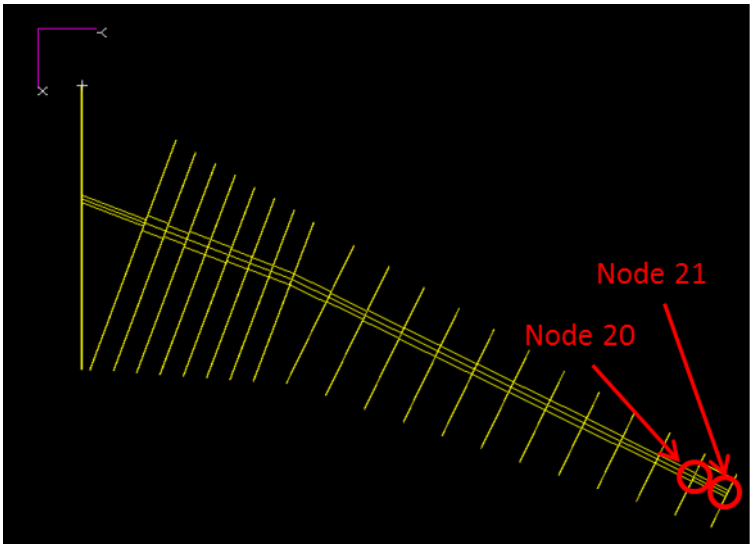

Figure 6.5 Simplified composite beam model

The natural frequency of the beam model was calculated using a FORTRAN program [193] and listed in Table 6.4.

Table 6.4 The frequencies of the first four modes of the wing beam model

	Mode 1 1st Bending	Mode 2 2nd Bending	Mode 3 3rd Bending	Mode 4 1st Torsion
Frequency (Hz)	3.640	11.365	24.594	42.3

The results shows the natural frequency of the first two modes of the beam wing model is close to baseline wing FE model within 2% deviation and for Mode 3 the difference is less than 10%. This shows the beam model has a good agreement with baseline model in dynamic behaviour and can be used for dynamic analysis instead of baseline model.

6.2 Gust Response Analysis

6.2.1 Gust Load Conditions and Critical Gust

Before determine gust load information for further gust analysis, critical gust load case should be determined. Two different flight conditions (cruise and landing conditions) and two weight cases (full fuel and empty fuel) are considered to determine the critical gust load case for further investigation. The critical gust load factor [181] is given by

$$n_{gust} = 1 + \frac{k_g \rho_0 U_{de} V_0 a_1}{2\frac{W}{S}} \tag{6.6}$$

ρ_0	Air density
V_0	Aircraft equivalent speed
U_{de}	Design gust speed
a_1	Wing lift curve slop
W	Aircraft weight
S	Wing section area

where

$$K_g = \frac{0.88\mu_g}{5.3 + \mu_g}$$

$$\mu_g = \frac{2\frac{W}{S}}{\rho C_{mean} a_1 g} \tag{6.7}$$

C_{mean}	Mean aerodynamic chord

The mean chord length for baseline wing is 4.18 m and wing C_L at cruise and landing are 0.5 and 1.6. The MAC number at cruise and landing conditions are 0.8 and 0.15 respectively. The altitude for cruise and landing are 31000 ft and 1000 ft. The air densities are 0.44 kg/m^3 and 1.19 kg/m^3 at cruise and landing altitudes calculated from Eq. (6.8).

$$\rho = \frac{pM}{RT}$$

$$p = p_0 \left(1 - \frac{Lh}{T_0}\right)^{\frac{gM}{RL}} \quad \textbf{(6.8)}$$

$$T = T_0 - Lh$$

h	Altitude
T_0	Sea level standard temperature
L	Temperature Lapse rate
p_0	Sea level standard pressure
R	Ideal gas constant
M	Molar mass of dry air

The design gust velocities at two flight condition altitudes are calculated at three gust gradient length at 9.14m, 52.3m, and 106.68m. The 9.14m and 106.68m are the lower and upper boundary of the gust length range and the 52.3 m is the gust length recommended by 12.5 times the mean chord of the wing. The design gust velocity are calculated through Eq. (2.30) and listed in Table 6.5.

Table 6.5 Design gust velocities at cruise and landing

Gust Gradient Length	9.14m	52.3m	106.68m
Gust frequency at cruise	13.12 Hz	2.29 Hz	1.12 Hz
U_{de} at cruise	5.89m	7.87m	8.86m
Gust frequency at landing	2.59 Hz	0.45 Hz	0.22 Hz
U_{de} at landing	9.08m	12.15m	13.68m

The gust load factor is calculated based on Eq. (6.6) for each case listed in Table 6.6.

Table 6.6 Gust load factor of each load case

	Cruise (full fuel)	Cruise (empty fuel)	Landing (full fuel)	Landing (empty fuel)
Gust Load Factor	1.49	1.61	1.07	1.08

From gust load factor results listed in Table 6.6 show that the critical gust load case is at cruise condition with empty fuel with a gust load factor of 1.61 and the gust information related to this gust load case is applied for further investigation.

6.2.2 Gust Response of Baseline Beam Wing Model

In this section, the gust response of the baseline wing is estimated at critical gust load case shown in Table 6.6 to determine critical gust gradient length. The dynamic stiffness matrix is a combination of stiffness and mass matrices of the beam and is frequency dependent. As this particular type of matrix results in a non-standard eigenvalue problem, the solution can be obtained by applying Wittrick-William algorithm [194]. The normal mode method was used to create the aeroelastic equation for a wing coupled with shelf excited unsteady aerodynamic forces, which is written in generalized coordinates as follows. The unsteady aerodynamic forces were calculated by using the classical Theodorsen theory [94, 195] and the strip theory in incompressible airflow.

$$\left[[K_D(\omega)] - \frac{1}{2}\rho V^2[AL]_R + i\omega[D] + i\frac{1}{2}\rho V^2[AL]_I\right]\{q\} = 0 \qquad \textbf{(6.9)}$$

By regarding gust load as external unsteady aerodynamic force, the aeroelastic response equation of the wing structure is written as

$$[M]\{\ddot{x}\} + [D]\{\dot{x}\} + [K]\{x\} = [AL_1]\{\ddot{x}\} + [AL_2]\{\dot{x}\} + [AL_3]\{x\} + \{AL_{ext}\} \qquad \textbf{(6.10)}$$

where [M], [D], [K] are the structural mass, damping, and stiffness matrices. $[AL_i]$ and $\{AL_{ext}\}$ represent the unsteady aerodynamic and external dynamic force matrices respectively. The gust velocity profile of a 1-cosine model is expressed as shown in Eq. (2.29). The [M], [D], [K] matrix are calculated through a FORTRAN based program [196].

The design gust speeds at each gust gradient length (U_{de}) are calculated in Table 6.5. The gust responses at three gust gradient length 9.14m, 52.3m, and

106.68m are calculated with corresponding gust frequency 13.12Hz, 2.29Hz, and 1.12Hz. It is noted that the gust frequency in this range covers the first two bending modes of the wing structure. This causes a concern of the wing structure, which is likely to be sensitive and have large response to gust load. The beam model created in section 6.1.2 is used for the baseline wing gust response calculation. The gust velocity according to the gradient length can be found in Table 6.5 at cruise condition with empty fuel. Structural damping of 3% of the structure stiffness is considered in the gust response calculation [197]. The flight speed at cruise condition (31000 ft) is 240m/s (M=0.8).

For the empty fuel cruise case, the gust response is measured as the wing tip displacement shown in Figure 6.6. From the results, it is noted that the maximum gust response is at the gust gradient length of 106.68m with a maximum tip displacement of 0.96m at a gust frequency of 1.12 Hz. This gust frequency is below the 1^{st} bending mode frequency. There are two main reasons for this result. Firstly, from Eq. (2.30) at the gust gradient length of 106.68m a higher gust velocity is achieved. Secondly, the flight speed for cruise condition is high result in high aerodynamic damping force and at a high gust frequency, the high equivalent angle of attach changes lead to a high damping force. The results without aerodynamic damping force are plotted in Figure 6.7. An equal gust velocity 8.864m/s is used for those cases. From Figure 6.7, the results show that without aerodynamic damping terms all the amplitudes of gust response at each gust gradient length is increased and maximum gust response gradient length is at 32.7m whose gust frequency matches 1^{st} bending mode frequency and oscillation took place at the end of the gust period. The gust frequency is 13.12Hz at 9.14m which is close to 2^{nd} bending mode frequency 11.10Hz the oscillation is also observed at the end of the gust load.

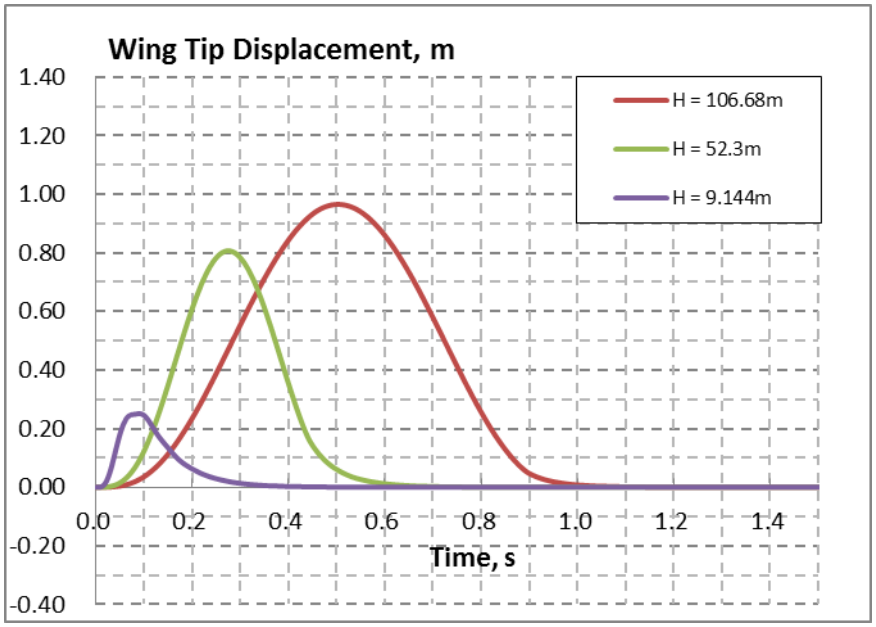

Figure 6.6 Wing tip displacement of varies gust gradient length

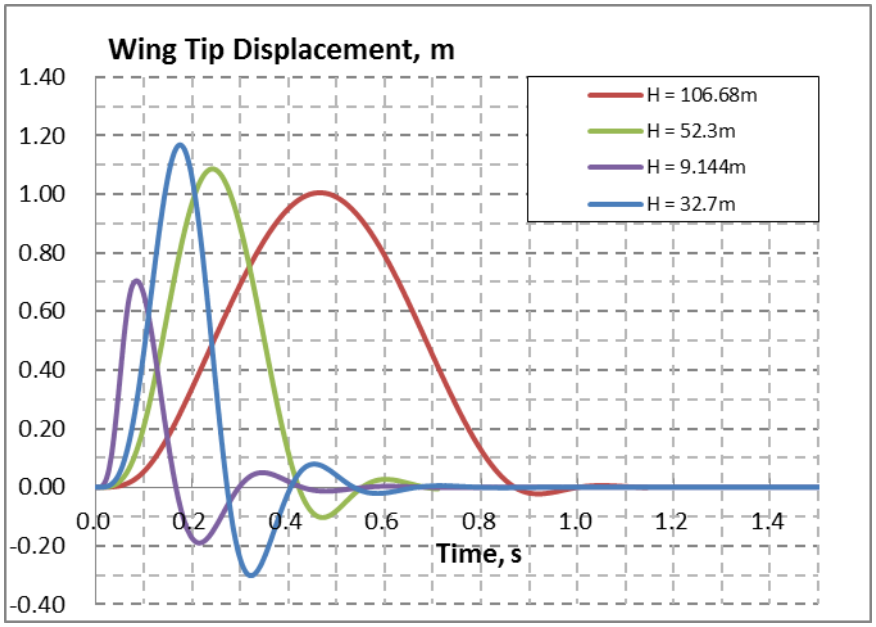

Figure 6.7 Wing tip displacements of structure damping only cases

From these results, it can be concluded that the critical gust load case is at the empty fuel cruise condition with a gust load of a gust gradient length of 106.68m generates a wing tip displacement of 0.9m. The investigation of PGAD is to be carried out based on this gust load condition.

6.3 Practical Optimization of PGAD

6.3.1 Parametric Studies on PGAD Location and Rotational Stiffness

To investigate the effect of the PGAD on gust alleviation based on the baseline wing model, a wing tip segment of 1m of the baseline wing is replaced by PGAD and the rotational degree of freedom of the PGAD about the neutral axis is released. A rotational spring is used to mount PGAD to the main wing body and provides specific rotational stiffness. By varying the spring shaft location, the neutral axis of the PGAD is changing and affecting the gust response of the wing. (See Figure 6.3)

A parametric study was carried out to investigate the effect of stiffness of the rotational spring and neutral axis location (spring location). For the neutral axis location case studies, the efficiency of the device located at four different locations 35%, 25%, 13.7%, and 10% of chord from leading edge are estimated. The corresponding parameter a values are -0.3, -0.5, -0.726, and -0.8. For the location cases $\mathrm{a} = -0.3$ and $\mathrm{a} = -0.5$, the neutral axis are located behind the aerodynamic centre and at the aerodynamic centre. The parameter $\mathrm{a} = -0.726$ is the location of the front spar which is a practical location to hinge the device and $\mathrm{a} = -0.8$ is an ideal neutral axis location with maximum distance ahead of the aerodynamic centre. Recalling the definition of parameter a is given in Figure 2.19. Two different spring stiffness was chosen for parametric studies as 4 kNm^2 and 1 kNm^2. For both parametric studies, PGAD twist angle is limited to ±10˚. The vertical displacements (Z-direction shown in Figure 6.5) of the next to last node are plotted in Figure 6.8 (a) and the twist angle difference between the last two nodes is the PGAD pitching displacement plotted in Figure 6.8 (c). In Figure 6.8 (b), equivalent angles of attack during the gust period are plotted.

a)

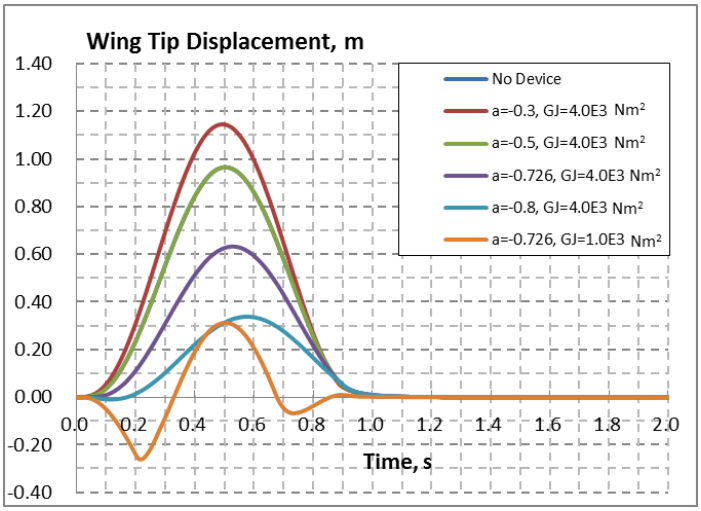

b)

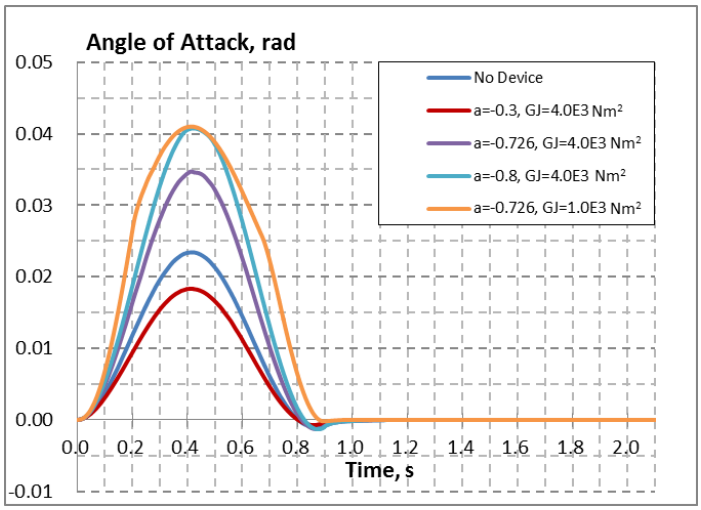

c)

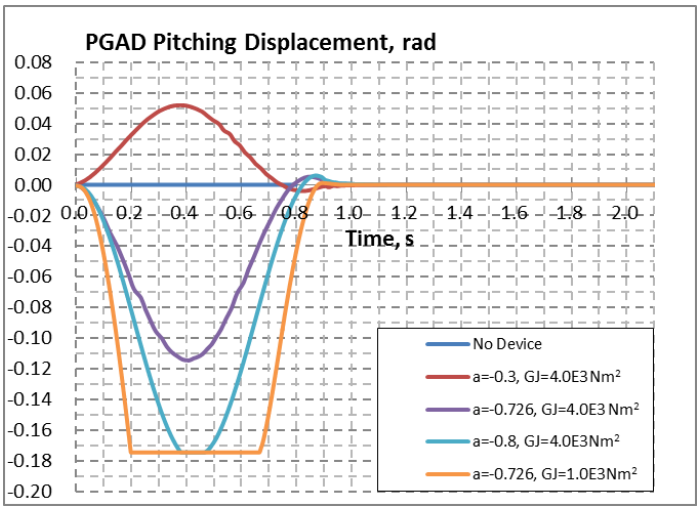

Figure 6.8 Wing tip displacement of varies neutral axis locations and rotational stiffness

In Figure 6.8 a), for the spring shaft location case studies, the $a = -0.5$ is the location of the aerodynamic centre and the tip displacement of the no device case tip displacements result is coincident with the results of the $a = -0.5$ case since no twist was generated by PGAD at the location. When parameter a is greater than -0.5, which indicate neutral axis is behind the aerodynamic centre, for example, at $a = -0.3$, a pitching up moment is generated by PGAD and enhance tip gust response. For those neutral axis ahead of aerodynamic centre cases $(a < -0.5)$, PGAD alleviate gust responses up to 61% at $a = -0.8$ by changing neutral axis locations. For the practical neutral axis location case $(a = -0.726)$, a reduction of 31% is achieved. When neutral axis is greater than -0.5, for example $a = -0.3$, a pitching up moment is generated and tip displacement is 1.18m shown in Figure 6.8 a) and c).

The rotational spring stiffness affects the pithing angle at a specific neutral axis location shown in Figure 6.8 a) and Figure 6.8 c). It can be observed that, for a soften spring (1 kNm^2), PGAD reached its maximum negative twist angle -10˚ and at the early gust period a negative displacement is generated

From these parametric studies, it shows that an optimal design of the PGAD can be obtained by optimize the two design parameters and at a specific neutral axis location and an optimal rotational spring stiffness can be calculated to minimize gust response.

6.3.2 Practical Optimization for Minimum Gust Response

In this optimization process, gradient based determinant method (GBDM) is employed to determine the PGAD design variables. Effort is primarily focused on minimizing the gust response and loading on the wing. The optimization analysis can be expressed as follows:

$$\begin{cases} Minimum\ Gust\ Response\ (x) \\ -0.1 \geq a \geq -0.8 \\ 4\ kNm \geq k \geq 1\ kNm \end{cases} \quad \textbf{(6.11)}$$

The objective of this optimization is to minimize total gust response by taking displacement of the next to last node was taken as wing gust response. Parameters x a vector are the key parameters of the PGAD as design variables. The optimizations were carried at neutral axis locations of $a = -0.1$, $a = -0.5$, $a = -0.726$, and $a = -0.8$. The optimization results are given in Figure 6.9.

a)

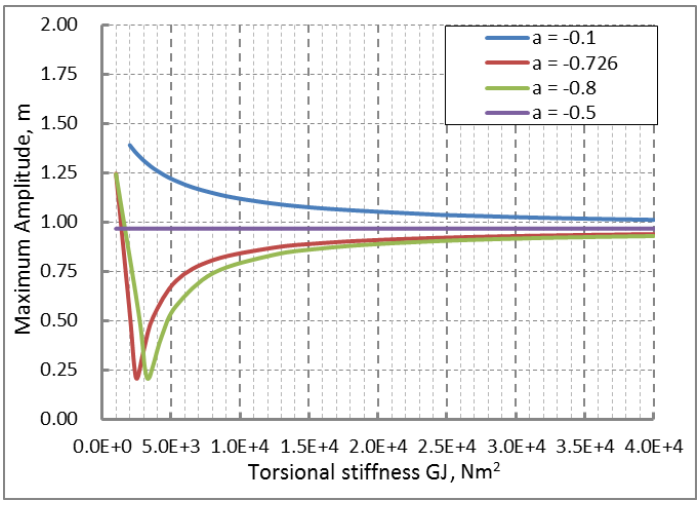

b)

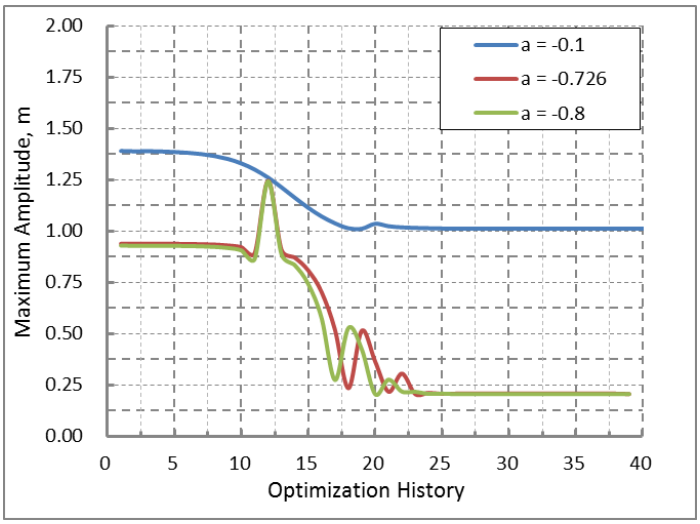

Figure 6.9 Results of PGAD minimum gust response optimization

a) Optimized response varying with the spring stiffness

b) Optimization history for different shaft locations

From Figure 6.9, it shows that after around 25 iterations, a minimum gust response can be achieved by varying spring stiffness. For $a > -0.5$, with the increase of the spring stiffness the tip displacement decreases minimum gust response achieved at the maximum spring stiffness and while $a < -0.5$ a minimum gust can be obtained at specific spring stiffness. For the practical case ($a = -0.726$), the minimum gust response of 0.25m, which reduced gust response by 70%, was obtained at the spring stiffness of 2.5 kNm^2.

PGAD reduces lift during cruise condition if neutral axis is ahead of aerodynamic centre. This effect enhances with a closer location of neutral axis to leading edge and softer spring. By considering this negative effect, a practical limit on the spring stiffness of 3.2 kNm^2 is introduced to limit 10% loss of lift during conventional cruise condition. At this spring stiffness, the tip gust response displacement is 0.5 m which is 15% less efficient than minimum gust response but is a significant benefit.

6.4 Application on a Flying Wing Concept

The investigation of the device efficiency was also carried out on a composite flying wing concept aircraft. The technical data of the concept is given in Table 6.7. The wing layout is given in Figure 6.10 and the spanwise lift and shear force are plotted in Figure 6.11. The composite material IM7/8552 properties are listed in Table 3.4.

Table 6.7 Design technical data of the flying wing concept

Wing span (m)	Fuselage length (m)	MTOM (full fuel, kg)	MTOM (empty fuel, kg)	Sweep angle (deg.)	Cruise altitude (km)
31.6	14.7	27674.2	11729.5	30	18.3

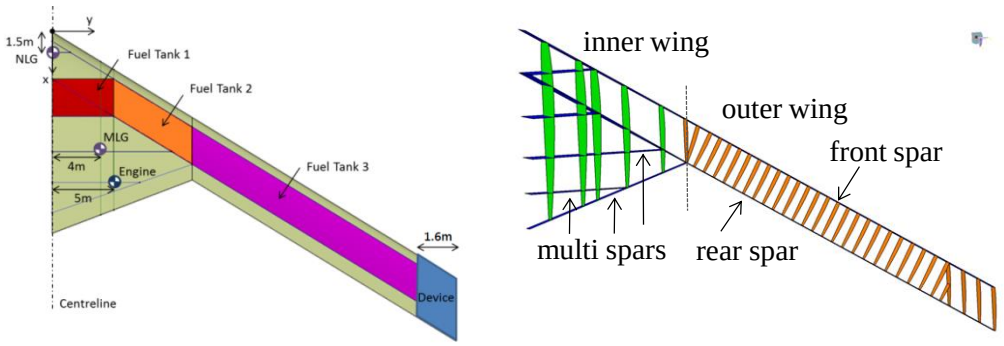

Figure 6.10 Layout of the flying wing concept

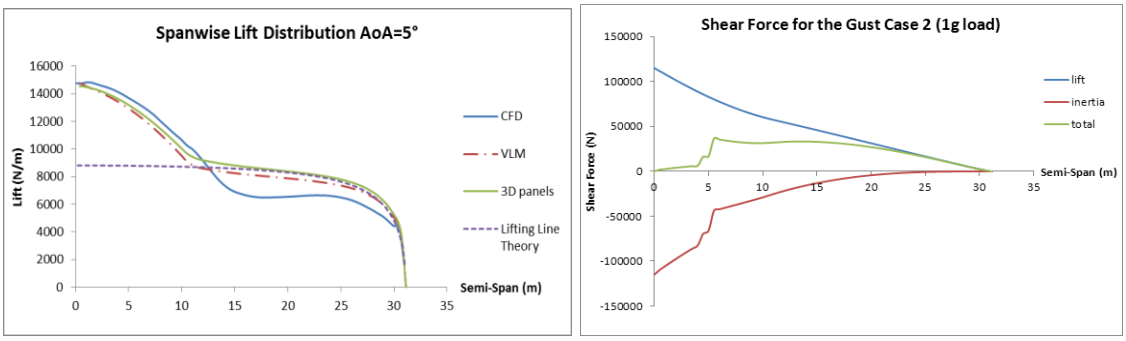

a) Spanwise lifting force b) Spanwise shear force

Figure 6.11 Spanwise lift and shear force distribution by different methods

For initial design, optimal design method developed in Chapter 4 was applied for panel design of the upper surface of the flying wing. The initial design results are listed in Table 6.8.

Table 6.8 Skin panel thickness of the initial design

Section	Upper skin thickness (mm)	Lower skin thickness (mm)	Section	Upper skin thickness (mm)	Lower skin thickness (mm)
1	4.5	3.7	7	5.2	3.4
2	5.3	2.9	8	4.7	3.9
3	6.0	3.1	9	4.2	3.4
4	7.6	5.2	10	3.1	2.6
5	6.3	4.5	11	2.1	2.9
6	5.8	3.9			

FE model was setup and strength check for the initial design was carried out and the maximum strain magnitude reaches 3320 με which is under the limit of 3500 με. The buckling load factors of wing box upper surface panels are checked with ESDU 03001 [163] and the results showed that the initial design satisfies strength and buckling requirements.

The first four mode frequencies of the FE model are listed in Table 6.9. The similar critical gust load case calculation was applied and the critical gust gradient length was 79.1m with a gust frequency of 0.65 Hz. Optimization of the PGAD device was applied with practical design constraints. The results show a practical shaft location at a=-0.7, and a spring stiffness of 28kN, the maximum gust response is 1.79m. Comparing with the 2.25m for the no device case, a gust response reduction of 17% was achieved.

Table 6.9 The modal frequencies of the wing FE and beam models

	FE Model	Beam Model
1st Bending Mode:	0.69 Hz	0.626 Hz
2nd Bending Mode:	3.16 Hz	3.104 Hz
3rd Bending Mode:	6.80 Hz	7.500 Hz
1st Torsion Mode:	12.18 Hz	13.22 Hz

To study the effect of PGAD to the aircraft including rigid body motion was included for the gust response analysis, an FE beam model was created in Patran/Nastran according to the EI, GJ used for in the beam model. The vertical degree of freedom at the wing root is released for including aircraft rigid body motion for gust response analysis. The first five modes (including rigid motion mode) are listed in Table 6 10.

Table 6.10 The modal frequencies of the FE beam model with rigid body motion

Mode No.	1	2	3	4	5
Freq. (Hz)	2.94E-5	0.766	3.657	8.706	15.069

The Nastran gust analysis results are plotted in Figure 6.12. Figure 6.12 a) is the displacement results of no device gust response of the composite wing and Figure 6.12 b) is the gust response of the composite wing equipped with the optimal designed PGAD compared with no device tip relative displacement.

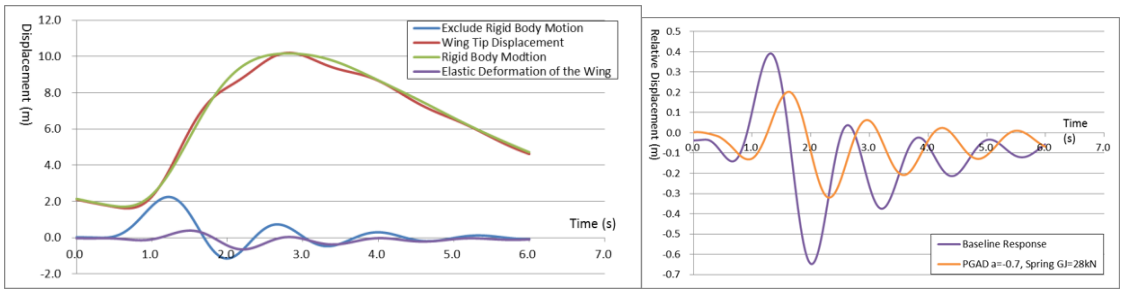

a) b)

Figure 6.12 Gust response of the flying wing concept with rigid body motion

a) Baseline gust response including rigid body motion

b) PGAD gust response with optimal design parameters

In Figure 6.12 a), the rigid body motion displacement was measured as the vertical displacement of the node at wing root. The relative displacement between the wing tip and wing root was taken as the elastic deformation of the wing. Less elastic deformation is observed for the gust response of the aircraft to the gust response of the wing. The difference between exclude rigid body motion displacements and elastic deformation displacements is due to the motion of the aircraft absorbs energy and alleviates gust effect.

In Figure 6.12 b), the elastic deformation displacments in Figure 6.12 a) was taken as the baseline and compared with the displacements of the composite wing equiped with optimal designed passive gust alleviation device. The results showed that the displacments were reduced by around 50%.

The bending moment at the wing root of the baseline response and optimal designed PGAD device equiped composite wing are plotted in Figure 6.13.

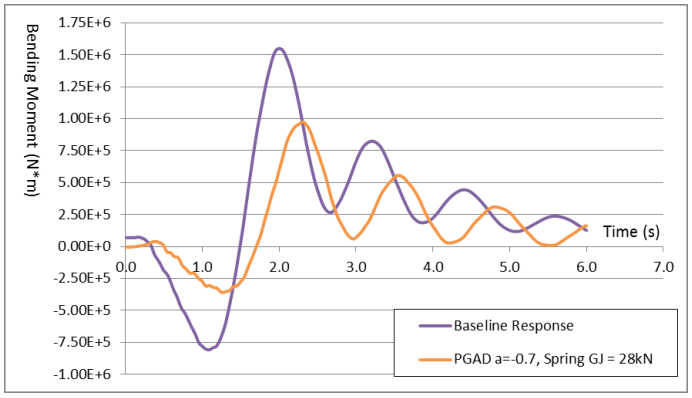

Figure 6.13 Bending moment alleviation at wing root

The bending moment at the wing root was reduced by 37.2% with the PGAD device.

6.5 Conclusion

To investigate the effect of PGAD, this chapter started from modal analysis of the optimized composite wing in Chapter 5 which taken as the baseline wing model and developed a beam wing model for dynamic analysis with similar dynamic behaviour compared with the baseline wing model. The gust load factor at cruise and landing conditions are calculated. Two different mass cases were considered at each flight conditions. Critical gust condition which has the maximum gust load factor was found at cruise condition with empty fuel. The gust response was then estimated at three different gust gradient length to calculate the critical gust gradient length and the maximum tip displacement is 0.9m and happens at the gust gradient length of 106.68m. This gradient length is used for further optimal design and optimization.

PGAD was introduced by replacing a 1m spanwise length segment of the baseline wing mounted with a shaft and a rotational spring. Parametric studies based on two design parameters, neutral axis location and spring stiffness, were carried out. Result shows PGAD can significantly reduce gust displacement at wing tip at an optimal set of neutral axis location and spring stiffness. To achieve a minimum gust response, gradient based optimization technique was introduced and optimization was carried out by changing rotational spring stiffness at several neutral axis locations. Considering practical design constraints, the gust response can be reduced by 44% at front spar location and the rotational spring stiffness is 3.2 kNm^2 for a practical optimal design.

PGAD was also applied to a flying wing concept aircraft. Composite wing design was carried out and similar optimal design of the device was processed. For a practical optimal design 17% less tip deflection can be achieved when the shaft mounted to the front spar and the torsional stiffness of this spring set to 28 kNm^2. Then the aircraft rigid motion response to the gust was considered with response solved in Patran/Nastran and analysis result show for the optimal design it not only reduced wing tip deflection by around 50% but also alleviated bending moment at the wing root by 37.2%.

7 Conclusion and Discussion

7.1 Optimization Process of a Composite Wing

In the research of optimization of a composite wing, attention was firstly focused on optimal structure type determination subject to buckling and took the upper surface panels of a commercial aircraft wing as an example. An optimal design method for composite stringer stiffened panel with practical design constraints was developed and applied in the reference wing initial design stage. A gradient based optimization technique was applied in the optimization stage to obtain a minimum weight composite wing design. Some of key conclusions are drawn here:

1. For optimal structure type determination, under uniaxial compression loads, in the low load range (0 - 800 N/mm) sandwich panels is the most structure type against buckling. In the high load range (> 1000 N/mm) the stringer stiffened panels are more efficient. Under a compressive and shear combined load condition, sandwich panel is the most efficient structure type in the low load range and the affect from the shear load is limited. In the high load range, when the shear ratio is more than a certain amount grid structure is more efficient than stringer stiffened panel starting from the low load range and at around 30% grid structure is the most efficient structure type covers the whole practical design range.

2. With a practical laminate layup and in the spanwise compression load range of the reference wing, an optimal design method of composite stringer stiffened panels was developed and provided optimal design with the global and local buckling took place with a less than 15% deviation of buckling stress.

7.2 Optimal Design of a Passive Gust Alleviation Device

A Passive Gust Alleviation Device was investigated as a wing tip device of a commercial aircraft. Parametric studies were carried out on the tip device of the reference wing. Some of the key conclusions are listed here:

1. The response of the wing is sensitive to the gust frequency and gradient length.
2. The Parametric study has shown that performance of the passive gust alleviation device is sensitive to the shaft location and rotational spring stiffness.
3. With a gradient based optimization technique, a 45% reduction in gust response can be achieved with practical constraints on key design parameters with considering cruise condition lift reduction effect due to the device.
4. PGAD can also be applied to large flying wing concept and it can not only reduce tip deflection but also alleviate wing root bending moment.

7.3 Contribution to Knowledge

In this research work, significant contributions have been made to optimal structure type determination subject to buckling based on loading condition, optimal stringer stiffened panel design, and optimal design of the passive gust alleviation device. The contributions to knowledge are list:

1. Investigation shows that the optimal structure type against buckling varies with the applied load condition, a proper selection in structure type is important.
2. Based on the buckling efficiency comparison among optimal design of sandwich panel, skin-stringer panel, and grid structure, guideline for

structure type determination is provided. In the low load range, sandwich panel is the most efficient structure type and not affected by the shear load. In the high load range, skin-stringer panel is more efficient in the axial compression load domain load cases and with 30% of shear load in a combined load condition, grid structure is more efficient.

3. Emero's optimal design method is validated for multi-stringer stiffened panel optimal design and by comparing with ESDU package and FEA, the results provided by the method is reliable. But this method provides impractical design result such as too small stringer pitch cannot be directly applied for practical design purpose.
4. Emero's optimal design method for stringer stiffened panel has been combined with practical design ratios and constraints for metallic stringer stiffened panel design. By replacing the corresponding stiffness terms, this method was further extended to optimal design of composite stringer stiffened panels. With a practical layup, an optimal design can be achieved.
5. By comparing composite and metallic optimal stringer stiffened panel design, under same distributed load, the buckling stress is close and in the low and high ±45° ply portion range the buckling stress of metallic panels is higher.
6. The deployed and neutral leading edge has almost the same contribution to the entire wing bending and torsional stiffness. The bending stiffness contribution of morphing leading edge to the entire wing is small.
7. Two design parameters, shaft location and torsional spring stiffness, are important to the performance of PGAD.
8. An optimal design of PGAD can not only reduce the wing tip displacement but also release loading on flying wing concept and conventional wing of a commercial aircraft.

7.4 Future Work

1. Further comparison sandwich panel, composite stringer stiffened panel, and composite grid structure for their buckling behaviours. Complete the efficiency chart for composite optimal structure type determination.
2. Compare composite optimal stringer stiffened panel designed through Emero's method with optimization results of a composite stringer stiffened panel with same weight and layup for validation.
3. Carry out full scale FE wing model gust response analysis with PGAD.
4. Carry out PGAD flutter analysis and study the effect of local PGAD natural mode to gust response of the wing.
5. Create an elastic aircraft beam model for further study on the gust response of the aircraft with PGAD.
6. Carry out wind tunnel experiments and study the performance of the wing then compare with analysis results.

REFERENCES

[1] Soutis, C. Carbon fiber reinforced plastics in aircraft construction. *Materials Science and Engineering: A*, 2005, 412 (1-2), pp. 171-176.

[2] Soutis, C. Fibre reinforced composites in aircraft construction. P*rogress in Aerospace Sciences*, 2005, 41 (2), pp. 143-151.

[3] HexPly 8552 epoxy matrix (180°C/356°F curing matrix). Product Data, Hexcel Composites. Publication FTA 072c, October 2008.

[4] SAFRAN Group. Airbus: *All the Models*. [Online] Available from: http://www.safran-group.com/site-safran/aerospatial/applications-aeronautiques/fiche-application/?id_rubrique=675&detail_applications_g09=A320&constructeur=Airbus (Accessed 10th April 2010).

[5] Cantwell, W. J., Morton, J. The impact resistance of composite materials - a review. *Composites*, 1991, 22 (5), pp. 347-362.

[6] Zou, Y., Tong, L., Steven, G. P. Vibration-based model-dependent damage (delamination) identification and health monitoring for composite structures - a review. *Journal of Sound and Vibration*, 2000, 230 (2), pp. 357-378.

[7] Chai, H., Babcock, C. D., Knauss, W. G. One dimensional modelling of failure in laminated plates by delamination buckling. *International Journal of Solids and Structures*, 1981, 17 (11), pp. 1069-1083.

[8] Alfano, G., Crisfield, M. A. Finite element interface models for the delamination analysis of laminated composites: Mechanical and computational issues. *International Journal for Numerical Methods in Engineering*, 2001, 50 (7), pp. 1701-1736.

[9] Vellaichamy, S., Prakash, B. G., Brun, S. Optimum design of cutouts in laminated composite structures. *Computers and Structures*, 1990, 37 (3), pp. 241-246.

[10] Srivatsa, K. S., Murty, A. V. K. Stability of laminated composite plates with cut-outs. *Computers and Structures*, 1992, 43 (2), pp. 273-279.

[11] Guo, S., Morishima, R. Numerical analysis and experiment of composite sandwich T-joints subjected to pulling load. *Composite Structures*, 2011, 94 (1), pp. 229-238.

[12] Qin, T., Zhao, L., Zhang, J. Fastener effects on mechanical behaviors of double-lap composite joints. *Composite Structures*, 2013, Vol. 100, pp. 413-423.

[13] Fari Bouanani, M., Benyahia, F., Albedah, A., Aid, A., Bachir Bouiadjra, B., Belhouari, M., Achour, T. Analysis of the adhesive failure in bonded composite repair of aircraft structures using modified damage zone theory. *Materials and Design*, 2013, Vol. 50, pp. 433-439.

[14] Vanderplaats, G. N., Weisshaar, T. A. Optimum design of composite structures. *International Journal for Numerical Methods in Engineering*, 1989, 27 (2), pp. 437-448.

[15] Wan, Z., Yang, C., Li, Z. Application of hybrid genetic algorithm in aeroelastic multidisciplinary optimization. *Journal of Beijing University of Aeronautics and Astronautics*, 2004, 30 (12), pp. 1142-1146.

[16] Liu, B., Haftka, R. T., Akgün, M. A. Two-level composite wing structural optimization using response surfaces. *Structural and Multidisciplinary Optimization*, 2000, 20 (2), pp. 87-96.

[17] Liu, B., Haftka, R. T., Akgun, M. A., Todoroki, A. Permutation genetic algorithm for stacking sequence design of composite laminates. *Computer Methods in Applied Mechanics and Engineering*, 2000, 186 (2-4), pp. 357-372.

[18] Nettles, A. T. *Basic mechanics of laminated composite plates*. NASA Marshall Space Flight Centre, Report No.N-95-15763, 1994.

[19] MSC Software. *Composite Failure Criteria*. [Online] Available from: http://www.mscsoftware.com/training_videos/patran/Reverb_help/index.html#page/Laminate%20Modeler/lam_theory.6.5.html (Accessed 10th February 2012).

[20] Vlasov, V. Z. *Thin-Walled Elastic Beams*. 2nd ed. Jerusalem, Israel: Israel Program for Scientists Translation, 1961.

[21] Gjelsvik, A. *The Theory of Thin-Walled Bars*. New York: John Wiley and Sons, Inc., 1981.

[22] Guo, S. Aeroelastic optimization of an aerobatic aircraft wing structure. *Aerospace Science and Technology*, 2007, 11 (5), pp. 396-404.

[23] Guo, S., Cheng, W., Cui, D. Aeroelastic tailoring of composite wing structures by laminate layup optimization. *AIAA Journal*, 2006, 44 (12), pp. 3146-3150.

[24] Perera, M., Guo, S. Optimal design of a seamless aeroelastic wing structure. In: *50th AIAA/ASME/ASCE/AHS/ASC Structures, Structural Dynamics and Materials Conference*, Palm Springs, California, 4-7 May, 2009.

[25] Xie, J., Yang, Z., Guo, S. A flexible wing with conformal control surfaces for optimum trim of a tailless air vehicle. In: *51st AIAA/ASME/ASCE/AHS/ASC Structures, Structural Dynamics and Materials Conference*, Orlando, Florida, 12-15 April, 2010.

[26] Xie, J., Yang, Z., Guo, S. Trim optimizations of an adaptive tailless aircraft with composite wing. *Advanced Materials Research*, 2011, Vol. 213, pp. 334-338.

[27] Emero, D. H., Spunt, L. Optimization of Multirib and Multiweb Wing Box Structures Under Shear and Moment Loads. In: *AIAA 6th Structures and Materials Conference*, Palm Springs, California, April, 1965.

[28] Niu, M. C. Y. *Airframe Structural Design: Practical Design Information and Data on Aircraft Structures*. Hong Kong: Conmilit Press Limited, 1999.

[29] Timoshenko, S. P., Gere, J. M. *Theory of Elastic Stability*. 2nd ed. Dover Publications, Inc., 2009.

[30] Galambos, T. V. *Structural Members and Frames*. New Jersey, USA: Prentice-Hall, Inc., 1968.

[31] Salem, A. H. *The sway critical loads of multi-storey frames with varying column sections and loaded at intermediate floor levels*. PhD Thesis, Faculty of Engineering, Ain Shams University, 1968.

[32] Allen, H. G., Bulson, P. S. *Background to Buckling*. New York: McGraw-Hill Book Company Limited,1980.

[33] Megson, T. H. G. *Aircraft Structures for Engineering Students*. 3rd ed. Oxford: Butterworth-Heinemann, 1999.

[34] Chen, J. Q. Mechanics of Composite Materials. 2nd ed. Beijing, China. Science Press, 2008

[35] Airbus S.A.S. *A350 wing Illescas 15-09-2011 – 12*. [Online] Available from: http://www.airbus.com/galleries/photo-gallery/?p=99#open=galleries/photo-gallery/dg/idp/18812-a350-wing-illescas-15-09-2011-12/?backURL=galleries/photo-gallery/?p=99 (Accessed 15th February 2012).

[36] Becker, H. *Handbook of Structural Stability Part II - Buckling of Composite Elements*. No. NACA-TN-3782. NASA, New York University, New York, 1957.

[37] Gerard, G. *Handbook of Structural Stability Part IV - Failure of Plates and Composite Elements*. No. NACA-TN-3784. NASA, New York University, New York. 1957.

[38] Lundquist, E. E., Stowell, E. Z., Schuette, E. H. *Principles of Moment Distribution Applied to Stability of Structures Composed of Bars or Plates*. No. NACA-TR-809. NASA Center, Langley Research Center, 1945.

[39] Baab, G. W. *Charts for Calculation of the Critical Compressive Stress for Local Instability of Idealized Web- and T-stiffened Panels*. No. NACA-ARR-L4H29, NACA-WR-L-204. NASA Center, Langley Research Center, 1944.

[40] Niu, M. C. Y. *Airframe Stress Analysis and Sizing*. 2nd ed. HongKong: Conmilit Press Ltd., 1999.

[41] Qatu, M. S., Leissa, A. W. Buckling or transverse deflections of unsymmetrically laminated plates subjected to in-plane loads. *AIAA Journal*, 1993, 31 (1), pp. 189-214.

[42] Chai, G. B., Hoon, K. H., Chin, S. S., Soh, A. K. Stability and failure of symmetrically laminated plates. *Structural Engineering and Mechanics*, 1996, 4 (5), pp. 485-496.

[43] Vescovini, R., Bisagni, C. Buckling analysis and optimization of stiffened composite flat and curved panels. *AIAA Journal*, 2012, 50 (4), pp. 904-915.

[44] Harrison, P. N., Le Riche, R., Haftka, R. T. Design of stiffened composite panels by genetic algorithm and response surface approximations. In: *Proceedings of the 36th AIAA/ASME/ASCE/AHS/ASC Structures, Structural Dynamics, and Materials Conference*, New Orleans, Los Angeles, 10-13 April, 1995.

[45] Huybrechts, S. M., Hahn, S. E., Meink, T. E. Grid stiffened structures: A survey of fabrication, analysis and design methods. In: *Processings of the 12th International Committee on Composite Materials (ICCM/12)*. Paris, France, 1999.

[46] Forman, S. E., Hutchinson, J. W. Buckling of reticulated shell structures. *International Journal of Solids and Structures*, 1970, 6 (7), pp. 909-932.

[47] Yamashita, T., Kato, S. Elastic buckling characteristics of two-way grid shells of single layer and its application in design to evaluate the non-linear behavior and ultimate strength. *Journal of Constructional Steel Research*, 2001, 57 (12), pp. 1289-1308.

[48] Bert, C. W., Wang, X., Striz, A. G. Differential quadrature for static and free vibration analyses of anisotropic plates. *International Journal of Solids and Structures*, 1993, 30 (13), pp. 1737-1744.

[49] Helms, J. E., Li, G., Smith, B. H. Analysis of grid stiffened cylinders. In: *2001 Engineering Technology Conference on Energy*, Houston, Texas, 2001.

[50] Kidane, S., Li, G., Helms, J., Pang, S. S., Woldesenbet, E. Buckling load analysis of grid stiffened composite cylinders. *Composites Part B: Engineering*, 2003, 34 (1), pp. 1-9.

[51] Bai, R., Wang, M., Chen, H. Buckling behaviour of composite AGS with delamination. *Acta Material Composite Science*, 2005, 22 (4), pp. 136-141.

[52] Chen, H. J., Tsai, S. W. Analysis and optimum design of composite grid structures. *Journal of Composite Materials*, 1996, 30 (4), pp. 503-534.

[53] Jaunky, N., Knight, N. F., Ambur, D. R. Optimal design of grid-stiffened composite panels using global and local buckling analyses. *Journal of Aircraft*, 1998, 35 (3), pp. 478-486.

[54] Ambur, D. R., Jaunky, N. Optimal design of grid-stiffened panels and shells with variable curvature. *Composite Structures*, 2001, 52 (2), pp. 173-180.

[55] Bradshaw, R., Campbell, D., Gargari, M., Mirmiran, A., Tripeny, P. Special structures: past, present, and future. *Journal of Structural Engineering*, 2002, 128 (6), pp. 691-709.

[56] Gatta, G., Romano, F. A design approach of a fuselage barrel in grid structure. In: *ASME International Design Engineering Technical*

Conferences and Computers and Information in Engineering Conference, Long Beach, California, 24-28 September, 2005.

[57] Nautic EXPO. *Sandwich Panels*. [Online] Available from: http://www.nauticexpo.com/prod/cel-components-srl/sandwich-panels-aluminium-honeycomb-34324-244378.html (Accessed 20th October 2012).

[58] Pearce, T. R. A., Webber, J. P. H. Experimental buckling loads of sandwich panels with carbon fibre faceplates. *Aeronautical Quarterly*, 1973, Vol. 24, pp. 295-312.

[59] Noor, A. K., Burton, W. S., Bert, C. W. Computational models for sandwich panels and shells. *Applied Mechanics Reviews*, 1996, 49 (3), pp. 155-199.

[60] Librescu, L., Hause, T. Recent developments in the modelling and behaviour of advanced sandwich constructions: a survey. *Composite Structures*, 2000, 48 (1), pp. 1-17.

[61] Frostig, Y. Buckling of sandwich panels with a flexible core – high-order theory. *International Journal of Solids and Structures*, 1998, 35 (3-4), pp. 183-204.

[62] Hohe, J., Librescu, L. A nonlinear theory for doubly curved anisotropic sandwich shells with transversely compressible core. *International Journal of Solids and Structures*, 2003, 40 (5), pp. 1059-1088.

[63] Hause, T., Librescu, L., Camarda, C. J. Postbuckling of anisotropic flat and doubly-curved sandwich panels under complex loading conditions. *International Journal of Solids and Structures*, 1998, 35 (23), pp. 3007-3027.

[64] Côté, F., Deshpande, V. S., Fleck, N. A., Evans, A. G. The out-of-plane compressive behaviour of metallic honeycombs. *Materials Science and Engineering: A*, 2004, 380 (1), pp. 272-280.

[65] Cartie, D. D., Fleck, N. A. The effect of pin reinforcement upon the through-thickness compressive strength of foam-cored sandwich panels. *Composites Science and Technology*, 2003, 63 (16), pp. 2401-2409.

[66] Schmit, L. A., Mehrinfar, M. Multilevel optimum design of structures with fibre-composite stiffened-panel components. *AIAA Journal*, 1982, 20 (1), pp. 138-147.

[67] Gantovnik, V. B., Gürdal, Z., Watson, L. T. A genetic algorithm with memory for optimal design of laminated sandwich composite panels. *Composite Structures*, 2002, 58 (4), pp. 513-520.

[68] Williams, H. R., Trask, R. S., Bond, I. P. Self-healing composite sandwich structures. *Smart Materials and Structures*, 2007, 16 (4), pp. 1198-1207.

[69] Zhang, J., Ashby, M. F. The out-of-plane properties of honeycombs. *International Journal of Mechanical Sciences*, 1992, 34 (6), pp. 475-489.

[70] Calkins, F. T., Mabe, J. H., Butler, G. W. Boeing's variable geometry chevron: Morphing aerospace structures for jet noise reduction. In: *Proceedings of SPIE, the International Society for Optical Engineering*, San Diego, California, 27-28 February 2006.

[71] Thill, C., Etches, J., Bond, I., Potter, K., Weaver, P. Morphing skins. *Aeronautical Journal*, 2008, 112 (1129), pp. 117-139.

[72] Neal, D. A., Good, M. G., Johnston, C. O., Robertshaw, H. H., Mason, W. H., Inman, D. J. Design and wind-tunnel analysis of a fully adaptive aircraft configuration. In: *45th AIAA/ASME/ASCE/AHS/ASC Structures, Structural Dynamics and Materials Conference*, Palm Springs, California, 19-22 April, 2004.

[73] Kintscher, M., Wiedemann, M., Monner, H. P., Heintze, O., Kühn, T. Design of a smart leading edge device for low speed wind tunnel tests in the European project SADE. *International Journal of Structural Integrity*, 2011, 2 (4), pp. 383-405.

[74] Sofla, A. Y. N., Meguid, S. A., Tan, K. T., Yeo, W. K. Shape morphing of aircraft wing: Status and challenges. *Materials and Design*, 2010, 31 (3), pp. 1284-1292.

[75] Statkus, F. D. *Continous skin, variable camber airfoil edge actuating mechanism*. [Online] Available from: http://www.wikipatents.com/4351502.html, United States Patent, No. 4351502, 1980, (Accessed 25th June 2011).

[76] Choi, S. H., Song, K. D., Golembiewskii, W., Chu, S. H., King, G. C. Microwave power for smart material actuators. *Smart Materials and Structures*, 2004, 13 (1), pp. 38-48.

[77] Dano, M. L., Hyer, M. W. SMA-induced snap-through of unsymmetric fibre-reinforced composite laminates. *International Journal of Solids and Structures*, 2003, 40 (22), pp. 5949-5972.

[78] Torsten Anft. *F-14 Tomcat Dimensions*. [Online] Available from: http://www.anft.net/vf-11/f-14.html (Accessed 23rd March 2010).

[79] Ahaus, L. A., Peters, D. A., Runge, H. P. Stall alleviation with multi-element morphing airfoils. In: *Next Generation Vertical Lift Specialists' Meeting*, Fort Worth, Texas, 23-25 February, 2011.

[80] *SADE-flexible high lift structures requirement*. Unpublished document.

[81] Reckzeh, D. *Aerodynamic design of Airbus high lift wings*. Internet Source. [Online] Available from: www.dlr.de/as/.../5/.../reckzeh_aero-design_of_high-lift-wings.pdf (Accessed 12th October 2011).

[82] Bartley-Cho, J. D., Wang, D. P., Martin, C. A., Kudva, J. N., West, M. N. Development of high-rate, adaptive trailing edge control surface for the smart wing phase 2 wind tunnel model. *Journal of Intelligent Material Systems and Structures*, 2004, 15 (4), pp. 279-291.

[83] Morishima, R., Guo, S., Ahmed, S. A composite wing with a morphing leading edge. In: *51st AIAA/ASME/ASCE/AHS/ASC Structures, Structural Dynamics and Materials Conference*, Orlando, Florida, 12-15 April, 2010.

[84] Yin, W. Stiffness requirement of flexible skin for variable trailing-edge camber wing. *Science China Technological Sciences*, 2010, 53 (4), pp. 1077-1081.

[85] Wildschek, A., Havar, T., Plötner, K. An all-composite, all-electric, morphing trailing edge device for flight control on a blended-wing-body airliner. *Proceedings of the Institution of Mechanical Engineers, Part G: Journal of Aerospace Engineering*, 2010, 224 (1), pp. 1-9.

[86] Pecora, R., Barbarino, S., Concilio, A., Lecce, L., Russo, S. Design and functional test of a morphing high-lift device for a regional aircraft. *Journal of Intelligent Material Systems and Structures*, 2011, 22 (10), pp. 1005-1023.

[87] Chen, X., Ge, W., Zhang, Y., Liu, S. Investigation on synthesis optimization for shape morphing compliant mechanisms using GA. *Acta Aeronautica Et Astronautica Sinica*, 2007, 28 (5), pp. 1230-1235.

[88] Shili, L., Wenjie, G., Shujun, L. Optimal design of compliant trailing edge for shape changing. *Chinese Journal of Aeronautics*, 2008, 21 (2), pp. 187-192.

[89] Secanell, M., Suleman, A., Gamboa, P. Design of a morphing airfoil using aerodynamic shape optimization. *AIAA Journal*, 2006, 44 (7), pp. 1550-1562.

[90] Gern, F. H., Inman, D. J., Kapania, R. K. Computation of actuation power requirements for smart wings with morphing airfoils. *AIAA Journal*, 2005, 43 (12), pp. 2481-2486.

[91] Collar, A. R. The Expanding Domain of Aeroelasticity. *Journal of the Royal Aeronautical Society*, 1946, 50 (428), pp. 613-636.

[92] Bisplinghoff, R. L., Ashley, H., Halfman, R. L. *Aeroelasticity*. New York: Dover Publications, Inc., 1996.

[93] MSC Software. *MSC Nastran version 68, aeroelastic analysis user's guide*.

[94] Theodorsen, T. *General theory of aerodynamic instability and the mechanism of flutter*. NACA Technical Report 496, 1935, pp. 413- 433.

[95] Frazer, R. A., Duncan, W. J. *The Flutter of Aeroplane Wings*. *J. Roy. Aeronaut.* 1929, Soc. 33, pp. 407-454.

[96] Lawrence, A. J., Jackson, P. *Comparison of Different Methods of Assessing the Free Oscillatory Characteristics of Aeroelastic Systems*. London: HMSO, 1970. No. 1084.

[97] Hassig, H. J. An approximate true damping solution of the flutter equation by determinant iteration. *Journal of Aircraft*, 1971, 8 (11), pp. 885-889.

[98] Bierbooms, W. *A dynamic model of a flexible rotor*. Delft University of Technology, Report IW-89034-R, 1990.

[99] Bierbooms, W. *A dynamic model of a flexible rotor including unsteady aerodynamics*. European Wind Energy Conference, Glasgow, 1989.

[100] Petot, D. Progress in the semi-empirical prediction of the aerodynamic forces due to large amplitude oscillations of an airfoil in attached or separated flow. In: *9th European Rotorcraft Forum,* Stresa, Italy, 1983.

[101] Petot, D. Differential equation modeling of dynamic stall. *La Recherche Aerospatiale*, 1989, (5), pp. 59-72.

[102] Peters, D. A. Toward a unified lift model for use in rotor blade stability analyses. *Journal of the American Helicopter Society*, 1985, 30 (3), pp. 32-42.

[103] Bierbooms, W. A. A. M. A comparison between unsteady aerodynamic models. *Journal of Wind Engineering and Industrial Aerodynamics*, 1992, 39 (1-3), pp. 23-33.

[104] Sun, M., Tang, J. Unsteady aerodynamic force generation by a model fruit fly wing in flapping motion. *Journal of Experimental Biology*, 2002, 205 (1), pp. 55-70.

[105] Ho, S., Nassef, H., Pornsinsirirak, N., Tai, Y. C., Ho, C. M. Unsteady aerodynamics and flow control for flapping wing flyers. *Progress in Aerospace Sciences*, 2003, 39 (8), pp. 635-681.

[106] Batina, J. T. Unsteady Euler airfoil solutions using unstructured dynamic meshes. *AIAA Journal*, 1990, 28 (8), pp. 1381-1388.

[107] Kreiselmaier, E., Laschka, B. Small disturbance Euler equations: efficient and accurate tool for unsteady load prediction. *Journal of Aircraft*, 2000, 37 (5), pp. 770-778.

[108] Wright, J. R., Cooper, J. E. *Introduction to Aircraft Aeroelasticity and Loads*. 1st ed. Southern Gate: John Wiley & Sons Ltd., 2007.

[109] Hodges, D. H., Pierce, G. A. *Introduction to Structural Dynamics and Aeroelasticity*. 1st ed. Cambridge: Cambridge University Press, 2002.

[110] Crandall, S. H. The role of damping in vibration theory. *Journal of Sound and Vibration*, 1970, 11 (1), pp. 3-18,IN1.

[111] Kamakoti, R., Shyy, W. Fluid-structure interaction for aeroelastic applications. *Progress in Aerospace Sciences*, 2004, 40 (8), pp. 535-558.

[112] Shubov, M. A. Mathematical modeling and analysis of flutter in bending-torsion coupled beams, rotating blades, and hard disk drives. *Journal of Aerospace Engineering*, 2004, 17 (2), pp. 56-69.

[113] Bendiksen, O. O. Review of unsteady transonic aerodynamics: Theory and applications. *Progress in Aerospace Sciences*, 2011, 47 (2), pp. 135-167.

[114] Scanlan, R. H., Tomko, J. J. Airfoil and bridge deck flutter derivatives. *Journal of the Engineering Mechanics Division*, 1971, 97 (6), pp. 1717-1737.

[115] Geuzaine, P., Brown, G., Harris, C., Farhat, C. Aeroelastic dynamic analysis of a full F-16 configuration for various flight conditions. *AIAA Journal*, 2003, 41 (3), pp. 363-371.

[116] Karpel, M. Design for active flutter suppression and gust alleviation using state-space aeroelastic modeling. *Journal of Aircraft*, 1982, 19 (3), pp. 221-227.

[117] Elhami, M. R., Narab, M. F. Comparison of SDRE and SMC control approaches for flutter suppression in a nonlinear wing section. In: *2012 American Control Conference (ACC)*, Montreal, QC, 27-29 June, 2012, pp. 6148-6153.

[118] Moon, S. H., Kim, S. J. Suppression of nonlinear composite panel flutter with active/passive hybrid piezoelectric networks using finite element method. *Composite Structures*, 2003, 59 (4), pp. 525-533.

[119] Moon, S. H., Kim, S. J. Active and passive suppressions of nonlinear panel flutter using finite element method. *AIAA Journal*, 2001, 39 (11), pp. 2042-2050.

[120] Shirk, M. H., Hertz, T. J., Weisshaar, T. A. Aeroelastic tailoring - theory, practice, and promise. *Journal of Aircraft*, 1986, 23 (1), pp. 6-18.

[121] Guo, S. Aeroelastic optimization of an aerobatic aircraft wing structure. *Aerospace Science and Technology*, 2007, 11 (5), pp. 396-404.

[122] Arizono, H., Isogai, K. Application of genetic algorithm for aeroelastic tailoring of a cranked-arrow wing. *Journal of Aircraft*, 2005, 42 (2), pp. 493-499.

[123] Kameyama, M., Fukunaga, H. Optimum design of composite plate wings for aeroelastic characteristics using lamination parameters. *Computers and Structures*, 2007, 85 (3-4), pp. 213-224.

[124] Floris, C., De Iseppi, L. The peak factor for gust lading: A review and some new proposals. *Meccanica*, 1998, 33 (3), pp. 319-330.

[125] Su, W., Cesnik, C. E. S. Dynamic response of highly flexible flying wings. *AIAA Journal*, 2011, 49 (2), pp. 324-339.

[126] Tang, D., Dowell, E. H. Experimental and theoretical study of gust response for high-aspect-ratio wing. *AIAA Journal*, 2002, 40 (3), pp. 419-429.

[127] Zhang, W., Zhang, W., Quan, J., Ye, Z. Gust alleviation of transonic wing. *Chinese Journal of Theoretical and Applied Mechanics*, 2012, 44 (6), pp. 962-969.

[128] Xu, X., Zhu, X., Zhou, Z., Fan, R. Application of active flow control technique for gust load alleviation. *Chinese Journal of Aeronautics*, 2011, 24 (4), pp. 410-416.

[129] Amitay, M., Washburn, A. E., Anders, S. G., Parekh, D. E. Active flow control on the stingray uninhabited air vehicle: Transient behavior. *AIAA Journal*, 2004, 42 (11), pp. 2205-2215.

[130] Sensburg, O., Becker, J., Lusebrink, H., Weiss, F. Gust load alleviation on Airbus A300. In: *3th Congress of the International Council of the Aeronautical Sciences/AIAA Aircraft Systems and Technology Conference*, Seattle, WA, USA, 1982, p. 44.

[131] Vio, G. A., Cooper, J. E. Optimisation of the composite sensorcraft structure for gust alleviation. In: *12th AIAA/ISSMO Multidisciplinary Analysis and Optimization Conference*, Victoria, British Columbia Canada, 10-12 September, 2008.

[132] Ghiasi, H., Pasini, D., Lessard, L. Optimum stacking sequence design of composite materials Part I: Constant stiffness design. *Composite Structures*, 2009, 90 (1), pp. 1-11.

[133] Sandhu R. S. *Parametric study of optimum fiber orientation for filamentary sheet*. Air Force Flight Dynamics Lab Wright-Patterson Afb Oh, Report No. AFFDL-TM-71-1-FBC, 1971.

[134] Cairo, R. P. *Optimum design of boron epoxy laminates*. Grumman Aircraft Engineering Corporation, Report No. TR AC-SM-8089, 1970.

[135] Lansing, W., Dwyer, W., Emerton, R., Ranalli, E. Application of fully stressed design procedures to wing and empennage structures. *Journal of Aircraft*, 1971, 8 (9), pp. 683-688.

[136] Davidon, W. C. Variable metric method for minimization. *SIAM Journal on Optimization*, 1991, 1 (1), pp. 1-17.

[137] Kyu Ha, S., Kim, D. J., Sung, T. H. Optimum design of multi-ring composite flywheel rotor using a modified generalized plane strain assumption. *International Journal of Mechanical Sciences*, 2001, 43 (4), pp. 993-1007.

[138] Thompson, M. D., Eamon, C. D., Rais-Rohani, M. Reliability-based optimization of fiber-reinforced polymer composite bridge deck panels. J*ournal of Structural Engineering*, 2006, 132 (12), pp. 1898-1906.

[139] Spallino, R., Giambanco, G., Rizzo, S. A design algorithm for the optimization of laminated composite structures. *Engineering Computations*, 1999, 16 (3), pp. 302-315.

[140] Han, L., Neumann, M., Xu, J. On the roots of certain polynomials arising from the analysis of the Nelder-Mead simplex method. *Linear Algebra and its Applications*, 2003, Vol. 363, pp. 109-124.

[141] Le Riche, R., Haftka, R. T. Optimization of laminate stacking sequence for buckling load maximization by generic algorithm. *AIAA Journal*, 1993, 31 (5), pp. 951-956.

[142] Nagendra, S., Jestin, D., Gürdal, Z., Haftka, R. T., Watson, L. T. Improved genetic algorithm for the design of stiffened composite panels. *Computers and Structures*, 1996, 58 (3), pp. 543-555.

[143] Todoroki, A., Haftka, R. T. Stacking sequence optimization by a genetic algorithm with a new recessive gene like repair strategy. *Composites Part B: Engineering*, 1998, 29 (3), pp. 277-285.

[144] Park, J. H., Hwang, J. H., Lee, C. S., Hwang, W. Stacking sequence design of composite laminates for maximum strength using genetic algorithms. *Composite Structures*, 2001, 52 (2), pp. 217-231.

[145] Kogiso, N., Watson, L. T., Gürdal, Z., Haftka, R. T. Genetic algorithms with local improvement for composite laminate design. *Structural Optimization*, 1994, 7 (4), pp. 207-218.

[146] Lin, C. C., Lee, Y. J. Stacking sequence optimization of laminated composite structures using genetic algorithm with local improvement. *Composite Structures*, 2004, 63 (3-4), pp. 339-345.

[147] Maksimenko, V. N., Butyrin, V. I., Pavshok, L. V. Optimization of the flat stiffened panels. In: *8th Korea-Russia International Symposium on Science and Technology (Vol. 3)*, Tomsk, 26 June - 3 July, 2004, pp. 38-39.

[148] Ermolaev, N. V., Malkov, V. P., Tarasov, V. L. Composite shells of revolution of minimum mass with constraints on the natural frequencies. *Mechanics of solids*, 1985, 20 (4), pp. 157-161.

[149] Mathias, D. W., Hornung, G., Roehrle, H. Composite elements in structural optimization-investigations on optimality criteria and mathematical methods. In: *ICAS Proceedings, 14th Congress of the International Council of the Aeronautical Sciences (Vol. 2)*, Toulouse, France, 1984, pp. 1179-1187.

[150] Guo, S., Li, D., Liu, Y. Multi-objective optimization of a composite wing subject to strength and aeroelastic constraints. *Proceedings of the Institution of Mechanical Engineers, Part G: Journal of Aerospace Engineering*, 2012, 226 (9), pp. 1095-1106.

[151] Nagendra, S., Haftka, R. T., Gurdal, Z. Design of a blade stiffened composite panel by a genetic algorithm. In: *34th*

AIAA/ASME/ASCE/AHS/ASC Structures, Structural Dynamics, and Materials Conference, La Jolla, California, 19-22 April, 1993, pp. 2418-2436.

[152] Kang, J. H., Kim, C. G. Minimum-weight design of compressively loaded composite plates and stiffened panels for postbuckling strength by Genetic Algorithm. *Composite Structures*, 2005, 69 (2), pp. 239-246.

[153] Isogai, K. Direct search method to aeroelastic tailoring of a composite wing under multiple constraints. *Journal of Aircraft*, 1989, 26 (12), pp. 1076-1080.

[154] Hu, N. Tabu search method with random moves for globally optimal design. *International Journal for Numerical Methods in Engineering*, 1992, 35 (5), pp. 1055-1070.

[155] Morishima, R., Guo, S., Ahmed, S. A composite wing with a morphing leading edge. In: 5*1st AIAA/ASME/ASCE/AHS/ASC Structures, Structural Dynamics and Materials Conference*, Orlando, Florida, 12-15 April, 2010.

[156] Morishima, R., Guo, S. Optimum design of a composite morphing leading edge for high lift wing. In: *4th SEMC Conference*, Cape Town, South Africa, 6-8 September, 2010.

[157] ESDU 98016. Elastic bucking of flat isotropic stiffened panels and struts in compression. ESDU International, February, 2008.

[158] ESDU 88015. Elastic wrinkling of sandwich panels with laminated fibre reinforced face plates. ESDU International, December, 1988.

[159] ESDU 81047. Buckling of flat rectangular plates. ESDU International, December 1981.

[160] Wang, W., Guo, S., Chang, N., Yang, W. Optimum buckling design of composite stiffened panels using ant colony algorithm. *Composite Structures*, 2010, 92 (3), pp. 712-719.

[161] Guo, S., Fu, Q. *Preliminary sizing of skin-stringer panels*. Unpublished document.

[162] Guo, S., Fu, Q. *Preliminary sizing for composite skin-stringer panels*. Unpublished document.

[163] ESDU 03001. Elastic buckling of long, flat, symmetrically-laminated (AsBoDf), composite stiffened panels and struts in compression. ESDU International, 2003.

[164] Liu, I. W., Lin, C. C. Optimum design of composite wing structures by a refined optimality criterion. *Composite Structures*, 1991, 17 (1), pp. 51-65.

[165] Naik, G. N., Gopalakrishnan, S., Ganguli, R. Design optimization of composites using genetic algorithms and failure mechanism based failure criterion. *Composite Structures*, 2008, 83 (4), pp. 354-367.

[166] Ghiasi, H., Pasini, D., Lessard, L. Optimum stacking sequence design of composite materials Part I: Constant stiffness design. *Composite Structures*, 2009, 90 (1), pp. 1-11.

[167] Ghiasi, H., Fayazbakhsh, K., Pasini, D., Lessard, L. Optimum stacking sequence design of composite materials Part II: Variable stiffness design. *Composite Structures*, 93 (1), pp. 1-13.

[168] Librescu, L., Thangjitham, S. Analytical study on static aeroelastic behavior of swept-forward composite wing structures. *Journal of Aircraft*, 1991, 28 (2), pp. 151-157.

[169] Librescu, L., Song, O. On the static aeroelastic tailoring of composite aircraft swept wings modelled as thin-walled beam structures. *Composites Engineering*, 1992, 2 (5-7), pp. 497-512.

[170] Lottati, I. Flutter and divergence aeroelastic characteristics for composite forward swept cantilevered wing. *Journal of Aircraft*, 1985, 22 (11), pp. 1001-1007.

[171] Qin, Z., Marzocca, P., Librescu, L. Aeroelastic instability and response of advanced aircraft wings at subsonic flight speeds. *Aerospace Science and Technology*, 2002, 6 (3), pp. 195-208.

[172] Guo, S., Cheng, W., Cui, D. Aeroelastic tailoring of composite wing structures by laminate layup optimization. *AIAA Journal*, 2006,44 (12), pp. 3146-3150.

[173] Guo, S. Aeroelastic optimization of an aerobatic aircraft wing structure. *Aerospace Science and Technology*, 2007, 11 (5), pp. 396-404.

[174] Perera, M., Guo, S. Optimal design of a seamless aeroelastic wing structure. In: *50th AIAA/ASME/ASCE/AHS/ASC Structures, Structural Dynamics and Materials Conference*, Palm Springs, California, 4-7 May 2009.

[175] Guo, S., Li, D., Liu, Y. Multi-objective optimization of a composite wing subject to strength and aeroelastic constraints. *Proceedings of the Institution of Mechanical Engineers, Part G: Journal of Aerospace Engineering*, 2012, 226 (9), pp. 1095-1106.

[176] Vanderplaats, G. N. *ADS-A Fortran program for automated design synthesis, version 1.10*. NASA Contractor Report 177985, 1985.

[177] MSC software. *MSC Nastran 2010, implicit nonlinear user's guide.*

[178] Morishima, R., Guo, S. Optimal design of a composite wing with a morphing leading edge. In: *17th ICCE Conference*, Honolulu, Hawaii, 26-31 July, 2009.

[179] Ahmed, S. *Aerodynamic and structural analysis of morphing high lift devices*. PhD Thesis of Engineering, Cranfield University, 2012.

[180] Tsai, S. W., Wu, E. M. A general theory of strength for anisotropic materials. *Journal of Composite Materials*, 1971, 5 (1), pp. 58-80.

[181] *Certification Specifications for Large Aeroplanes CS-25*. European Aviation Safety Agency, Amendment3, September 2007.

[182] Guo, S., Cheung, C.W., Banerjee, J. R., Butlar, R. Gust alleviation and flutter suppression of an optimised composite wing. In: *Proceedings of the*

International Forum on Aeroelasticity and Structural Dynamics, Manchester, 1995, pp. 44.1-41.9.

[183] Britt, R. T., Jacobson, S. B., Arthurs, T. D. Aeroservoelastic analysis of the B-2 bomber. *Journal of Aircraft*, 2000, 37 (5), pp. 745-752.

[184] Reich, G. W., Raveh, D. E., Zink, P. S. Application of active-aeroelastic-wing technology to a joined-wing sensorcraft. *Journal of Aircraft*, 2004, 41 (3), pp. 594-602.

[185] Vartio, E., Shimko, A., Tilmann, C. P., Flick, P. M. Structural modal control and gust load alleviation for a sensorcraft concept. In: *46th AIAA/ASME/ASCE/AHS/ASC Structures, Structural Dynamics and Materials Conference*, Austin, Texas, 18-21 April, 2005.

[186] Roberts, R. W., Canfield, R. A., Blair, M. Sensor-craft structural optimization and analytical certification. In: *46th AIAA/ASME/ASCE/AHS/ASC Structures, Structural Dynamics and Materials Conference*, Austin, Texas, 18-21 April, 2005.

[187] Tilmann, C. P., Flick, P. M., Martin, C. A., Love, M. H. High-altitude long endurance technologies for sensorcraft. In: *RTO AVT Symposium on Novel and Emerging Vehicle and Vehicle Technology Concepts (AVT-099)*, Brussels, Belgium, RTO Paper MP-104-P-26, 7-11 April, 2003.

[188] Reich, G. W., Bowman, J. C., Sanders, B. Application of adaptive structures technology to high altitude long endurance sensor platforms. In: *13th International Conference on Adaptive Structures and Technologies*, Potsdam, Germany, 7-9 October, 2002, pp. 423-434.

[189] Nangia, R. K., Palmer, M. E., Tilmann, C. P. Planform variation effects in unconventional high aspect ratio joined-wing aircraft incorporating laminar flow. In: *43rd AIAA Aerospace Sciences Meeting and Exhibit*, Reno, Nevada, 10-13 January, 2005.

[190] Henderson, J. A., Martin, C. A., Kudva, J. N. Sensitivity of optimized structures to constraints and performance requirements for the SensorCraft

ISR platform. In: *44th AIAA/ASME/ASCE/AHS/ASC Structures, Structural Dynamics and Materials Conference*, Norfolk, Virginia, 7-10 April, 2003.

[191] Armanios, E. A., Badir, A. M. Free vibration analysis of anisotropic thin walled closed cross section beams. *AIAA Journal*, 1995, 33 (10), pp. 1905–1910.

[192] Banerjee, J. R., Williams, F. W. Free vibration of composite beams - An exact method using symbolic computation. *Journal of Aircraft*, 1995, 32 (3), pp. 636-642.

[193] Guo, S. *BOXMXESDC*. Unpublished document.

[194] Wittrick, W. H., Williams, F. W. A general algorithm for computing natural frequencies of elastic structures. *Quarterly Journal of Mechanics and Applied Mathematics*, 1971, 24 (3), pp. 263-284.

[195] Liani, E., Guo, S. Potential-flow-based aerodynamic analysis and test of a flapping wing. In: *37th AIAA Fluid dynamics Conference*, Miami, Florida, AIAA-2007-4068, 2007.

[196] Guo, S. *AIRFRAME3D-EBFD*. Unpublished document.

[197] Adams, V., Askenazi, A. *Building Better Products with Finite Element Analysis.* Santa Fe, NM: OnWord Press, 1999.